THEORETICAL INVESTIGATION AND DESIGN OF WIDEBAND DIELECTRIC RESONATOR ANTENNAS

A THESIS SUBMITTED TO
THE GRADUATE SCHOOL OF NATURAL AND APPLIED SCIENCES
OF
MIDDLE EAST TECHNICAL UNIVERSITY

BY

YILMAZ ÇAĞRI YÜKSEL

IN PARTIAL FULFILLMENT OF THE REQUIREMENTS
FOR
THE DEGREE OF MASTER OF SCIENCE
IN
ELECTRICAL AND ELECTRONICS ENGINEERING

MAY 2015

Approval of the thesis:

THEORETICAL INVESTIGATION AND DESIGN OF WIDEBAND DIELECTRIC RESONATOR ANTENNAS

submitted by **YILMAZ ÇAĞRI YÜKSEL** in partial fulfillment of the requirements for the degree of **Master of Science in Electrical and Electronics Engineering Department, Middle East Technical University** by,

Prof. Dr. Gülbin Dural Ünver
Dean, Graduate School of **Natural and Applied Sciences** _____

Prof. Dr. Gönül Turhan Sayan
Head of Department, **Electrical and Electronics Engineering** _____

Assoc. Prof. Dr. Lale Alatan
Supervisor, **Electrical and Electronics Engineering Dept., METU** _____

Examining Committee Members:

Prof. Dr. Mehmet Tuncay Birand
Electrical and Electronics Engineering Dept., METU _____

Assoc. Prof. Dr. Lale Alatan
Electrical and Electronics Engineering Dept., METU _____

Prof. Dr. Özlem Aydın Çivi
Electrical and Electronics Engineering Dept., METU _____

Prof. Dr. Şimşek Demir
Electrical and Electronics Engineering Dept., METU _____

M.Sc. Doğanay Doğan
Aselsan, REHS Division _____

Date: **05/05/2015**

I hereby declare that all information in this document has been obtained and presented in accordance with academic rules and ethical conduct. I also declare that, as required by these rules and conduct, I have fully cited and referenced all material and results that are not original to this work.

Name, Last name : Yılmaz Çağrı Yüksel

Signature :

ABSTRACT

THEORETICAL INVESTIGATION AND DESIGN OF WIDEBAND DIELECTRIC RESONATOR ANTENNAS

Yüksel, Yılmaz Çağrı

M.S., Department of Electrical and Electronics Engineering

Supervisor: Assoc. Prof. Dr. Lale Alatan

May 2015, 111 page

The aim of this thesis is to utilize Dielectric Resonator Antennas (DRA) as array elements due to their advantages over other conventional antenna elements such as dipoles and microstrip patches. Depending on both the excitation mechanisms and the antenna shape, a Dielectric Resonator Antenna (DRA) provides its designer multiple independent degrees of freedom. In this thesis three antenna shapes, namely hemispherical, cylindrical and rectangular DRAs, are investigated. The cylindrical and the rectangular shaped DRAs are used in designs. A design software that calculates the initial dimensions of the DRAs is developed and these dimensions are optimized through the full-wave analysis performed by using a Finite Element Method (FEM) based electromagnetic field solver.

The concept of a compact DRA with wideband operation in 2.9-3.3 GHz frequency band is presented. The return losses, impedance characteristics, internal field distributions and radiation patterns of DRA elements are discussed. The effect of dimensional parameters of both antenna element and feed network are investigated. The rectangular and stack-cylindrical shaped DRAs are manufactured and excited via microstrip slots. For rectangular DRA a -10dB impedance bandwidth of 20.3% and a gain of 5.28dB are obtained. An enhancement is achieved both in the -10dB

impedance bandwidth (44.7%) and the gain of the antenna (9.35dB) with stacked-cylindrical DRA configuration.

A Taylor amplitude tapered linear array is designed to achieve 10 degree half power beam width (HPBW) with 30dB side lobe level (SLL). An 8-arm modified Wilkinson unequal power divider is designed to implement a linear array with high ratios between excitation amplitudes. Array characteristics are measured in the near field antenna measurement chamber. The prototype and the test results for the antenna element and the array structure are discussed. For rectangular DRA array, 10.1dB gain, -26dB SLL and 9.6^0 HPBW are obtained. For stacked-cylindrical DRA configuration, 14.3dB gain, -26.9dB SLL and 9.5^0 HPBW are achieved.

Keywords: dielectric resonator antenna, stacked cylindrical, slot coupled feed.

ÖZ

GENİŞ BANTLI DİELEKTRİK REZONATÖR ANTENLERİN ANALİZ VE TASARIMI

Yüksel, Yılmaz Çağrı
Yüksek Lisans, Elektrik ve Elektronik Mühendisliği Bölümü
Tez Yöneticisi: Doç. Dr. Lale Alatan

Mayıs 2015, 111 sayfa

Bu tezde dielektrik rezonatör antenlerinin dizi yapısı içerisinde kullanımı amaçlanmıştır. Anten şekli ve besleme mekanizmalarına göre Dielektrik Rezonatör Antenler (DRA) tasarımcısına çeşitli seçim serbestliği sağlamaktadırlar. Bu tezde üç temel anten şekli; yarı küresel, silindirik ve dikdörtgen biçimli DRA'lar incelenmiş olup silindirik ve dikdörtgen biçimli DRA tasarımları yapılmıştır. Bununla birlikte tasarım başlangıcında anten boyutlarını hesaplamak için kullanılmak üzere bir yazılım geliştirilmiş, geliştirilen yazılımla tasarlanan antenlerin Sonlu Elemanlar Metodu (FEM) tabanlı elektromanyetik yapı çözücüsü kullanılarak tam dalga analizleri yapılmış ve boyutları optimize edilmiştir.

2.9-3.3GHz frekans bandında çalışan kompakt bir DRA konsepti gösterilmiştir. Tasarlanan antenlerin geriş dönüş kaybı, empedans karakteristikleri, dahili alan dağılımları ve ışıma örüntüleri incelenmiştir. Anten ve besleme mekanizmasının boyutlarının yapı üzerindeki etkileri parametrik olarak araştırılmıştır. Dikdörtgensel ve katmanlı-silindirik DRA üretilmiş ve mikroşerit yarıklar ile beslenmiştir.

Dikdörtgensel DRA yapısında %20.3 -10dB geri dönüş kaybı bant genişliği ve 5.28dB kazanç gözlenmiştir. Katmanlı-silindirik DRA yapısı ile %44.7'lik -10dB geri dönüş kaybı bant genişliği ve 9.35dB kazanç elde edilmiştir.

10 derece ana hüzme genişliği ve 30dB yan hüzme seviyesi elde etmek üzere Taylor genlik dağılımlı doğrusal anten dizisi tasarımı yapılmıştır. Sekiz dikdörtgensel (ve katmanlı-silindirik) elemandan oluşan doğrusal dizide kullanılmak üzere sekiz kollu güç bölücü tasarlanmıştır. Doğrusal dizide elemanlar arası genlik dağılımını sağlayabilmek amacıyla çeşitli güç bölüm topolojileri incelenmiş, değiştirilmiş eşitsiz Wilkinson bölücü yapısı kullanılmıştır.

Dizi antenler yakın alan test odasında ölçülmüştür. Anten elemanları ve dizi yapılarının ışıma ölçümleri, HFSS simülasyonları ile karşılaştırmalı olarak incelenmiştir. Dikdörtgensel DRA ile oluşturulan dizi yapısında 10.1 dB kazanç, -26dB yan hüzme seviyesi and 9.6 derece yarım güç hüzme genişliği, Katmanlı-silindirik DRA ile oluşturulan dizi yapısında 14.3dB kazanç, -26.9dB yan hüzme seviyesi ve 9.5 derece yarım güç hüzme genişliği elde edilmiştir.

Anahtar Kelimeler: dielektrik rezonatör anten, katmanlı silindirik, mikroşerit yarık besleme.

Dedicated to my family and Elif,

You most of all, made this possible.

ACKNOWLEDGEMENTS

I sincerely thank my supervisor Assoc. Prof. Dr. Lale Alatan for all her guidance and support throughout my study. I would like to thank to Dr. Can Barış Top for his expert opinions related to antenna design and Prof. Dr. Sencer Koç for his guidance in material selection. I also would like to thank Erdinc Yurdakul for his help in production of antenna prototypes.

I also thank to Melih Gönül and Damla Ülker for their assistance in measurement of array patterns in near field antenna measurement station, Ömer Öçal for his help in production of beam former network and İsmail Kökbıyık for the design of array antenna support block.

More personally, I would also like to extend special thanks to my friend Damla Alptekin for her encouragement at the times when I needed a gentle push to keep me going during my study.

Last, I would like to thank ASELSAN Inc. for financing and providing resources during my study.

TABLE OF CONTENTS

LIST OF FIGURES

FIGURES

CHAPTER 1

INTRODUCTION

The aim of this thesis is to design a linear antenna array that will operate within 2.9-3.3GHz frequency band with a 3dB half power beamwidth of 10° and sidelobe levels below -30dB. These highly suppressed sidelobe levels require amplitude tapering for the excitation of array elements. Therefore a feeding network based on microstrip technology is preferred due to the ease in design and manufacturing. In microstrip technology printed dipole or microstrip antennas are widely used as antenna elements. However, in recent years dielectric resonator antennas (DRAs) became an attractive alternative due to the techniques proposed to broaden the operational bandwidth of these relatively narrow band structures. Hence, DRAs are chosen to be the array elements in this thesis.

In this chapter a brief history of dielectric resonator antennas (DRAs) is mentioned highlighting the main developments in this evolving technology. A list of general characteristics of DRAs is put together to point out where they stand when compared to traditional antenna elements, such as dipoles and microstrip patches. Their strengths and weaknesses are also discussed concisely.

1.1 Brief History of Dielectric Resonator Antennas

In 1939, R.D Richtinger showed that nonmetallic dielectric objects which he called dielectric resonators [1] could function similar to metallic cavities, and the modal analysis of them were first presented in the early 1960s by Okaya and Barash [2]. The analysis opened the way for the use of these low-loss dielectric materials as dielectric resonators in filters and oscillators instead of or alternative to the waveguide cavity resonators and as a more conformable topology for printed circuit integration.

If the shielding is removed the dielectric resonators can be made to radiate very efficiently when excited at certain frequencies [3]. Furthermore, broadband responses can be obtained by lowering their dielectric constants. In 1980s began the first studies of dielectric resonator antennas started with the examination of the characteristics of typical shapes such as hemispherical, cylindrical and rectangular. After several studies had been carried out on their excitations and radiation patterns, DRAs became more intriguing alternative to traditional low-gain radiators. Also the first planar array of DRAs are demonstrated by Birand and Gelpsthorpe [4] in the same decade (Fig. 1). The array was designed to operate between 32 and 35GHz. The measured data had a good agreement with the theoretical data although the design was made using simple array theory. The design consisted of 12 DRAs and was operated in leaky-wave configuration, producing a beam whose peak scanned with frequency from 6° to 20° -off broadside.

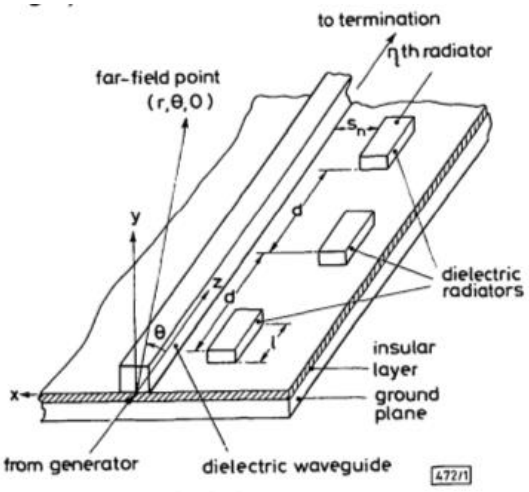

Fig. 1 Dielectric waveguide fed linear DRA array

In 1990s more attention was placed both on the feeding mechanisms to excite the DRAs and on establishing the relation between the input impedance, bandwidth, dielectric constant, shape and Q-factor. In 1994 Mongia and Bhartia published their work to characterize the performance of basic DRA elements [5] in which they proposed the mode nomenclature and provided a set of equations for predicting the resonant frequency and quality factor (Q-factor) for DRAs with basic shapes.

Since mid-1990s as more researchers studied in this field and more mobile devices have become widespread; more emphasis have been put on compact, portable, hybrid DRA solutions to meet the requirements for emerging broadband or ultra wideband systems.

1.2 Major Characteristics

The main characteristics of simple-shaped DRAs are listed below. These findings are also applicable for most DRAs that are more complicated in shape.

- The size of the DRA is proportional to $\lambda_0/\sqrt{\epsilon_r}$,with λ_0 and ϵ_r being the free-space wavelength and relative dielectric constant, respectively. Therefore a reduction in size can be easily achieved by choosing a material with high dielectric constant.

- A wide range of dielectric constants can be selected from 4 to 100, allowing the designer to have control over the physical size of the DRA and its bandwidth. As both microstrip patch antenna and DRA behave like resonant cavities, both antenna types therefore can be made small by increasing the permittivity.

- Radiation Q-factor and the resonant frequency is a function of the aspect ratio (ratio of two dimensions of the dielectric shape) of the DRA for a fixed dielectric constant. Since the same aspect ratio can be achieved for infinite number of size combinations, this property allows a flexibility in controlling the input impedance and bandwidth of the antenna. The losses for a DRA are the dielectric losses due to conductivity of the dielectric material which is usually negligible and conductor loss in the feeding structure and the ground plane.

- When a dielectric material is selected with low loss characteristics, a DRA would have the capacity of providing efficient radiation in the millimeter wave (MMW) frequency region due to the absence of surface waves and the inherent conductor losses. This has been proved experimentally through comparison of a DRA with a conventional microstrip antenna at 35GHz [6]. The DRA exhibits a high radiation efficiency (>90%) with negligible dissipation loss, whilst the performance of conventional metallic antennas

rapidly degrades with a radiation efficiency of around 80%.

- DRAs can be designed to operate over a wide frequency band from as low as 1GHz to as high as 40GHz. Also DRAs can be excited by many feeding schemes including probes, slot coupled microstrip lines, dielectric image guides, and substrate integrated waveguides (SIW). Depending on the DRA shape and feeding scheme several modes can be excited within the DRA - some of which are similar to short electric and magnetic dipoles- for different coverage requirements.

Costwise, in some designs, materials must be machined precisely from large blocks. Moreover drilling may be necessary for several excitations as probes, or the DRAs have to be bonded to ground plane. These requirements make the manufacturing process generally more complex and more costly. However for mass production, the cost differences associated with these processes may not be significant. There are also some application areas such as military communications or intelligence systems where performance is more important than cost and DRAs may provide solutions that cannot be offered by any other radiating elements.

1.3 Organization of the Thesis

After the introduction, the dielectric antenna and several feed configurations will be discussed in next chapter in order to give an insight on the terms used in subsequent sections. The basic shaped antennas are illustrated with theoretical analysis. The design procedures are described in details for fundamental shapes. In Chapter 3, the basic properties of several feed configurations such as coaxial probe, direct microstrip feed and the aperture slot are characterized with simulations. In Chapter 4, a design tool for rectangular and cylindrical DRAs is introduced. Chapter 4 also focuses on the design of the thesis work. Rectangular, cylindrical and stacked-cylindrical DRA elements are designed and investigated using simulations. In Chapter 5, a beam former network for the array application is discussed. The array tapering method is explained. The divider topologies are also discussed. In Chapter 6, the fabrication of the array elements and the beam former network are mentioned. The experimental results are compared with the simulations. Chapter 7 presents some conclusions and recommendations for the future work.

CHAPTER 2

DIELECTRIC RESONATOR ANTENNA CONFIGURATIONS

This chapter mainly focuses on exemplifying various DRA configurations in terms of both shape and feeding structures. Before investigating complicated DRA shapes, most commonly used three basic DRA shapes, namely, hemispherical, cylindrical and rectangular will be introduced.

2.1 The Hemispherical DRA

The most basic geometry of a hemispherical DRA is shown in Fig. 2. ϵ_r and radius α are the only design parameters of the antenna. The antennas discussed and designed in this thesis are considered to be mounted on an infinite ground plane which is assumed to be perfect conductor.

According to image theory a dielectric hemisphere mounted on a ground plane can be considered as a dielectric sphere in free space.

The resonant modes of dielectric spheres in free space were investigated in details by Gastine, Courtois and Dormann in 1967 [7]. Authors proposes two mode configurations, transverse electric (TE_{mn}) to R and transverse magnetic (TM_{mn}) to R for spherical DRA. The two subscripts describes the mode for the field variation in azimuth *(Ø)* and elevation *(*θ*)* directions. TE_{mn} modes have zero value for radial component of the electric field and other components of electric and magnetic field are given as:

$$E_r = 0$$

$$E_\theta = -\frac{jkm}{rsin\theta}\sqrt{\frac{\mu}{\epsilon}}\sqrt{kr}j_{n+1/2}\,(kr)P_n^m(cos\theta)\begin{matrix}cos\\-sin\end{matrix}m\emptyset$$

$$E_\emptyset = -\frac{jk}{r}\sqrt{\frac{\mu}{\epsilon}}\sqrt{kr}\,j_{n+1/2}\,(kr)\frac{dP_n^m(cos\theta)}{d\theta}\begin{matrix}sin\\cos\end{matrix}m\emptyset$$

$$H_r = -\frac{n(n+1)}{r^2}\sqrt{kr}\,j_{n+1/2}\,(kr)P_n^m(cos\theta)\begin{matrix}sin\\cos\end{matrix}m\emptyset$$

$$H_\theta = \frac{1}{r}\frac{d[\sqrt{kr}\,j_{n+1/2}\,(kr)]}{dr}\frac{dP_n^m(cos\theta)}{d\theta}\begin{matrix}sin\\cos\end{matrix}m\emptyset$$

$$H_\theta = \frac{m}{rsin\theta}\frac{d[\sqrt{kr}\,j_{n+1/2}\,(kr)]}{dr}P_n^m(cos\theta)\begin{matrix}cos\\-sin\end{matrix}m\emptyset$$

where $P_n^m(cos\theta)$is the associated Legendre function of the first kind of orders n,m in cosθ and $j_{(n+1/2)}(k\rho)$is the first kind Bessel function of the order *n+1/2* and $k = \omega\sqrt{(\varepsilon\mu)}/c$ is the wavenumber. The fields outside the dielectric can be obtained by replacing Bessel functions with the Hankel functions of the second kind and by using the wavenumber in free space.

TM_{mn} mode formulas are the same when **E** and **H** fields are interchanged and the equations are multiplied by the wave impedance $\sqrt{(\mu/\varepsilon)}$.

The authors of [7] also give the characteristic equations for spherical resonators:

Mode TE_{mn}

$$\frac{j_{n-1/2}\,(kr)}{j_{n+1/2}\,(kr)} = \frac{h_{n-1/2}^2\left(\frac{kr}{\sqrt{\epsilon}}\right)}{\sqrt{\epsilon}h_{n+1/2}^2\left(\frac{kr}{\sqrt{\epsilon}}\right)}$$

Mode TM_{mn}

$$\frac{n}{kr} - \frac{j_{n-1/2}(kr)}{j_{n+1/2}(kr)} = \frac{n\epsilon}{kr} - \sqrt{\epsilon}\frac{h^2_{n-1/2}\left(\frac{kr}{\sqrt{\epsilon}}\right)}{h^2_{n+1/2}\left(\frac{kr}{\sqrt{\epsilon}}\right)}$$

The fundamental mode of a hemispherical DRA is TE_{11} mode and it produces a pattern similar to that of a short horizontal magnetic dipole whereas the TM_{10} mode results in a pattern similar to that of a short horizontal electric monopole.

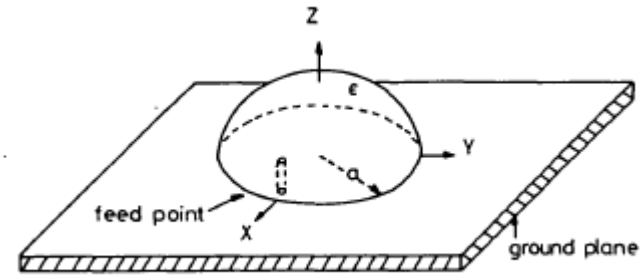

Fig. 2 TE111 mode excitation with probe [8]

In order to compute the resonance frequency corresponding to TE_{11} mode :

$$\frac{j_{1/2}(\sqrt{\varepsilon_r}k_0a)}{j_{3/2}(\sqrt{\varepsilon_r}k_0a)} = \frac{h^2_{1/2}(k_0a)}{\sqrt{\varepsilon_r}\,h^2_{3/2}(k_0a)} \tag{1}$$

The roots of the transcendental equation given in (1) is complex. Once the root (k_0a) is found, the resonance frequency $f_{11}$and the Q-factor of the resonator can be computed as [8]:

$$f(GHz) = \frac{Re(k_0a)}{a}\frac{c}{2\pi} = \frac{4.7713Re(k_0a)}{a(cm)} \tag{2}$$

$$Q = \frac{Re(k_0 a)}{2Im(k_0 a)} \tag{3}$$

Q-factor can also be defined as:

$$Q = \frac{2\omega W_e}{P} = \frac{2\omega W_e}{P_{loss} + P_{rad}}$$

If the dielectric material is selected such that the loss is negligible or so low that the material can be assumed to be lossless, the only power lost in the resonator will be radiating loss which means the Q-factor will be equal to the radiated Q-factor. $(Q = Q_{rad})$.

Hence it is worth mentioning that the Q-factor depends only on the mode and the dielectric constant (ϵ_r) of the sphere. The radiation Q-factor is plotted using the equations in [8] for TE_{11} and TM_{01} modes in Fig. 3 and Fig. 4, respectively.

The radiation Q-factor can also be related to the fractional impedance bandwidth of the antenna [9]:

$$BW = \frac{\Delta f}{f_0} = \frac{s-1}{\sqrt{s}Q} \tag{4}$$

As with TE_{11} mode, the resonant frequency and radiation Q-factor can be determined by solving the transcendental equation given below:

$$\frac{1}{\sqrt{\varepsilon_r}k_0 a} - \frac{j_{1/2}(\sqrt{\varepsilon_r}k_0 a)}{j_{3/2}(\sqrt{\varepsilon_r}k_0 a)} = \frac{\sqrt{\varepsilon_r}}{k_0 a} - \frac{\sqrt{\varepsilon_r}h_{1/2}^2(k_0 a)}{h_{3/2}^2(k_0 a)} \tag{5}$$

Equations (2), (3) and (4) are also valid for TM_{10} mode.

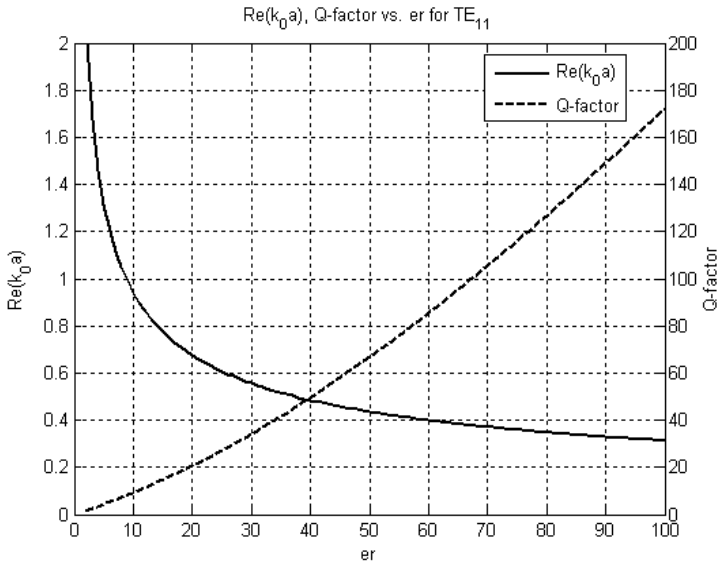

Fig. 3 Q-factor of the TE_{11} mode versus the dielectric constant

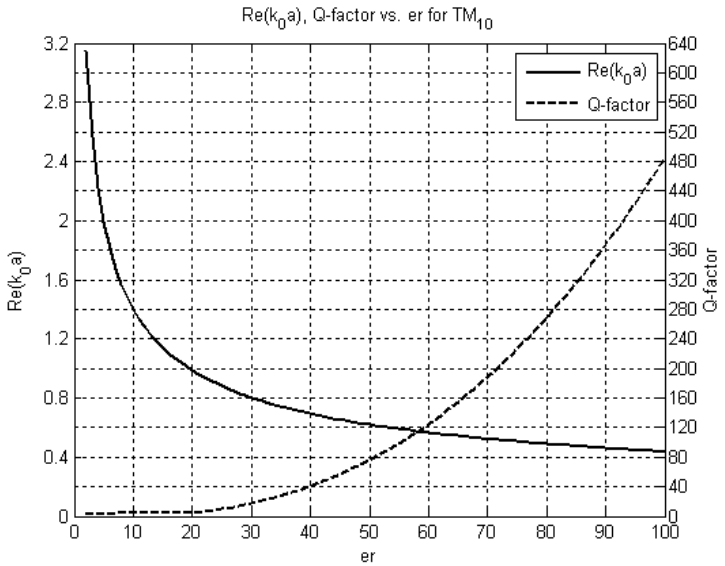

Fig. 4 Q-factor of the TM10 mode versus the dielectric constant

2.1.1 The Hemispherical DRA Design Procedure

The design procedure is straightforward:

- Specify the desired resonant frequency *f*, the fractional impedance bandwidth (BW), and the maximum Voltage Standing Wave Ratio (VSWR, s) in the band.
    - *Using* (4), *calculate Q-factor*.

- Determine the dielectric constant ϵ_r and corresponding $Re(k_0 a)$ using Fig. 3 for TE_{11} mode. For TM_{10} mode, ϵ_r can be determined using Fig. 4.

- Determine the radius of hemispherical DRA using (3).

2.2 The Cylindrical DRA

As mentioned in the hemispherical DRA section, the hemispherical shaped DRAs leave the designer with only one degree of freedom in choosing the design parameters, namely the radius of the sphere. In addition to the dielectric constant of the material, this radius determines both the resonant frequency, the radiation Q-factor, antenna size and impedance bandwidth. On the other hand, the cylindrical DRA can be characterized by its height *h*, radius a, and the dielectric constant of the material ε_r. These parameters determine $k_0 a$, the Q-factor so the impedance bandwidth and resonant frequency. Therefore the cylindrical shape offers one more degree of freedom than the hemispherical shape: the aspect ratio a/h.

The modes of cylindrical DRA can be divided into three families: electric dipole mode (also called TM to z mode) with azimuthal **H** field ($H_\emptyset$) and magnetic dipole mode with azimuthal **E** field ($E_\emptyset$), also hybrid HEM mode which is theoretically investigated in ref. [10] and computed in ref. [11] by using Method of Moments procedure. The HEM mode can be called HE if the E_z component is dominant or EH if the H_z component is dominant.

The most commonly used modes for radiating applications are $TE_{01\delta}$, $TM_{01\delta}$ and $HE_{11\delta}$ modes because of their high radiation efficiency. The mode subscripts refer to field variations in the azimuth ($\varnothing$), radial (r) and axial (z) directions, respectively. The field distributions for all these modes can be seen in Fig. 5.

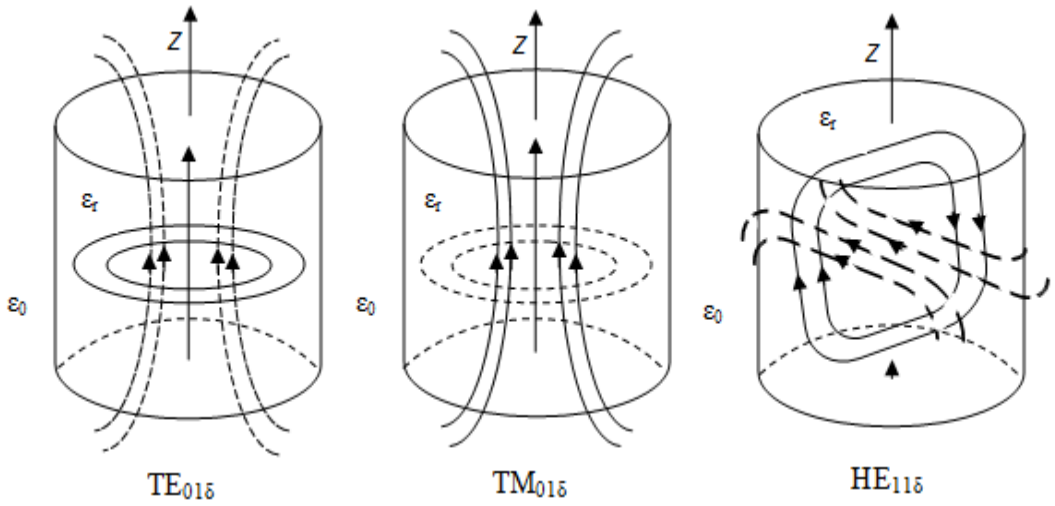

Fig. 5 E-field (solid lines) and H-field (dashed lines) distributions for three fundamental modes in a CDRA [12]

The $TE_{01\delta}$ mode radiates like a short magnetic monopole. The expressions for **E** and **H** are as [12]:

$$H_z = J_0(\beta r)\cos\left(\frac{\delta\pi z}{h}\right)$$

$$H_r = J_1(\beta r)\sin\left(\frac{\pi\delta z}{h}\right)$$

$$E_\varnothing = J_1(\beta r)\cos\left(\frac{\pi\delta z}{h}\right)$$

$$E_z = E_r = H_\varnothing = 0$$

where β can be obtained from the first zero of $J_0(\beta a)$.

These preceding results are valid under the conditions below:

- $H_z = 0$ is assumed at all surfaces parallel to z-axis. (PMC)
- The tangential components of **E** and **H** fields are continuous across the surfaces perpendicular to the z-axis.
- The electrical properties of the material is isotropic.
- The fields outside the resonator decay exponentially to zero at infinity.

The value of δ is defined as the fraction of a half-cycle of the field variation in the z-direction, ranges between zero and one and approaches one for high values of dielectric constant. According to Yee [13], δ/h satisfies the condition below:

$$\frac{\delta^2}{h^2} = \frac{4f^2}{c^2}(\epsilon_r - 1)\cos^2\left(\frac{\delta\pi}{2}\right) \tag{6}$$

where

$$\delta = \frac{h\zeta}{\pi} \tag{7}$$

and

$$\zeta^2 = \left(\frac{w}{c}\right)^2 \epsilon_r - \beta^2 \tag{8}$$

Given all parameters of the DRA (a, h, ϵ_r), the resonance frequency can be computed by solving (6) through the use of fixed point iteration method.

Alternatively, the resonance frequency can also be computed by iteratively solving the following equation [12]:

$$\tan^2\left(\frac{\beta h}{2}\sqrt{K_e-1}\right)=\frac{1-K^2}{K_e^2-1}$$

where $K=k/\beta$, $K_e=k_e/\beta$ and k, k_e are wave numbers in free space and in the dielectric medium, respectively.

The design of a cylindrical DRA requires determination of a, h, ϵ_r values to achieve a desired operating frequency and bandwidth. However determination of these parameters is not possible by using the formulas presented in this chapter. To help the design of cylindrical DRA, some empirical formulas that relate the resonance frequency and Q-factor of the DRA to ϵ_r and a/h ratio are proposed in [8]. These formulas are listed below for three different modes:

$TE_{01\delta}$ Mode:

$$f_{GHz}a=\frac{0.111}{\sqrt{\epsilon_r+1}}\left(1+0.2123\frac{a}{h}-0.00898\left(\frac{a}{h}\right)^2\right) \quad (9)$$

$$Q=0.078192\epsilon_r^{1.27}\left(1+17.31\frac{h}{a}-21.57\left(\frac{h}{a}\right)^2+10.86\left(\frac{h}{a}\right)^3-1.98\left(\frac{h}{a}\right)^4\right) \quad (10)$$

$TM_{01\delta}$ Mode:

$$f_{GHz}a=0.047746\frac{\sqrt{3.83^2+\left(\frac{\pi a}{2h}\right)^2}}{\sqrt{\epsilon_r+2}} \quad (11)$$

$$Q=0.00872\epsilon_r^{0.888413}e^{0.0397475\epsilon_r}\left(1-\left(0.3-0.2\frac{a}{h}\right)\left(\frac{38-\epsilon_r}{28}\right)\right) \quad (12)$$

$$x\left(9.498186\frac{a}{h}+2058.33\left(\frac{a}{h}\right)^{4.322261}e^{-3.50099\left(\frac{a}{h}\right)}\right)$$

$HE_{11\delta}$ Mode:

$$f_{GHz}a = \frac{0.30195}{\sqrt{\epsilon_r + 2}}\left(0.27 + 0.36\left(\frac{a}{2h}\right) - 0.02\left(\frac{a}{2h}\right)^2\right) \quad (13)$$

$$Q = 0.01007\epsilon_r^{1.3}\frac{a}{h}\left(1 + 100e^{-2.05\left(\frac{a}{2h} - \frac{1}{80}\left(\frac{a}{h}\right)^2\right)}\right) \quad (14)$$

2.2.1 The Cylindrical DRA Design Procedure

The design procedure is more complex than it was in the hemispherical section due to the more degree of freedom the designer has. One more degree of freedom introduces more solutions into the problem with more trade-offs between bandwidth, VSWR, resonant frequency and the DRA dimensions. On the other hand the number of solutions can be significantly decreased by limiting one or more of these design parameters.

The design procedure is explained below:

- Specify the desired resonant frequency *f*, the fractional impedance bandwidth (BW), and the maximum VSWR (s) in the band.
    - *Using* (4), *calculate Q-factor*.

- Specify the mode to obtain the desired radiation pattern. Using the related mode formulas (10), (12) or (14) specify the possible values of dielectric constant ϵ_r that satisfies the required Q-factor.

In order to choose the possible ϵ_r value, the variation of Q-factor with respect to a/h ratio needs to be plotted for various ϵ_r values. Such a plot can be found in Fig. 7 for $HE_{11\delta}$ mode. It can be observed from the figure that if one needs a Q-factor of 20, the dielectric constant should be chosen to be smaller than 50 for a feasible design.

Since there is no unique solution for a given Q-factor the designer has two different paths for the design procedure. These paths are itemized as:

- Determine the dielectric constant and obtain several a/h values from the mode formulas (9), (11), (13). For each different a/h values, there is a unique a and a unique h, *or*

- Determine or limit the dimension values and the ratio according to the dimensional restrictions, set the dielectric constant of DRA material.

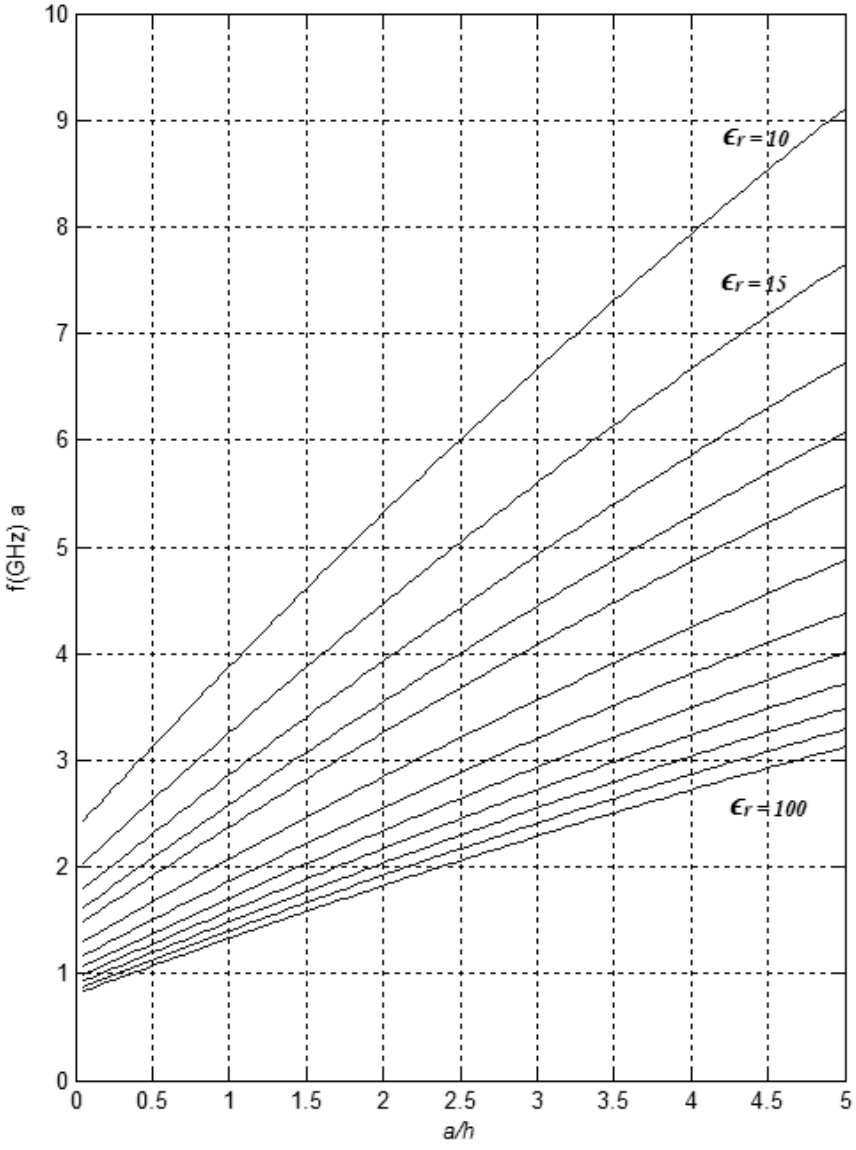

Fig. 6 $f_0 a$ of the $HE_{11\delta}$ mode of the cylindrical DRA

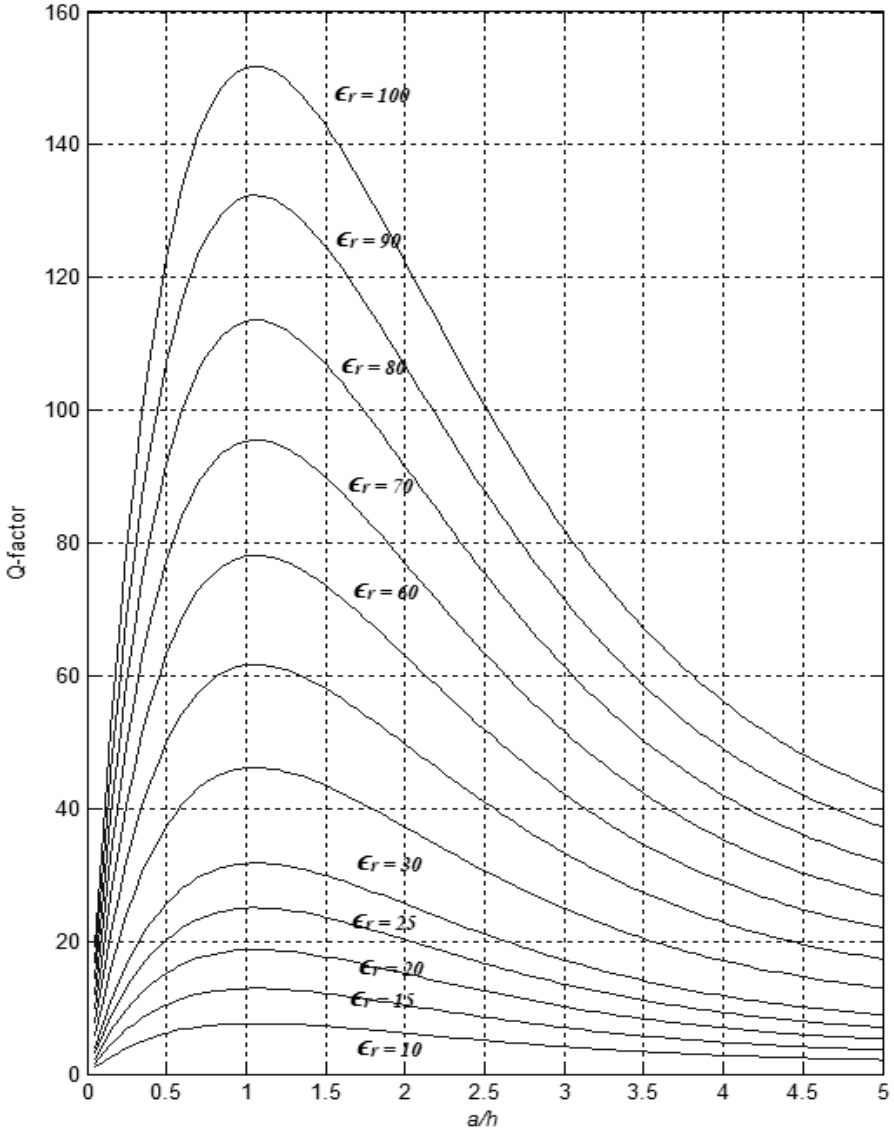

Fig. 7 Q-factor of the $HE_{11\delta}$ mode of the cylindrical DRA

2.3 The Rectangular DRA

Literature survey shows that the investigations reported on rectangular-shaped DRA's are less than that of the investigations reported on the previous shapes like hemispherical and cylindrical DRAs. However, rectangular DRA's offer practical advantages over cylindrical and hemispherical DRAs. For example, by choosing the rectangular DRA dimensions properly, it is easier to avoid the excitation of higher order modes. Consequently the performance of the antenna improves since higher order modes result in larger cross-polarization levels.

The rectangular DRA is characterized by a height *h,* a width *w,* a depth *d,* and a dielectric constant ϵ_r. as shown in Fig. 8. The rectangular shape offers one more degree of freedom for the design of DRA since two aspect ratios of a rectangular DRA (height/length and width/length) can be chosen independently. Thus, it provides a greater flexibility in terms of bandwidth control.

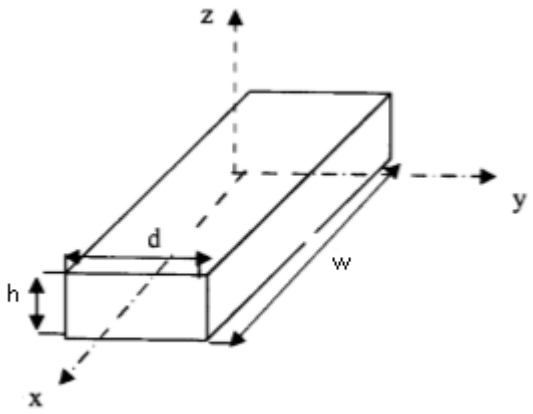

Fig. 8 Rectangular Dielectric Resonator Antenna (RDRA)

According to Van Bladel [14] modes of a DR can be confined or nonconfined type. The following condition is satisfied at all the surfaces of DR for both confined and nonconfined modes.

$$\mathbf{E} \cdot \hat{\mathbf{n}} = \mathbf{0} \tag{15}$$

E denotes the electric field intensity and $\hat{\mathbf{n}}$ is the normal to the surface of the resonator. This is the first condition of PMC boundaries.

On the other hand, the boundary condition related to the tangential component of the magnetic field intensity;

$$\hat{\mathbf{n}} \times \mathbf{H} = \mathbf{0} \tag{16}$$

is not satisfied at all the surfaces of DR by all modes. *Confined* modes are the modes which satisfy both conditions while *nonconfined* modes can only satisfy (15). The lowest order *nonconfined* and *confined* modes radiate like magnetic and electric dipoles, respectively. Van Bladel also showed that *confined* modes can only be supported by dielectric bodies of revolution such as spherical and cylindrical. A rectangular DR as not being a body of revolution can support *nonconfined* modes only.

The field solution for rectangular DRA is given in Appendix A in details. The fields are solved using a modified dielectric waveguide model (DWG) which is called truncated dielectric waveguide model. In order to obtain a relation for the resonance frequency, the model imposes magnetic wall conditions on the planes parallel to the direction of wave propagation while assuming that the waves are exponentially decaying beyond the planes perpendicular to the direction of wave propagation.

The resonance frequency for TE_{11} to x (TE_{11}^{x}) mode (Fig. 9) can be solved using the transcendental equation below:

$$k_x \tan\left(k_x \frac{w}{2}\right) = \sqrt{(\varepsilon_r - 1)|k_0|^2 - k_x^2} \tag{17}$$

where k_x is the wave number in x direction.

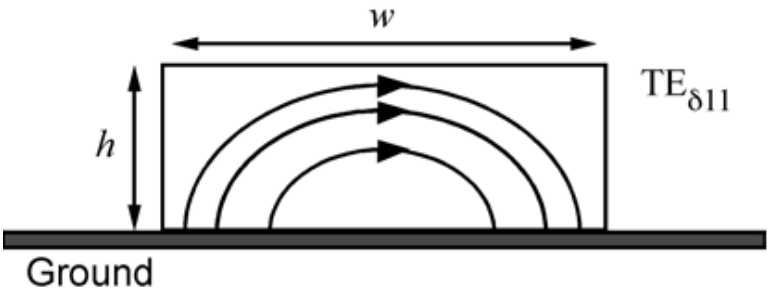

Fig. 9 RDRA TE_{11} mode E field distribution [8]

The solution of (17) requires a graphical or numerical approach. Alternatively, the numerical solutions which are derived by several curve fittings can also be used to determine the resonant frequency [8]. In [8] a normalized frequency F is defined as:

$$F = \frac{2\pi w f_0 \sqrt{\varepsilon_r}}{c} \tag{18}$$

If f_0 is taken in GHz and w in cm then the expression reduces to:

$$F = \frac{\pi w_{cm} \sqrt{\varepsilon_r}}{15 f_{0(GHz)}} \tag{19}$$

By choosing curve fitting approach, the normalized frequency can be approximated in terms of aspect ratios of the DRA:

$$F = a_0 + a_1 \left(\frac{w}{b}\right) + a_2 \left(\frac{w}{b}\right)^2 \tag{20}$$

where

$$a_0 = 2.57 - 0.8 \left(\frac{d}{b}\right) + 0.42 \left(\frac{d}{b}\right)^2 - 0.05 \left(\frac{d}{b}\right)^3 \tag{21}$$

$$a_1 = 2.71\left(\frac{d}{b}\right)^{-0.282} \tag{22}$$

$$a_2 = 0.16 \tag{23}$$

Note that the resonant frequency f_0 depends on $b,\ d/b$ and w/b, whereas it depends on radius $a,\ a/h$ for cylindrical DRA and on radius only a for hemispherical DRAs.

As for hemispherical and cylindrical DRAs, the Q-factor determines the constraints for ratios d/b and w/b. To obtain the expression for Q-factor, the stored energy and the radiated power need to be calculated.

The radiation Q-factor is defined as:

$$Q = \frac{2\omega_0 W_e}{P_{rad}} \ where\ \omega_0 = 2\pi f_0$$

For TE_{11}^{x} mode the stored energy is defined in [15] as:

$$W_e = \frac{\epsilon_0 \epsilon_r wbdA_{11}^2}{32}\left(1 + \frac{\sin(k_x w)}{k_x w}\right)\left(k_y^2 + k_z^2\right)$$

where A_{11} is the mode amplitude and the radiated power is:

$$P_{rad} = 10k_0^4|\boldsymbol{p_m}|^2$$

where $\boldsymbol{p_m}$ the magnetic dipole moment expressed in closed form as:

$$\boldsymbol{p_m} = -\frac{j\omega 8\varepsilon_0(\varepsilon_r - 1)A_{11}}{k_x k_y k_z}\sin\left(\frac{k_x w}{2}\right)\hat{\boldsymbol{a}}_x$$

A general expression linking the unloaded Q-factor to the antenna geometrical features is [16]:

$$Q \propto 2w_0\varepsilon_r^p \left(\frac{Volume_{DRA}}{Surface_{Dra}}\right)^s \qquad p > s \geq 1 \tag{24}$$

In design procedure, generally the normalized Q factor is used and is defined as:

$$Q_e = \frac{Q}{\varepsilon_r^{3/2}} \tag{25}$$

The relation between normalized Q-factor, d/b and w/b cannot be obtained analytically, instead graphical method is more convenient. The variation of normalized Q-factor with respect to d/b aspect ratio for $w = b$ is presented in Fig. 10 for different permittivity values taken from ref. [17]. Similar graphs for different w/b aspect ratios are also given in Fig. 11 and Fig. 12.

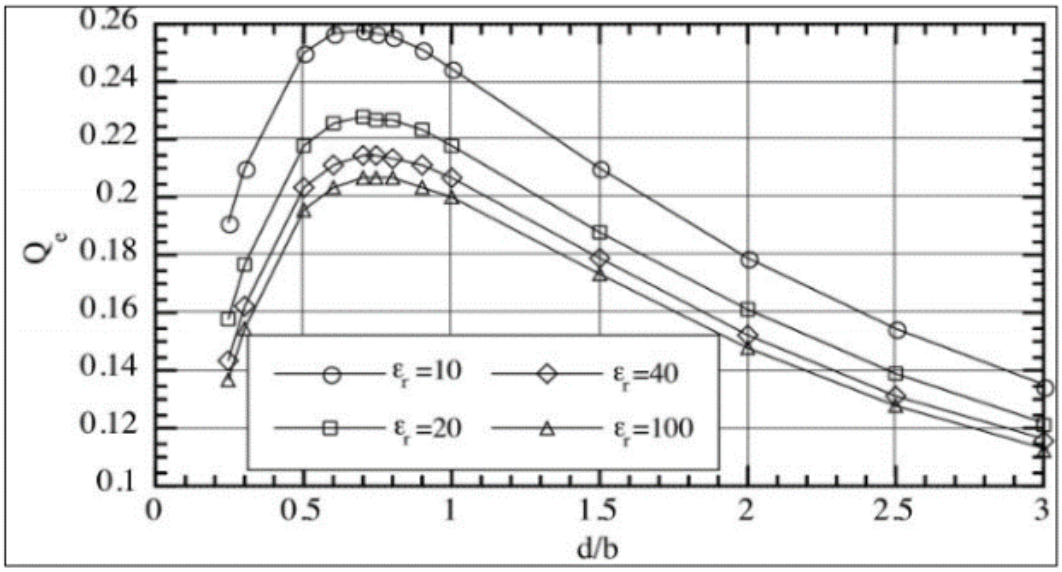

Fig. 10 Normalized Q-factor of a RDRA for w=b.

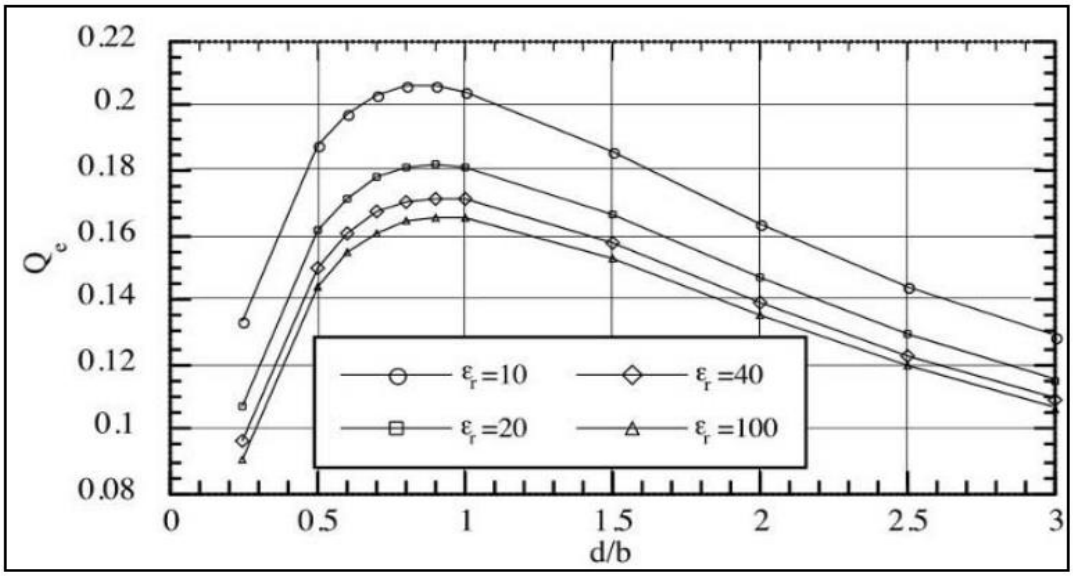

Fig. 11 Normalized Q-factor of a RDRA for w=2b.

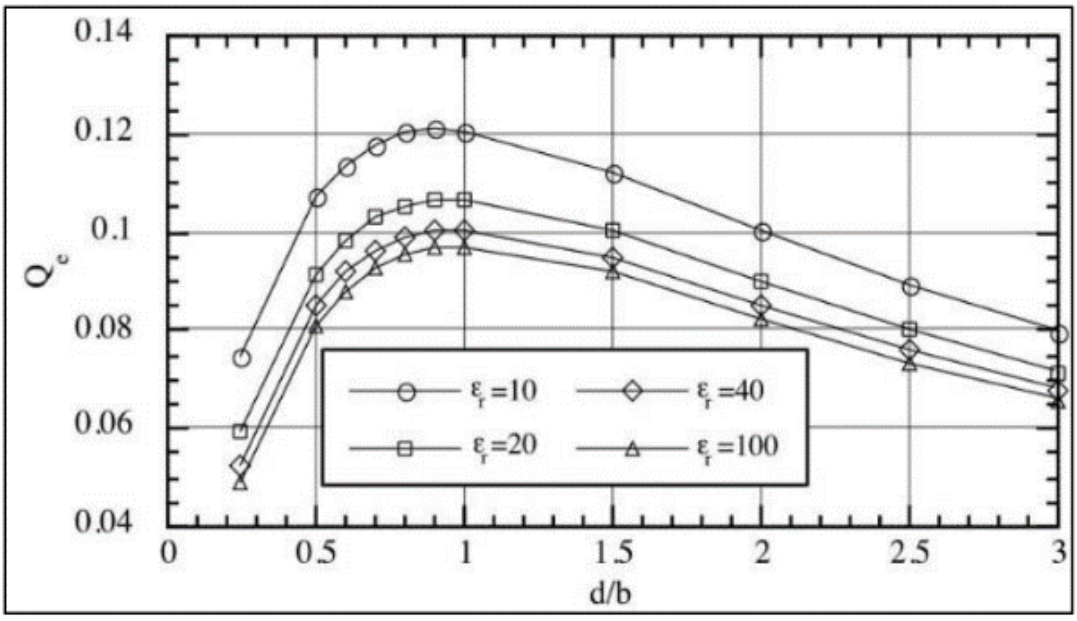

Fig. 12 Normalized Q-factor of a RDRA for w=4b

As it will be summarized in the next section, rectangular DRAs can be designed by using these graphs.

The Rectangular DRA Design Procedure

The design procedure of rectangular DRA is more involved than the case for cylindrical DRA. This is due to two more degrees of freedom the designer has. On the other hand, the number of possible solutions is larger than that of a cylindrical DRA thus the designer can handle trade-offs between geometry, impedance bandwidth and resonant frequency more easily.

The design procedure is explained below:

Step 1:

- Specify the desired resonant frequency *f*, the fractional impedance bandwidth (BW), and the maximum VSWR (s) in the band.
    - *Using* (4), *calculate Q-factor*.

Step 2:

- Choose a dielectric constant and calculate the normalized Q-factor, by using (25). Using Fig. 10 - Fig. 12 check whether the dielectric constant is suitable or, in other words, check if there is any possible aspect ratios d/b and w/b to meet the required bandwidth for the chosen dielectric constant. To maintain maximum flexibility, choose a dielectric constant that provides more solutions.

Step 3:

- Using Fig. 10 - Fig. 12, determine d, w, b values.

Since there are more degrees of freedom, the last two steps of the design procedure can be interchanged. For example, the designer can begin the design procedure assigning one dimension and calculates dielectric constant and other dimensions.

2.4 Other DRA Shapes

The major limitation of DRAs is the relatively narrow bandwidth. Therefore DRAs with various shapes are proposed in literature [18]-[21] to enhance their bandwidths.

In [18], sectored cylindrical DRA as shown in Fig. 13 is proposed to reduce the volume. Thus, by lowering the Q-factor, an increase in bandwidth can be achieved.

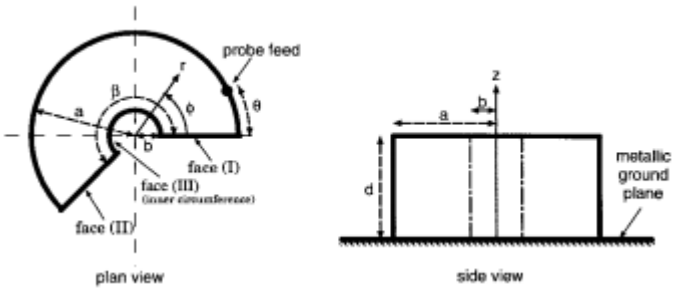

Fig. 13 General geometry of circular sector DRA. According to [18] sector faces can be mettalic plates or left open.

A sectored antenna occupying 75% less volume than a conventional cylindrical antenna operating 1.68-2.30 GHz frequency band is reported.

The notched DRAs presents a central air gap to offer a larger impedance bandwidth Fig. 14. According to [19], aperture-fed notched rectangular DRAs have demonstrated an increase in impedance bandwidth by 28%.

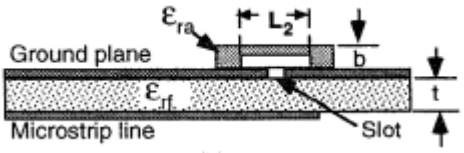

Fig. 14 Geometry of the notched rectangular DRA [19]

In [20] an ultrawideband omnidirectional antenna is presented. Ultrawideband is achieved by adjusting the individual resonant frequencies of both the monopole and the ring DRA. The feed scheme is also simple since only a coaxial probe is needed. A coaxial probe excites the monopole antenna together with the ring DRA as shown in Fig. 15.

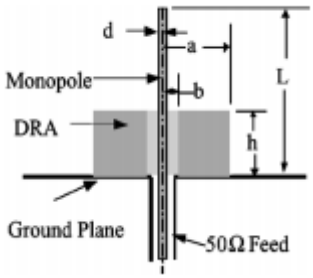

Fig. 15 Geometry of the monopole and the ring DRA [20]

In [21] an increase in bandwidth of microstrip patch is obtained. As reported in ref. [21], a microstrip patch antenna with an impedance bandwidth of 5.68 – 5.86 GHz is loaded by a DRA with an impedance bandwidth of 5.10 – 5.42 GHz to obtain an overall impedance bandwidth of 21% from 5.30 – 6.55 GHz.

CHAPTER 3

FEED SCHEMES

For an antenna to radiate in practical applications of any use, the radiating energy must be coupled into the element through input ports. The coupling scheme includes the type of port and the location of the port with respect the DRA and determines the amount of coupling χ together with the operating mode generated. The mode or modes generated induce the radiation pattern. For this reason, it is important to determine the mode required before following the design procedures. Each mode generates different field distribution over the DRA. The location is to be determined depending on the current distribution on the DRA for the predetermined mode.

Lorentz Reciprocity Theorem is utilized in defining the amount of coupling [22].

The theorem states that in an enclosed system of two electric and magnetic sources, the field along the source other than its primary source is equal to the other field along its source. Related mathematical expression is as follows:

$$\oiint_{S} (\boldsymbol{E_1 x H_2 - E_2 x H_1}) \cdot \boldsymbol{dS} = \oiiint_{V} (\boldsymbol{E_2 \cdot J_1 - E_1 \cdot J_2 - H_2 \cdot M_1 - H_1 \cdot M_2}) \boldsymbol{dV}$$

Which reduces to:

$$\iiint_{V} (\boldsymbol{E_1 \cdot J_2 - H_1 \cdot M_2}) \boldsymbol{dV} = \iiint_{V} (\boldsymbol{E_2 \cdot J_1 - H_2 \cdot M_1}) \boldsymbol{dV}$$

E_1 along J_2 is equal to E_2 along J_1. Since in our system there is only one source (electric or magnetic) the amount of coupling can be defined as follows

For an electric source:

$$\chi = \iiint_V (E_2 \cdot J_1) dV \tag{26}$$

For a magnetic source:

$$\chi = \iiint_V (H_2 \cdot M_1) dV \tag{27}$$

Above equations (26) and (27) state that the source, electric or magnetic, must be placed so that the dot products yield the maximum amount. In the other words, in order to achieve strong coupling, the source must be located in an area where:

- Field strength is strong,
- Field is in the same direction with the source.

According to coupling theory, the coupling mechanism also has a loading effect on the Q-factor of the DRA. The loading effect is generally defined as Q_{ext} and expressed as:

$$Q_{ext} = \frac{Q}{\chi}$$

The relation between loaded Q factor (Q_L), Q and Q_{ext} can expressed as:

$$Q_L = \left(\frac{1}{Q} + \frac{1}{Q_{ext}}\right)^{-1} = \frac{Q}{1+k}$$

Loaded Q-factor can be adjusted to a desired value however maximum amount of coupling is achieved when χ approaches to unity which is called critical coupling.

In next sections, several feed methods will be discussed.

3.1 Coaxial Probe Feed

One of the most preferred feed mechanisms is using a probe. Depending on the probe location, various modes can be excited. In this thesis, probe excitation is only used in simulation platform to see the effects. For a selected probe, there are two parameters that can be adjusted in order to achieve the desired amount of coupling

- Probe height
- Probe location

After manufacturing, adjusting probe height is relatively easier than adjusting the probe location. If the probe is located somewhere within the DRA, to vary the location the DRA must be drilled. Optimizing the height is more applicable since it is easy to trim the probe.

Several simulations were done in the beginning of the work to study probe coupling.

In this thesis stacked DRA configurations are also studied in order to investigate their bandwidth performance. Since the field distributions for a single cylindrical DRA were already presented in Chapter 2, the simulation studies are performed for a 3 layer stacked DRA within a probe at center as shown in Fig. 16. This structure is simulated by using FEM based EM simulation software ANSYS HFSS. The E field distribution is presented in Fig. 17.

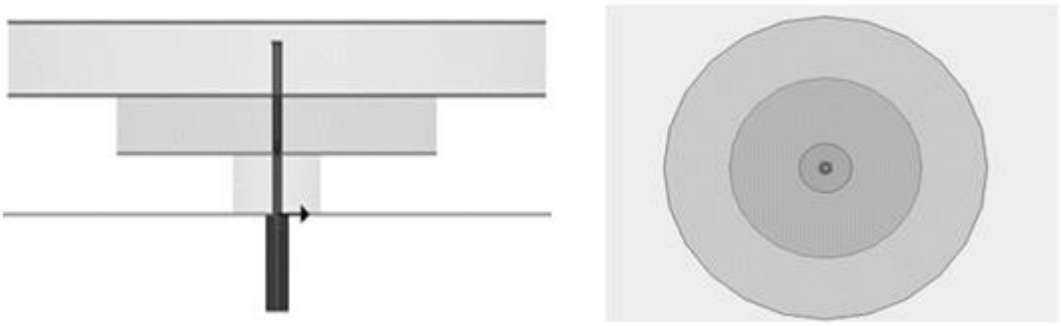

Fig. 16 3-Stacked Cylindrical DRA with centered probe feed

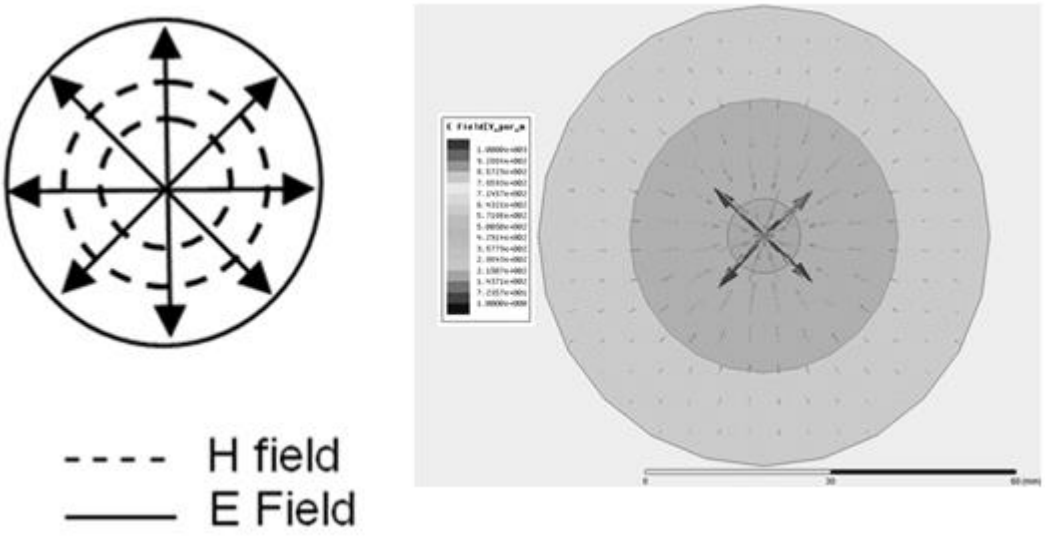

Fig. 17 Field distribution of $TM_{01\delta}$ mode of CDRA

Since the probe is a current source, it must be placed at the center to achieve the strongest coupling.

On the other hand, the side coupling as shown in Fig. 18 excites TE mode. $TE_{11\delta}$ mode electric field distribution is given in Fig. 19a.

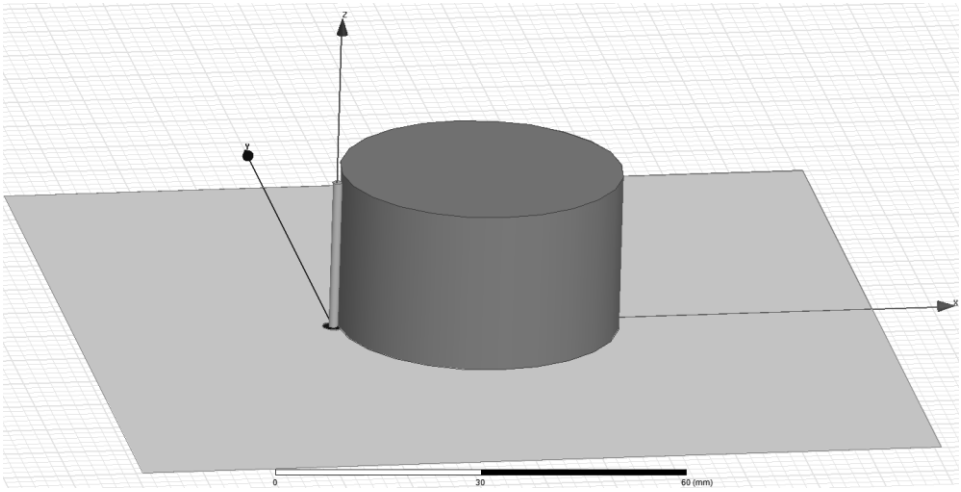

Fig. 18 Probe excitation from the side of CDRA

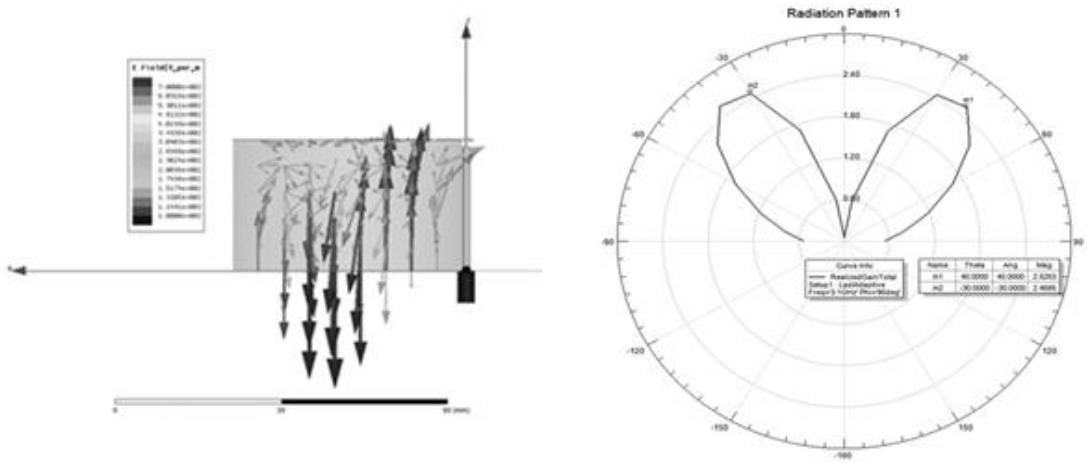

a b

Fig. 19 $TE_{11\delta}$ mode field distribution (a) and corresponding radiation pattern (b)

The radiation pattern for $TE_{11\delta}$ mode is shown in Fig. 19b. As expected from the field distribution with odd symmetry, the radiation pattern exhibits a null at broadside direction.

3.2 Slot Coupled Microstrip Line Feed

A slot on the ground plane is used to achieve the coupling between microstrip line and the DRA. Different slot shapes can be used to excite the DRA, the small rectangular is the most widely used. Having the feed network below the ground plane isolates the radiating element from any unwanted coupling or spurious radiation from the feed.

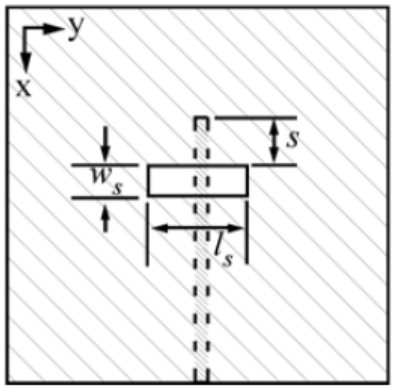

Fig. 20 Slot coupled microstrip line feed geometry

There are more than two parameters to optimize the coupling, slot dimensions (l_s, w_s) and slot location under the DRA.

Following relations can be used for initial slot dimensions [8]:

$$l_s = \frac{0.4\lambda_0}{\sqrt{\varepsilon_{DRA}}}, \quad w_s = 0.2 l_s$$

And the stub extension:

$$s = \frac{\lambda_g}{4}$$

Generally it is necessary to tune slot dimensions and stub extension. The approximation of above formulas will be discussed in DRA design section.

A slot under the microstrip line behaves as magnetic source. Thus, the slot must be located at the area where the magnetic field is strong. The electric field distribution and the corresponding equivalent magnetic source for slot apertures is given in Fig. 21.

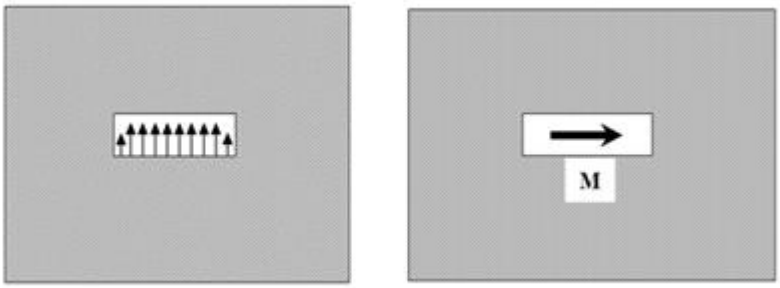

Fig. 21 E-field distribution over slot and equivalent magnetic source

TE^x mode for RDRA has H-field distribution is given in Fig. 22. As in the figure, the slot is placed under RDRA so that the magnetic source and the H field lines are aligned. The feed location is adjusted to obtain maximum coupling.

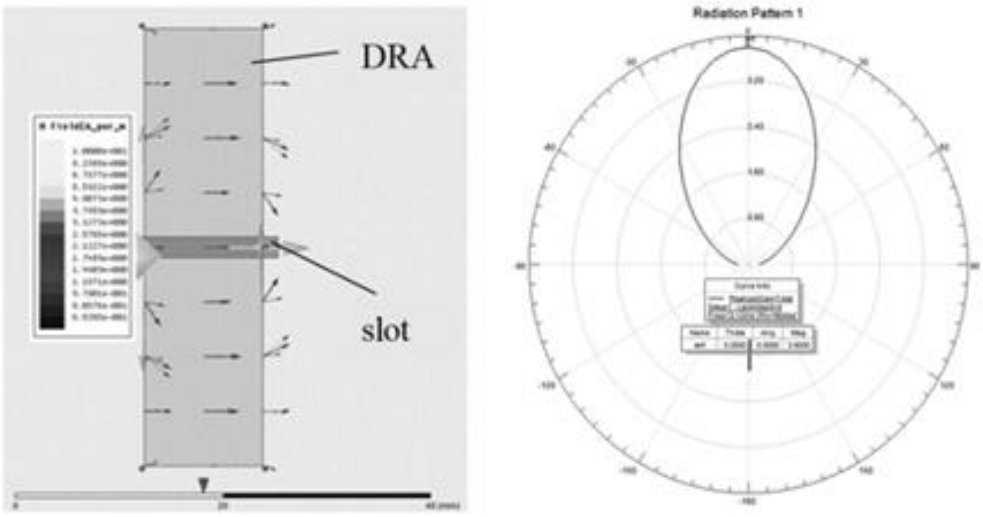

Fig. 22 TE^x mode H-field distribution of RDRA and corresponding radiation pattern

For the case of $HE_{11\delta}$ mode of CDRA, the electric field distribution is given in Fig. 23. Magnetic fields lines are perpendicular to E-field lines. As in RDRA feed adjustment, the slot is placed so that the magnetic source and H field lines are aligned in the same direction.

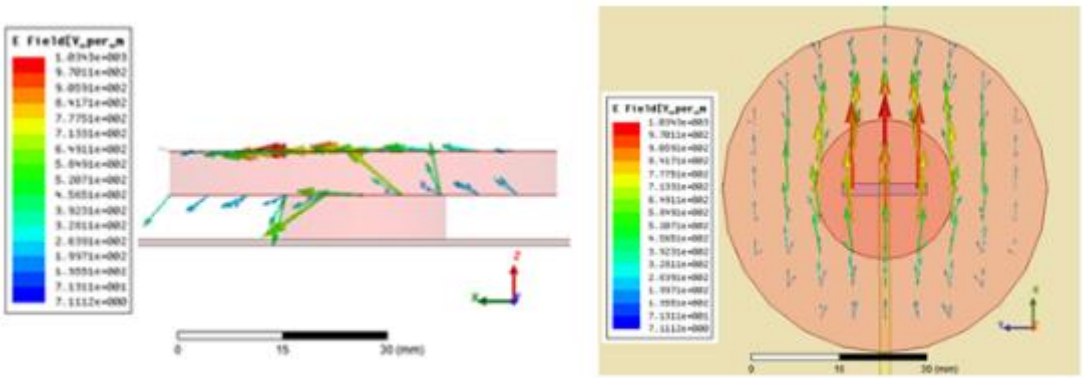

Fig. 23 $HE_{11\delta}$ mode of SCDRA

Slot aperture is used for both Stacked Cylindrical DRA and Rectangular DRA designs. In this thesis, slot coupled microstrip line feed is preferred due to its flexibility in design, convenience for array applications and ease of manufacturing.

3.3 Microstrip Line Direct Feed

A DRA is placed on a microstrip line [23]. Since the DRA is placed over the substrate, the image theory cannot be applied directly. In the structure the substrate also plays a significant role in determining the resonant frequency. This is due to the loading effect of substrate on DRA. Thus, in the design procedures, all the calculations must be carried on the base of the effective dielectric constant ϵ_{eff} instead of ϵ_{DRA} in order to obtain well-approximated results.

There is only one parameter that can be adjusted for direct feed (with fixed characteristic impedance) in order to achieve desired coupling.

s: the length of the line underneath the DRA.

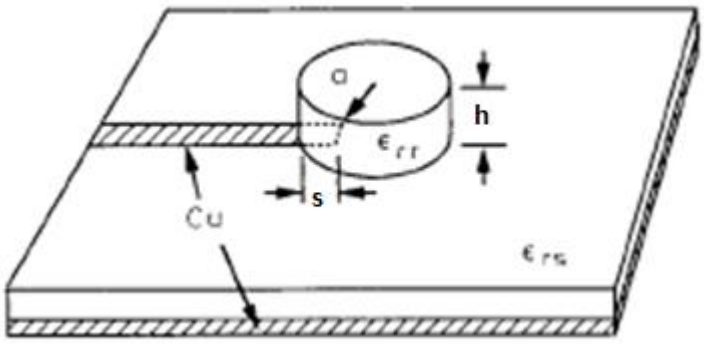

Fig. 24 CDRA design parameters [23]

The dielectric constant of DRA, ϵ_{DRA} is more dominant factor for the degree of coupling. For high values of ϵ_{DRA}, it is easy to achieve strong coupling; however, the

maximum amount of coupling reduces dramatically if the dielectric constant of the DRA is lowered. This problem may be hard to overcome if a low dielectric constant is necessary to obtain a wideband characteristic. A convenient way to overcome the problem is to use a multi segment DRA (MSDRA) [24] structure as in Fig. 25. An insert material is used under the DRA. The insert acts as an impedance transformer between DRA and the microstrip line. Fields inside the insert are more concentrated which improves the coupling performance. The same mechanism is utilized by stacked circular DRA which will be discussed in design section. The fields are more concentrated inside the part that close to the slot. Thus, greater bandwidths can be obtained.

The author of [24] also proposes a modified dielectric waveguide model to analyze MSDRAs. According to the report, the effective permittivity and effective height must be substituted into the formulas in Chapter 2.

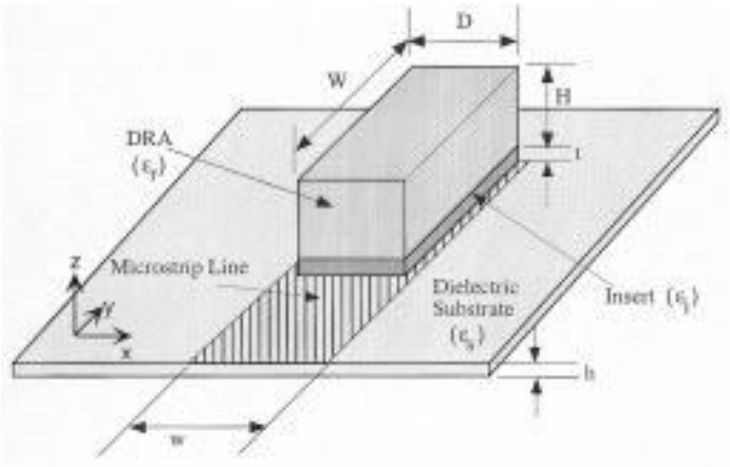

Fig. 25 Multi segment DRA on a Microstrip Line [24]

$$\epsilon_{eff} = \frac{H_{eff}}{\frac{H}{\epsilon_r} + \frac{t}{\epsilon_i} + \frac{h}{\epsilon_s}}$$

and the effective height:

$$H_{eff} = H + t + h$$

One practical disadvantage is, some microstrip substrates are not eligible for DRAs to be mounted on. Adhesives may not be suitable for Teflon (PTFE) based materials. Alignment problems may arise if the DRA cannot be mounted properly.

There are more coupling mechanisms for DRA using, Co-Planar Feeds, Dielectric Image Guides (DIG) etc. These mechanisms will not be discussed in this thesis.

CHAPTER 4

DESIGN OF DIELECTRIC RESONATOR ANTENNAS

In Chapter 2, the field modes that can be excited in rectangular and circular DRAs were studied. Moreover, the procedures for the design of such antennas were presented. It was pointed out that for rectangular and cylindrical DRAs there was not a unique design for a given operation frequency and bandwidth. For example for a cylindrical DRA, the same frequency and bandwidth requirement can be achieved by different height and radius couples. There may be some additional design constraints on antenna size due to mechanical requirements. Hence, the antenna designer may need to perform the design procedure several times in order to end up with a design that satisfies all these requirements. Consequently the need for a design software arises to avoid repetitive hand calculations in this iterative design procedure.

C Sharp (C#) programming language is used on Microsoft Visual Studio platform to develop such a design software. Two different software tools are developed for cylindrical and rectangular DRAs. For cylindrical DRA, a graphical interface is introduced as shown in Fig. 26. Once the dielectric constant value is entered the software plots the Q-factor vs. a/h ratio graph for three fundamental operating modes ($TE_{01}, TM_{01}, HE_{11}$) by using the equations presented in Chapter 2. By means of graphical plots, users will have a better way in understanding the Q-factor behavior with respect to dimensional parameters. When the required center frequency, bandwidth and voltage standing wave ratio (VSWR) value are set the corresponding Q value is calculated and this Q value is also plotted on the Q-factor vs. a/h plot.

When the designer marks any point on the plot with the cursor radius (a) and height (h) values corresponding to that point are given as the output.

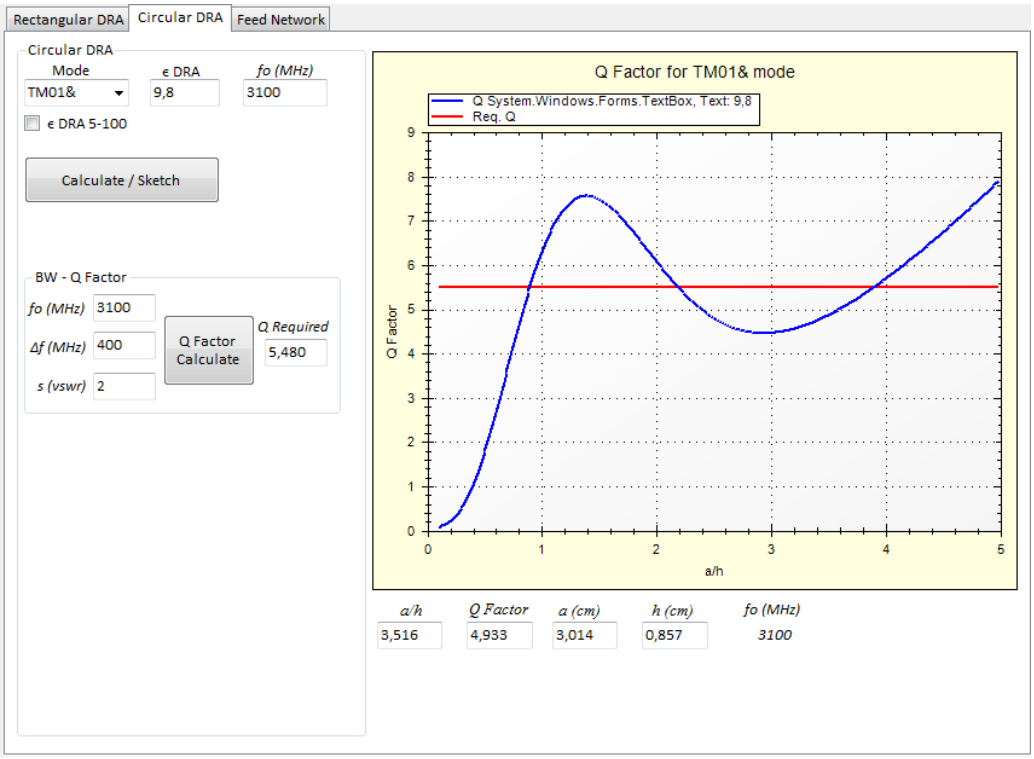

Fig. 26 DRA design tool, Circular DRA Design Section

For the same dielectric constant (9.8) and the same required Q-factor (5.48), the Q-factor vs. a/h ratio variations are plotted for three fundamental modes in Fig. 27-Fig. 28 for comparison. Since any Q-factor value lower than the required Q-factor (i.e. larger bandwidth) provides a feasible solution for the design it can be observed that HE_{11} mode offers more design flexibility. Moreover, TE_{01} and TM_{01} modes exhibit a null in broadside direction whereas HE_{11} mode has maximum radiation in broadside direction. Therefore HE_{11} mode is evaluated to be the most suitable mode for the designs considered in this thesis.

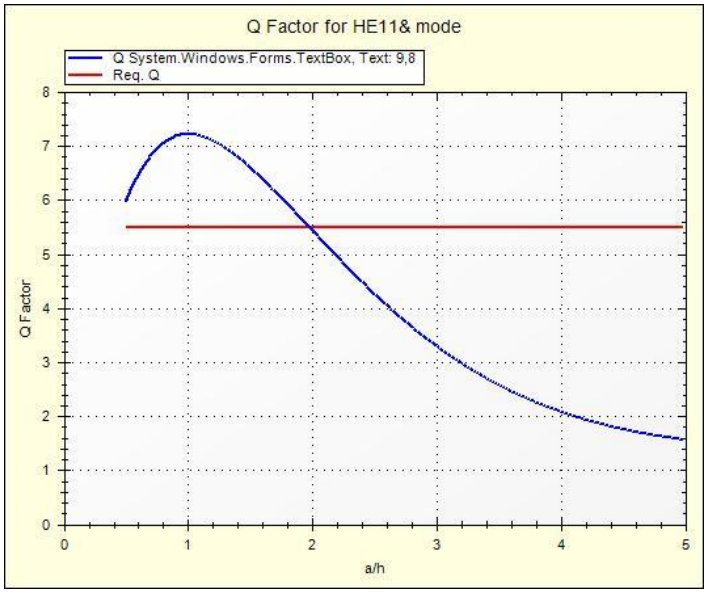

Fig. 27 Q-factor vs. a/h for HE11 mode of CDRA

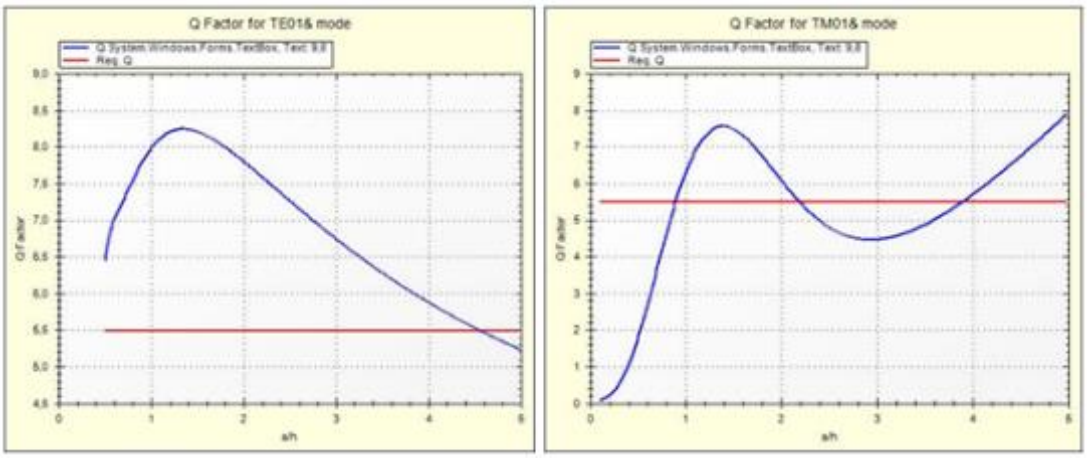

Fig. 28 Q-factor for TE01 and TM01 modes of CDRA

If a dielectric constant is not specified then Q-factor vs. a/h ratio plots for different values of the dielectric constant (between 5 and 100) can be observed as seen in Fig. 29. This feature helps the designer to choose a different dielectric material.

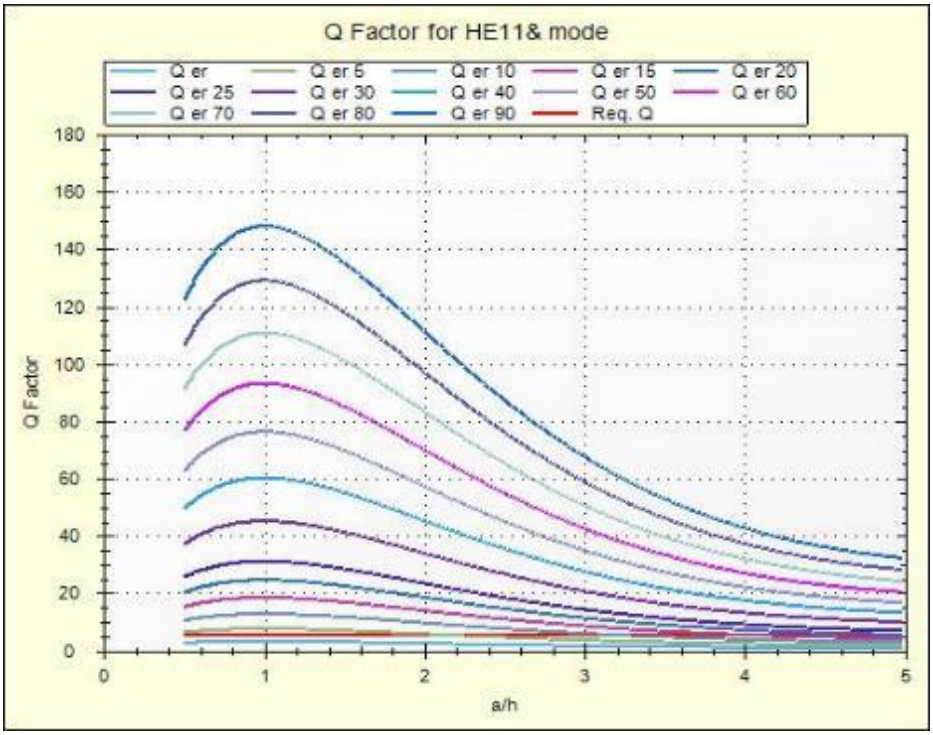

Fig. 29 Q factor vs. a/h for different values of ϵ_{DRA}

The software for the rectangular DRA is developed based on the formulas presented in Chapter 2 for the TE^x mode of the resonator. Since the Q-factor depends on two different aspect ratios for the rectangular DRA a graphical interface was not possible for this case.

The aspect ratios are selected using the graphs in rectangular DRA design section of the Chapter 2. After determining proper aspect ratios (w/b and d/b) for a required Q-factor, the designer inputs the ratio values into the software. The software then calculates the normalized frequency, F and corresponding dimension values using the expressions given in Chapter 2.

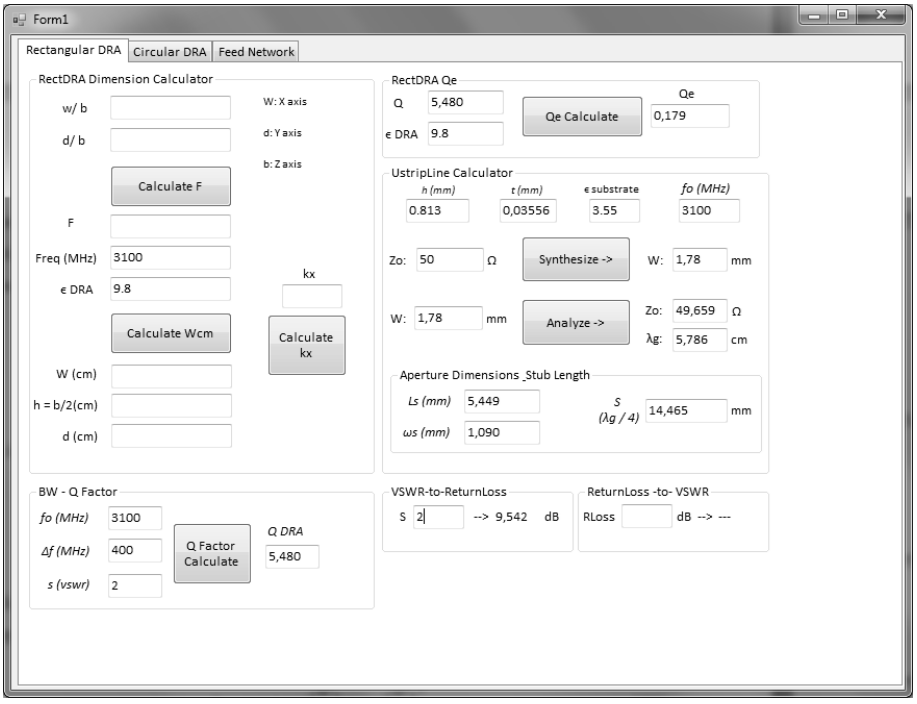

Fig. 30 DRA design tool, rectangular DRA design section

The initial values for slot dimensions are also calculated using the design software. The design equations introduced in Chapter 2 were empirical formulas and they were obtained using curve-fitting method. Due to this approximate approach in the design procedure the designed antennas need to be analyzed by using a full wave analysis method for an accurate characterization. Also the dimensions of the antenna should be optimized according to the results obtained from the electromagnetic field (EM) simulator. In this thesis FEM based full-wave solver HFSS by ANSYS is used for EM simulations. In the following sections these design examples will be presented. For each design the initial antenna dimensions are determined by the developed software then these dimensions are fine-tuned using HFSS.

4.1 Design of Rectangular DRA (RDRA)

In this thesis, following specifications are considered in designing DRA elements:

- Frequency band: 2.9 GHz – 3.3 GHz ($f_0 = 3100\ MHz, \Delta f = 400$ MHz)
- Return loss $\leq 10dB$ ($VSWR = 2$)
- The dimensions of DRA elements must be suitable to be used as a linear array element.
- For ease of the beam-forming network design, the DRA is to be fed by means of an aperture coupled microstrip line.

Due to the availability of the material the dielectric constant is chosen to be 9.8.

By using the design software the initial dimensions of the rectangular DRA are chosen as:

$$w = 4.783\ cm$$

$$h = \frac{b}{2} = 1.195\ cm$$

$$d = 1.076\ cm$$

The simulations of this rectangular DRA (RDRA) is performed in HFSS by using the model presented in Fig. 31.

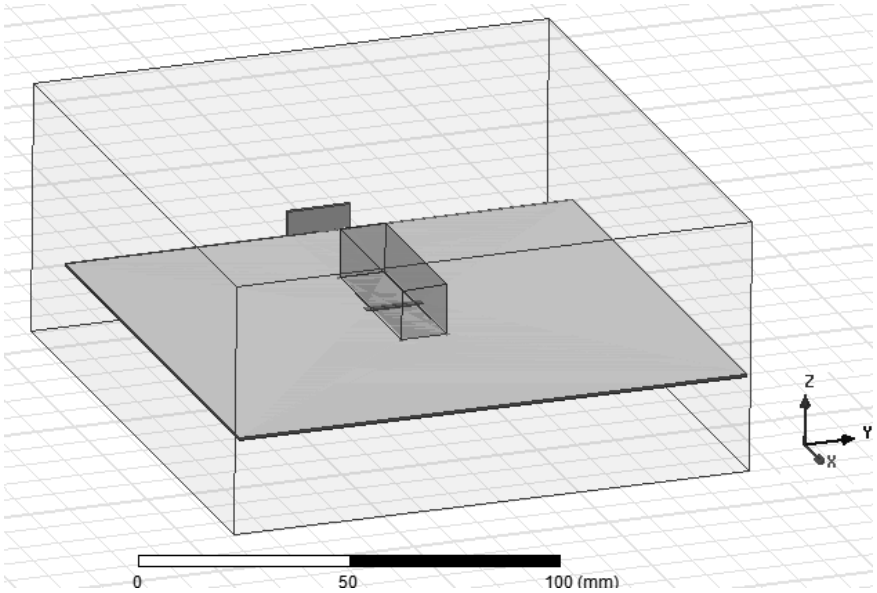

Fig. 31 RDRA HFSS model, antenna side

An optimization of the dimensions were required to meet the design specifications. The optimized antenna dimensions are as follows:

$$w = 4.25 \text{ cm}$$

$$h = b/2 = 1.27 \text{ cm}$$

$$d = 1.15 \text{ cm}$$

According to simulations, the return loss below 10dB is in 2.8-3.3GHz frequency range as shown in Fig. 32. The 10dB return loss bandwidth is obtained as 16.4%. It can also be seen that the operation band of the DRA designed by using the dimensions obtained using design tool is very close to the projected frequency band. After a fine tuning in HFSS, the RDRA became capable of operating in the required frequency band.

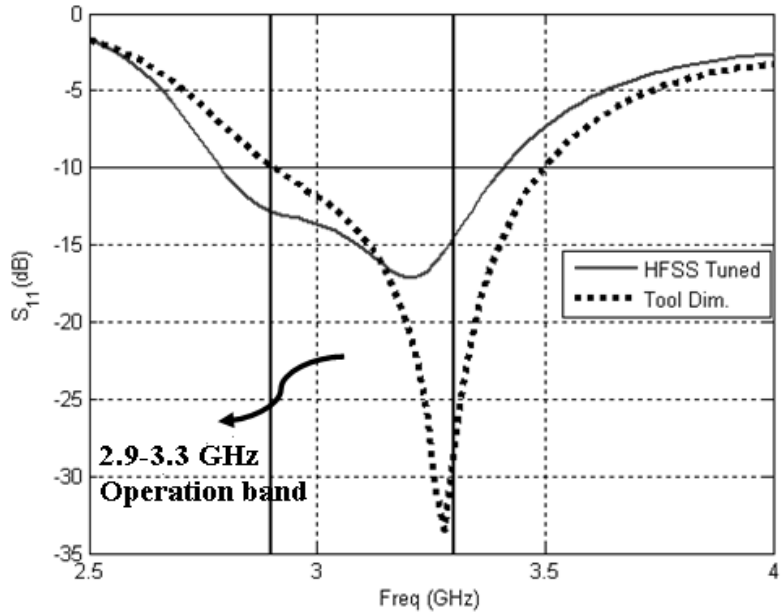

Fig. 32 The return loss curves for tuned DRA and DRA with design tool dimensions

Simulated input impedance of the optimized RDRA vary around 50Ω. A good matching is observed in the 2.8-3.4GHz band.

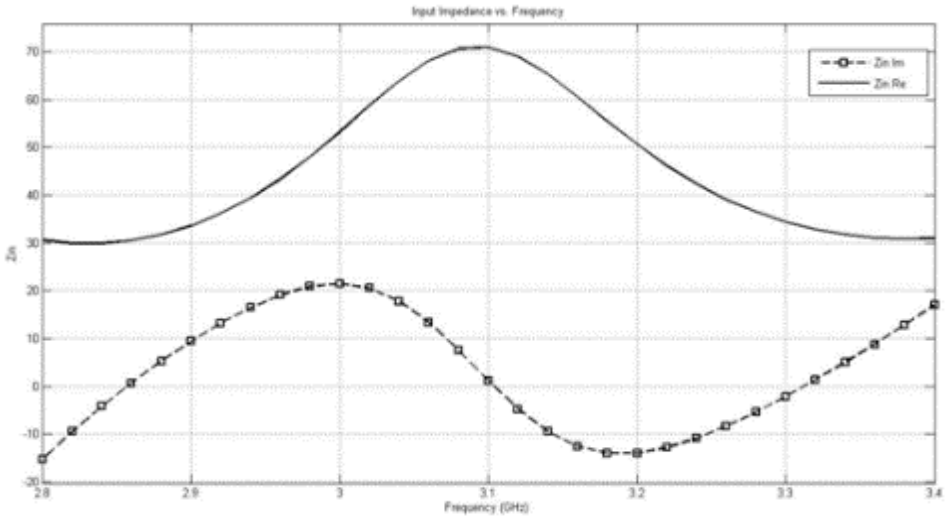

Fig. 33 Impedance vs. frequency for optimized rectangular DRA

The gain of RDRA is 5.71dB at broadside with 3-dB beamwidth of 78° and 125° at H-plane and E-plane, respectively.

The co-polar and the cross-polar far field patterns are presented in Fig. 35 and Fig. 36 for E and H planes, respectively. The cross-polarized field level is 52dB below the co-polarized field in broadside direction in each plane. Within 3dB beamwidth, cross-polarization level is more than 25dB below the co-polarized level. The polarization purity observed in simulation results may be due to single mode excitation. Front-to-back ratio is 14.63dB. The back radiation may be due to both the finite ground plane and the radiation of the slot. If needed this back radiation could be eliminated by placing a second ground plane under the feeding structure.

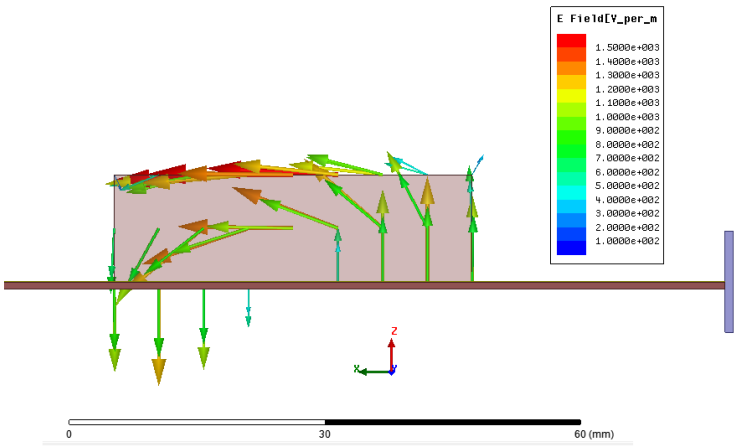

Fig. 34 RDRA simulated TE mode E-field distribution

The field distribution of TE_{11} mode of the RDRA is consistent with the field distribution shown in Fig. 9 of Chapter 2.

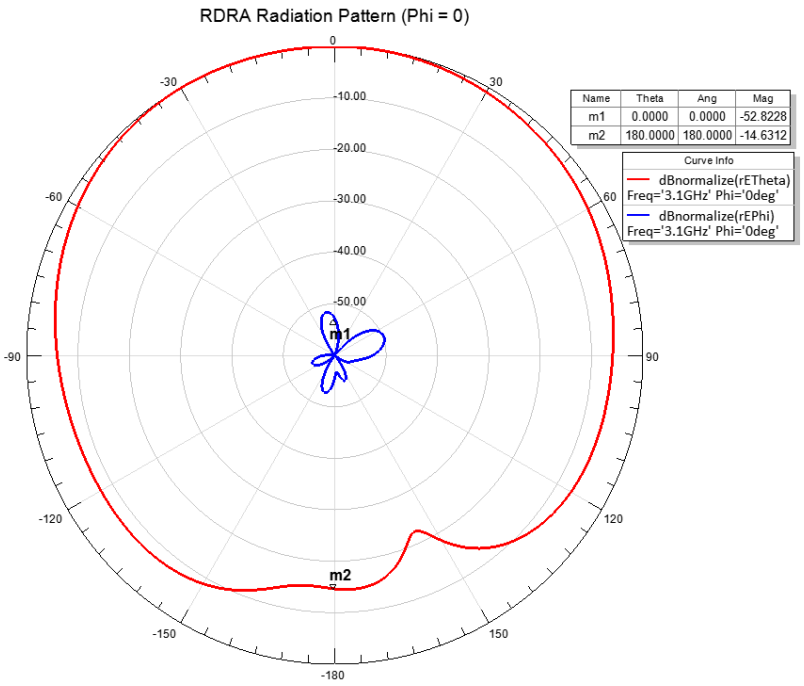

Fig. 35 Co-polar and cross-polar components at E-plane ($\emptyset = 0°$)

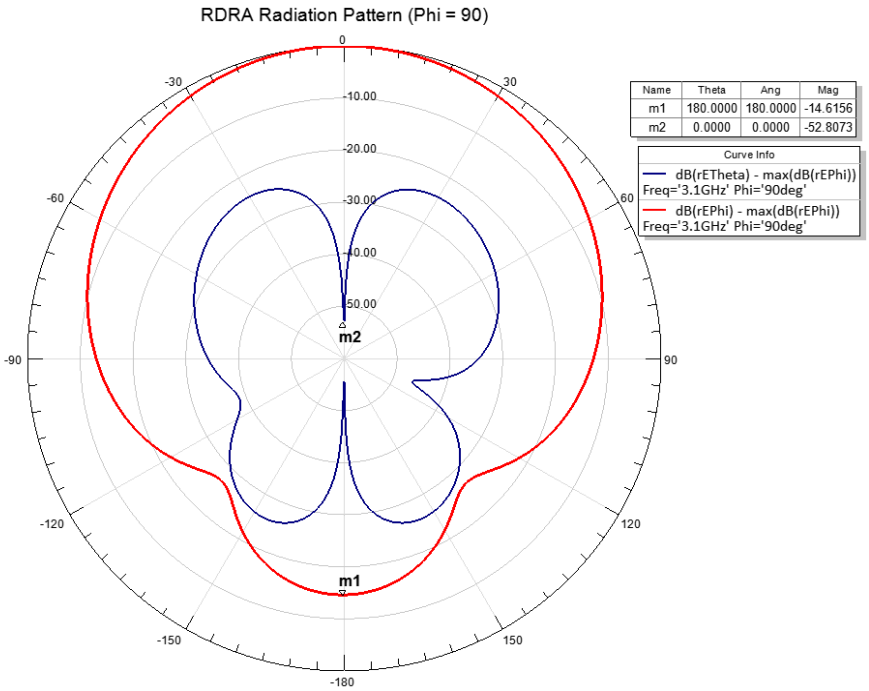

Fig. 36 Co-polar and cross-polar components at H-plane ($\emptyset = 90°$)

4.2 Design of Cylindrical DRA (CDRA)

The same specifications also apply for the Circular DRA.

As discussed in the first section of this chapter HE_{11} mode is chosen and the initial antenna parameters are calculated by the design software as:

$a = 27.27\ mm,\ \ h = 7.8\ mm$

After optimizing these parameters through HFSS simulations (by using the model in Fig. 37) for a better matching, the resulting dimensions are:

$a = 28\ mm,\ \ h = 7.62cm$

The design tool provides good approximations for the dimensions of CDRA.

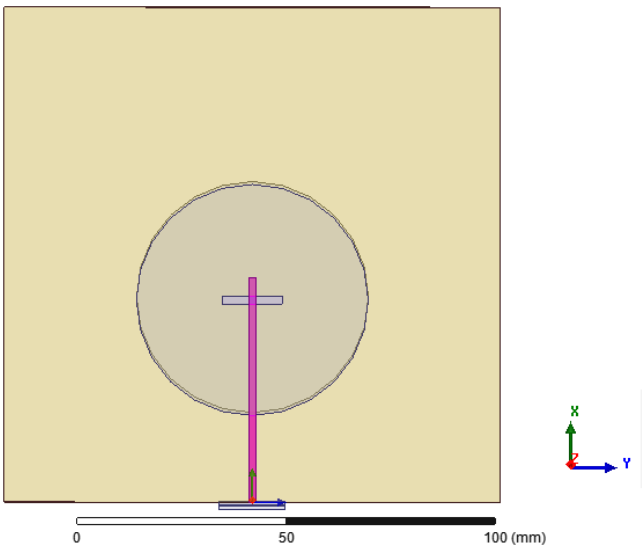

Fig. 37 Microstrip line under the substrate and the slot on the ground plane

The return loss characteristics are shown in Fig. 38. The resonant frequency is found to be 3.1 GHz. A 10dB return loss bandwidth of 2.84 - 3.35GHz is obtained. 16.4% of impedance bandwidth is achieved with fundamental cylindrical shape without

practicing any bandwidth enhancement method.

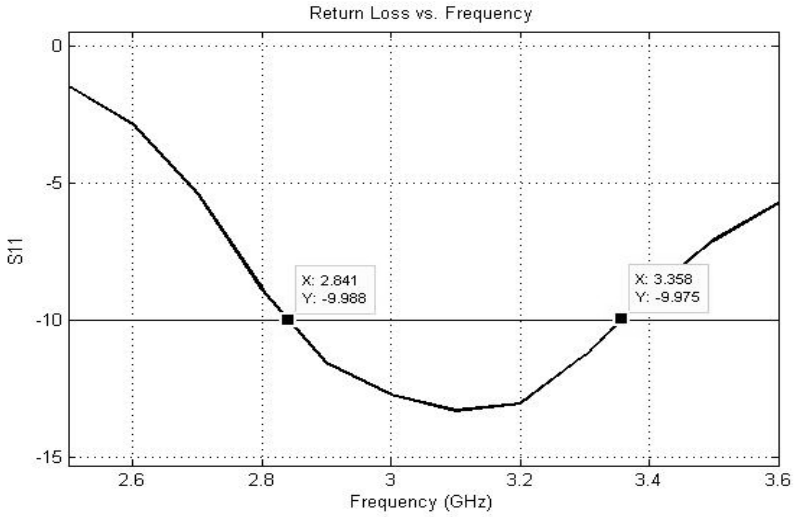

Fig. 38 Return loss of CDRA

The electric field distribution at 3.1GHz is shown in Fig. 39:

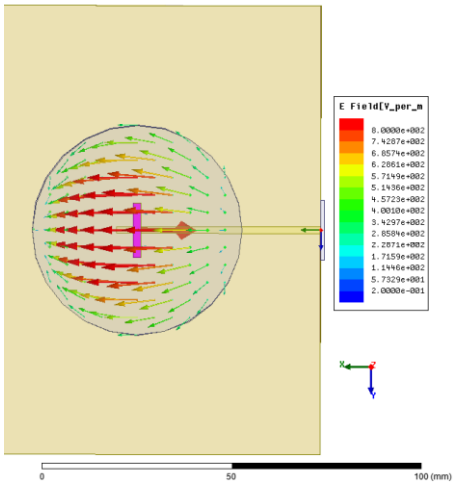

Fig. 39 E-field distribution over CDRA for HE11 mode

The gain of the antenna is 4.81dB at broadside with 3dB beamwidth of 74° and 145° at H-plane and E-plane, respectively. The increase of 20° in beamwidth at E-plane with respect to RDRA, affected adversely CDRA by lowering the gain by 0.9dB. However the antenna gain of the antenna can be further optimized for a better matching by adjusting the microstrip line segment extension beneath the substrate.

The co-polar and the cross-polar far field patterns are presented in Fig. 41, Fig. 40 for E and H planes, respectively. The cross-polarized field level is 60dB below the co-polarized field in broadside direction in each plane. Within 3dB beamwidth, cross-polarization level is more than 25dB below the co-polarized level. Front-to-back ratio is 13.88dB.

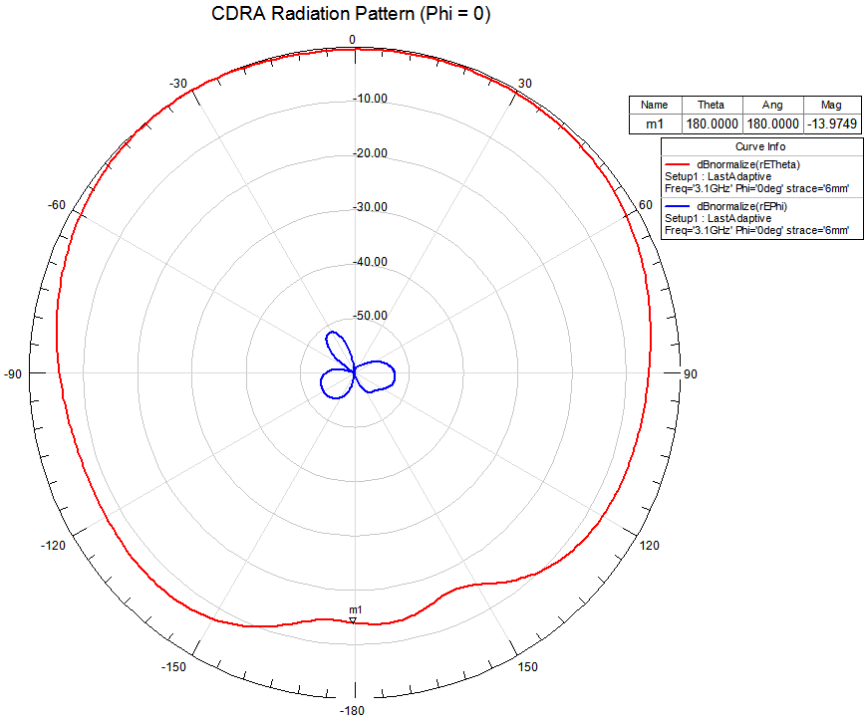

Fig. 40 Co-pol and Cross-pol components of E-field at E-plane

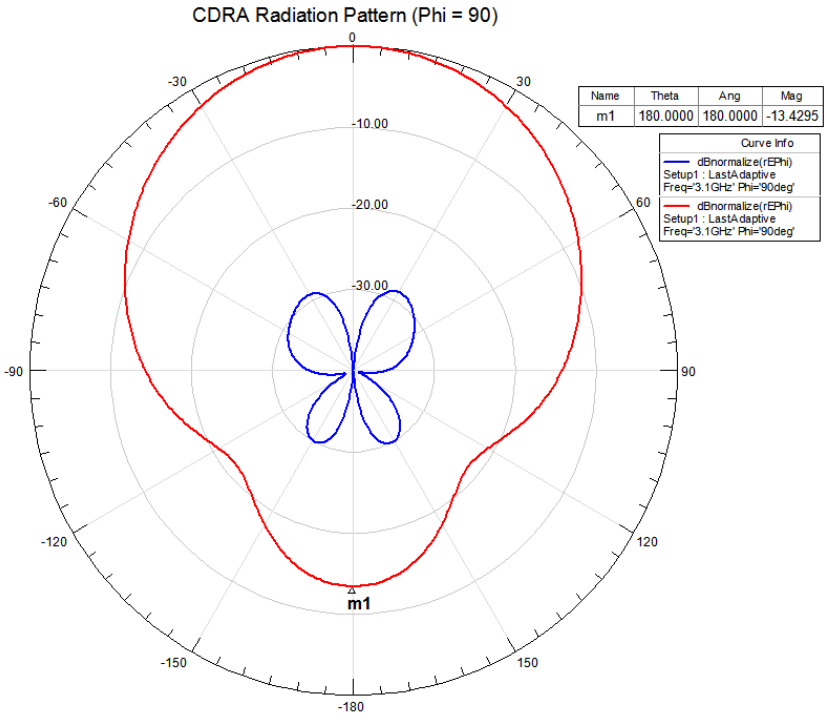

Fig. 41 Co-pol and Cross-pol components of E-field at H-plane

4.3 Design of Stacked Cylindrical DRA (SCDRA)

As stated in previous section, the cylindrical DRA is designed without utilizing any bandwidth or coupling improvement technique. An enhanced amount of coupling can be obtained by stacking DRAs. Through a stacked DRA configuration (Fig. 42) an enhanced coupling rate is achieved by concentrating fields near the coupling port as seen in Fig. 43, where the field distributions in SCDRA and CDRA are compared. This approach involves stacking DRAs on top of each other to realize such effect. In our case a slot is used as the coupling port. The bottom part is excited by a slot, while the upper part is electromagnetically coupled. Hence, the bottom part of SCDRA comprises the fields more concentrated when compared to the upper part.

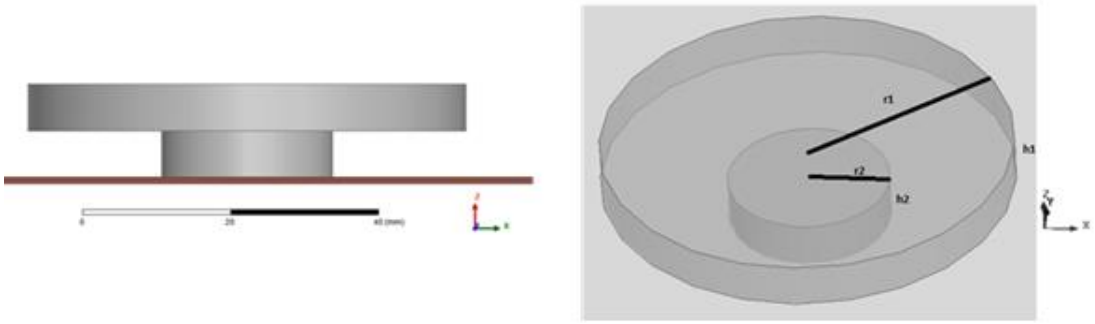

Fig. 42 Side and top view of SCDRA

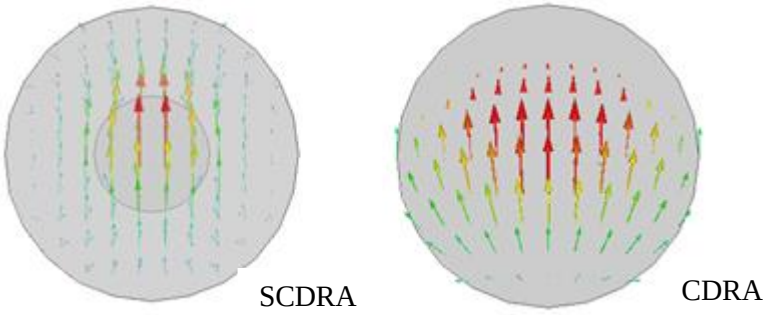

SCDRA CDRA

Fig. 43 E-Field distributions on SCDRA and CDRA

One thing to consider when designing SCDRA is that a compact design may not be possible. As it will be seen in this section, the upper part is slightly wider in diameter than the basic shaped CDRA.

Unlike the CDRA, the SCDRA does not have a straightforward design procedure. This is due to the quantity of design parameters. The radius and the height of both cylinder sections have effect on the resonant frequency.

For the design of SCDRA in this thesis, the heights are fixed to a constant value of

6.35mm since the material selected was Rogers TMM10i which has a dielectric constant of 9.8 and thickness 6.35mm.

For thicker materials the design becomes more compact. However, this requires a 3D shaping of the material. Since the height is fixed to the thickness of the substrate, only a drilling machine is sufficient for production.

The theoretical design is made by using the design software. The corresponding Q-factor for a CDRA with total height of 12.7 mm is 7.2. This exceeds the required Q-factor (5.48) which is calculated in previous section. However, Q-factor can be lowered by varying dimension values. The radius of bottom CDRA is decreased while the radius of the upper part is increased. The input impedance variation with respect to these dimension variations is observed through HFSS simulations.

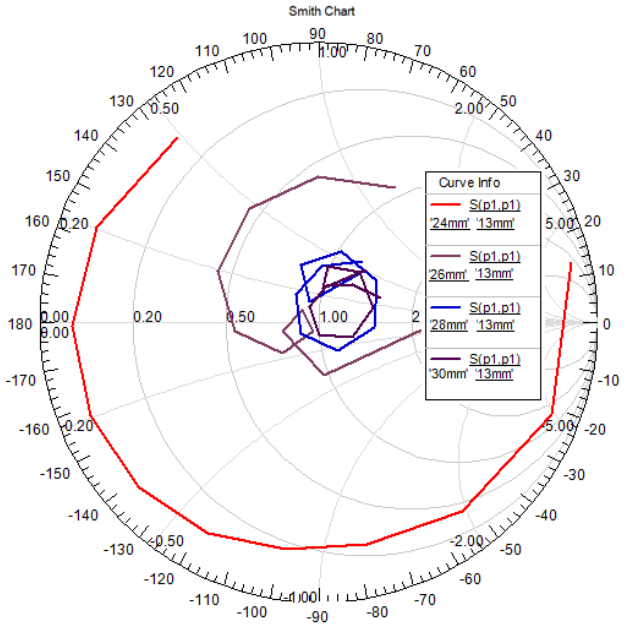

Fig. 44 Input impedance variation with respect to the radius of top DRA

For a fixed radius (13mm) on the bottom part, the impedance loci for different values of the radius for the upper section are shown in Fig. 44. The optimum value (for

largest bandwidth) for upper radius is 30mm.

Next, while the top radius is fixed at 30mm, the radius of the bottom section is varied between 10 and 13 mm. An 11.75mm of radius for bottom part exhibits the largest bandwidth as shown in Fig. 45.

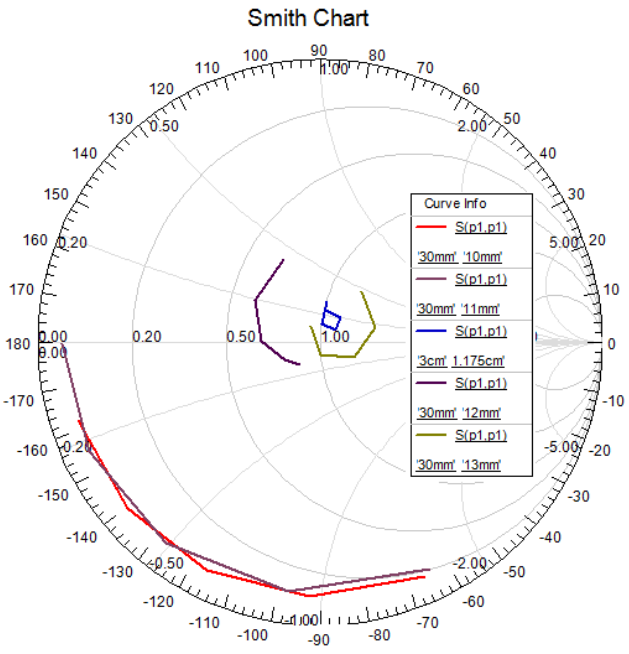

Fig. 45 Input impedance variation with respect to the radius of bottom DRA

The return loss of the antenna is plotted in Fig. 46. It can be deduced that extra resonances are introduced by using the stacked configuration.

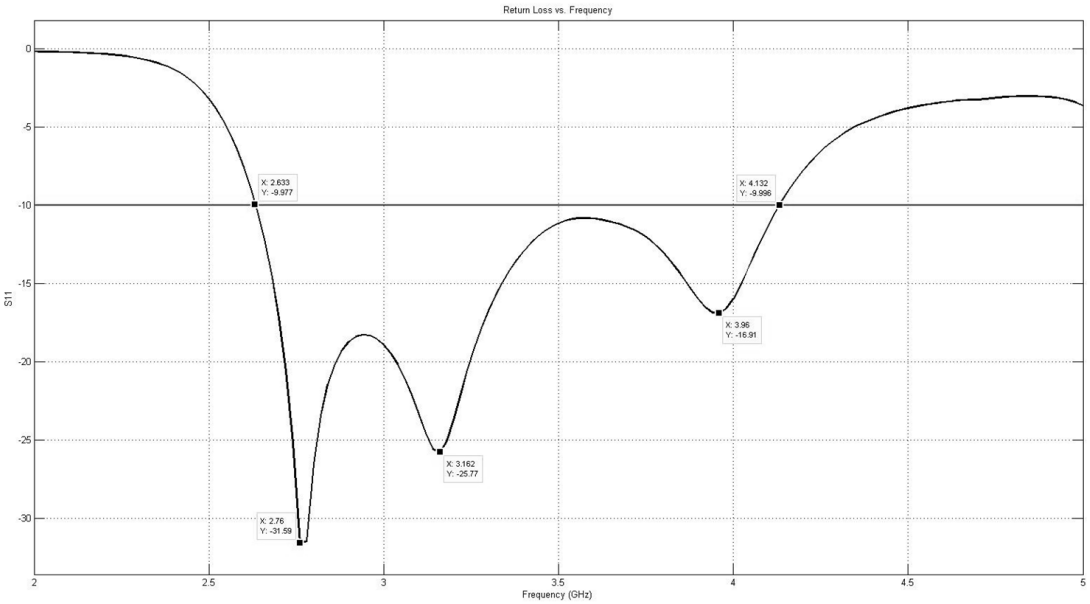

Fig. 46 10-dB impedance bandwidth of SCDRA

The stacked cylindrical design resulted in an increase in the 10dB return loss bandwidth from 16.4% (2.84 - 3.35GHz) to 44.7% (2.62 - 4.13GHz, Fig. 46). One of the reasons of this bandwidth enhancement is multiple resonances provided by the stacked configuration. The second reason can be discussed by recalling the following expression for the Q-factor:

$$Q \propto 2w_0\varepsilon_r^p\left(\frac{Volume_{DRA}}{Surface_{Dra}}\right)^s \qquad p > s \geq 1$$

Neglecting any volume change between two designs (assuming no significant change over volume), the surface area is increased remarkably in stacked DRA. An increase in the surface area directly decreases the Q-factor, thus, the overall bandwidth was increased since the impedance bandwidth is inversely proportional to Q-factor.

The gain of the antenna is 9.35dB whereas the gain of the single CDRA was 4.81dB. The 3dB beamwidths of the antenna are 62° and 50° at H-plane and E-plane, respectively. It can be observed that the increase in the gain is due to the three fold

decrease in the E-plane 3dB bemawidth. The stacked designs result in more fringing fields at the sides of DRA. Moreover the radiating aperture of a SCDRA is larger compared to the CDRA. Thus, higher gains with narrower beamwidths can be achieved with stacked configuration.

The co-polar and cross polar components of E-field in both $\emptyset = 0$ and $\emptyset = 90°$ planes are plotted in Fig. 47 and Fig. 48, respectively. The cross-polarized field level is 58dB below the co-polarized field in broadside direction at each plane. Even within 3dB beamwidth, cross-polarization level is 26dB below the co-polarized level. Front-to-back ratio is 19dB.

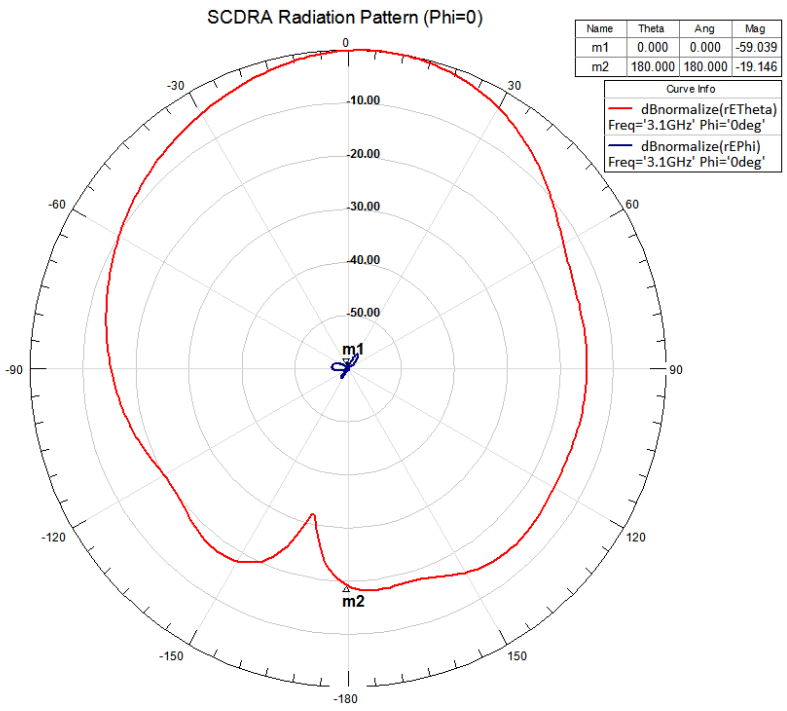

Fig. 47 Co-pol and Cross-pols components of E-field at E-plane

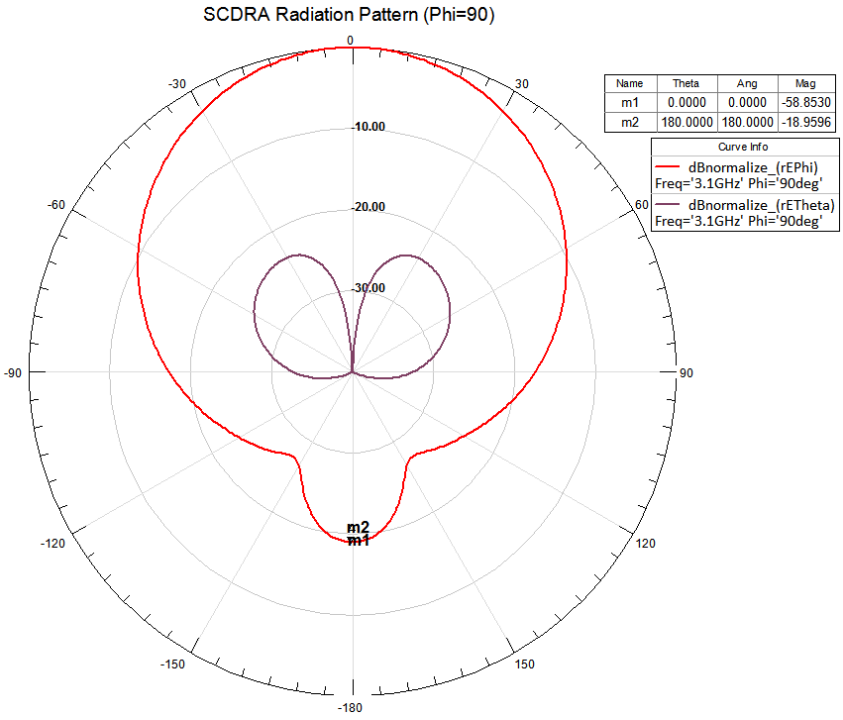

Fig. 48 Co-pol and Cross-pol components of E-field at H-plane

The diameter of the element is $0.62\lambda_0$ which is suitable for array applications. However the radiating elements would be located closer to each other when compared to that of a CDRA array, hence, the mutual coupling must be investigated during designs.

CHAPTER 5

ARRAY DESIGN

In this section, the design of array feed network will be presented. The dielectric resonator antennas that are designed in the previous chapter will be used as array elements.

The requirements for the array as follows:

- Beamwidth ≅ 10° at broadside
- Sidelobe level ≤ $-30dB$

It is well-known that amplitude tapering needs to be performed to array excitation coefficients in order to reduce sidelobe levels. Binomial, Dolph-Chebychev, Taylor and cosine-squared are widely used amplitude tapering distributions. Taylor distribution will be used in the design of the array considered in this thesis. After determining the type of distribution the number of elements (N) and the spacing between elements (d) need to be specified. The 3dB beamwidth (θ_{HPBW}) of a uniformly illuminated aperture with length L can be computed by using the following approximate relation:

$$\theta_{\mathrm{HPBW}} = \frac{50.6}{L/\lambda_0}\ in\ degrees$$

This relation is used to determine number of elements by assigning $L = Nd$. For 10°

beamwidth $L = Nd = 5\lambda_0$. When the number of array elements is equal to powers of two, design of feed network becomes easier through the use of two way power dividers. The spacing between array elements should be greater than the size of an element which is $0.62\lambda_0$ for SCDRA. Moreover it should be smaller than the wavelength to avoid grating lobes. Considering these constraints on N and d, N is chosen to be 8.

It is well-known that beamwidth increases by applying amplitude tapering. In [25] the beamwidth broadening factor (BBF) for a cosine squared on pedestal distribution is reported to be 1.295 for $30dB$ SLL. By making use of this BBF d can be computed from the following relation:

$$\theta_{HPBW} = \frac{50.6\ x\ 1.295}{L/\lambda_0} = \frac{65.527}{8d/\lambda_0}$$

For 10° beamwidth the inter-element spacing of 8 element array is computed to be $d = 0.819\lambda_0 = 7.92cm$. d is chosen to be $8cm$. The excitation of array element is computed by using the following one parameter Taylor distribution [26]

$$\mathrm{w}(m) = I_0(\alpha\sqrt{1 - m^2/M^2}), \tag{28}$$

$m = 0, \pm 1, \ldots, \pm M$ for odd number of array elements $N = 2M + 1$

$m = \pm 1, \pm 2, \ldots, \pm M$ for even number of array elements $N = 2M$

And $I_0(x)$ is the modified Bessel function of first kind and zeroth order.

An empirical formula for α have been developed by Kaiser and Schafer in terms of the SLL in dB (R),

$$\alpha = \begin{cases} 0, & R < 13.26 \\ 0.76609(R - 13.26)^{0.4} + 0.09834(R - 13.26), & 13.26 \leq R < 60 \\ 0.1238(R + 6.3), & 60 < R < 120 \end{cases} \quad (29)$$

Computed coefficients are:

$$w(1) = w(-1) = 1$$

$$w(2) = w(-2) = 0.8172$$

$$w(3) = w(-3) = 0.5278$$

$$w(4) = w(-4) = 0.2863$$

Since the excitation coefficients are symmetric with respect to the center of the array a 4-way power divider is sufficient for the design of the feed network. According to the required excitation coefficients when the transmission coefficients (S_{ij}) between the input port (port 1) and each output port (port 2-5) are calculated as follows by considering port 5 as reference.

$$S_{41} - S_{51} = -1.75 \text{ dB}$$

$$S_{31} - S_{51} = -5.55 \text{ dB}$$

$$S_{21} - S_{51} = -10{,}86 \text{ dB}$$

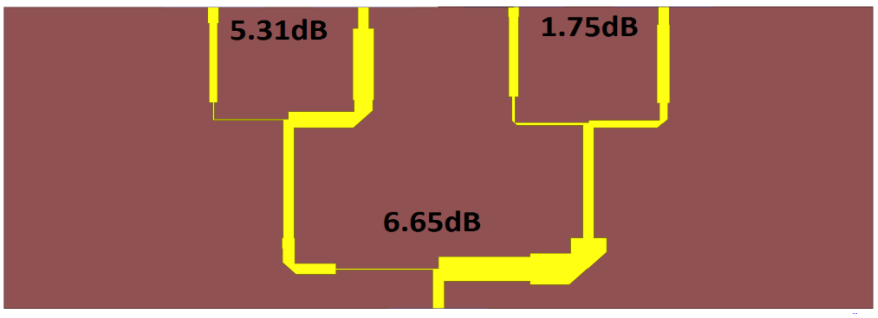

Fig. 49 Conventional power divider network

First a power divider with a corporate divided configuration as shown in Fig. 49 is designed. The numbers on the figure denote the difference in the transmission coefficients of two adjacent ports. These numbers will be referred as “power division ratio” for the corresponding two way power dividers in the rest of this thesis. The widths of the transmission lines are designed (details will be presented in next section) to provide the impedance transformations required for unequal power division between the output ports. It can be observed from the Fig. 49 that this configuration requires very large power division ratios that result in impractical designs due to manufacturing tolerances in the widths of the transmission lines.

Hence, a different power divider configuration is proposed as shown in Fig. 50 to get rid of one of the large power ratios. With new divider topology, power division ratio of the first divider is lowered to 0.12dB from 6.65dB.

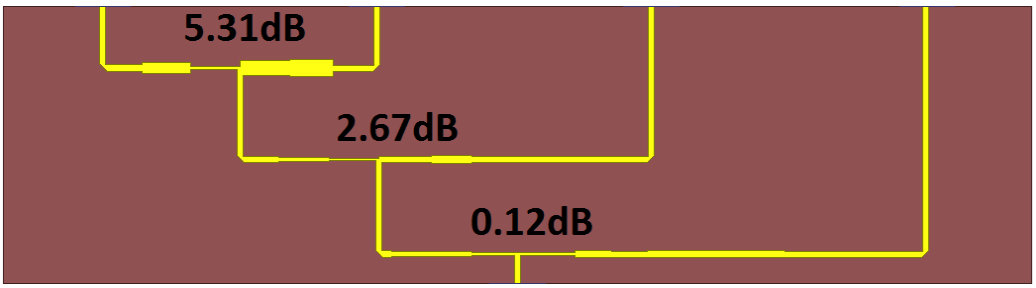

Fig. 50 Power divider configuration

In the following section, the design procedure for the power divider shown in Fig. 50 will be presented.

5.1 Design of Power Divider

The first unequal-split Wilkinson article is published by Parad and Moynihan in Jan. 1965, entitled *Split Tee Power Divider* [27]. In the article, Parad and Moynihan develop a set of equations for two-way unequal dividers shown in Fig. 51.

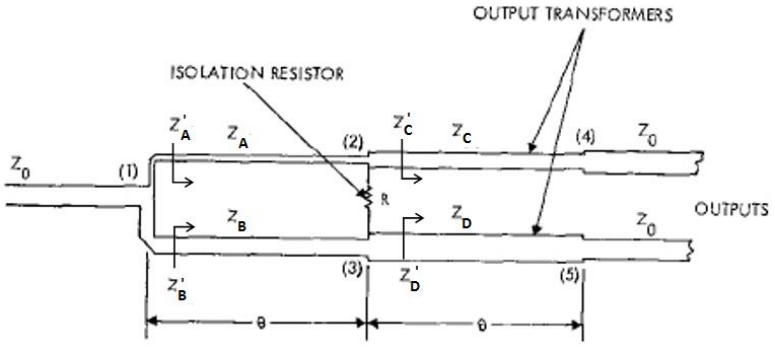

Fig. 51 Unequal Wilkinson divider by Parad and Moynihan [27]

Z_A, Z_B, Z_C, Z_D are characteristic impedances of two stage quarter wave impedance transformer sections. Z_A', Z_B' are the impedances seen from the input of corresponding arms.

Due to the parallel connection the power ratio is inversely proportional to the ratio of the impedances seen from the ports.

$$\frac{P_3}{P_2} = \frac{Z_A'}{Z_B'} \tag{30}$$

Also the impedances of two arms must satisfy the equation below at the center frequency for matching purposes,

$$Z_0 = \frac{Z_A' Z_B'}{Z_A' + Z_B'} \tag{31}$$

Using above equations (30) (31),

$$Z_A' = Z_0(1 + P_3/P_2) \tag{32}$$

$$Z_B' = Z_0(1 + P_3/P_2)\ /(P_3/P_2) \tag{33}$$

Considering the cascaded quarter wave transformers $Z_A^{'}$ and$Z_B^{'}$ can be written as:

$$Z_A^{'} = \frac{Z_0 Z_A^2}{Z_C^2} \quad , \quad Z_B^{'} = \frac{Z_0 Z_B^2}{Z_D^2} \tag{34}$$

Using (32) and (34),

$$Z_C = \frac{Z_A}{\sqrt{1+\frac{P_3}{P_2}}}\ Z_D = Z_B\sqrt{\frac{P_3}{P_2}/(1+\frac{P_3}{P_2})} \tag{35}$$

Also in order to have zero voltage across the isolation resistor, the following impedance ratio must also be satisfied:

$$\frac{Z_A}{Z_B} = \frac{P_3}{P_2} \tag{36}$$

Now all the impedances can be written in terms of Z_A, also the isolation resistance can be derived using the odd mode analysis however, for our case the isolation resistance will not be used.

$$Z_B = \frac{Z_A}{P_3/P_2}\ , \quad Z_C = \frac{Z_A}{\sqrt{1+P_3/P_2}}, \quad Z_D = \frac{Z_A}{\sqrt{P_3/P_2}\sqrt{1+P_3/P_2}} \tag{37}$$

For a high dividing ratio, the divider design may end up with an unrealizable (very high) characteristic impedance. In such situations, the arm with the highest impedance can be fixed to a more realizable impedance value and so the other impedances can be calculated accordingly. The design of three different power

dividers (shown in Fig. 52) will be presented in the following subsections.

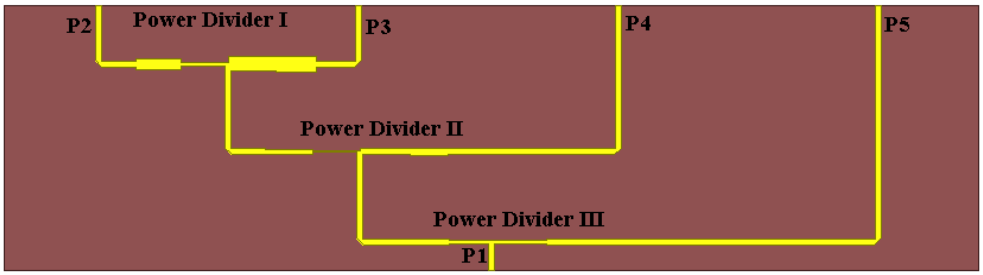

Fig. 52 Power divider I, II and III

5.1.1 Power Divider I

The voltage coefficients of the last two elements determines the power division ratio of this divider as:

$$w(3) = w(-3) = 0.5278 = -5.55dB$$

$$w(4) = w(-4) = 0.2863 = -10.86dB$$

$$w(3)dB - w(4)dB = 5.31dB$$

The divider must provide 5.31dB of a difference between its two arms.
For a non-Wilkinson divider,

$$\frac{P_A}{P_B} = \frac{Z_B}{Z_A} = 0.2942\ (5.31dB)$$

Also

$$Z_A \ /\!/\ Z_B = \frac{Z_A Z_B}{Z_A + Z_B} = 50\Omega$$

Using those two equations the arm impedances are calculated as:

$$Z_A = 219.93\Omega$$

$$Z_B = 64.712\Omega$$

For a 0.813mm RG4003C PCB substrate, 219.93Ω corresponds to a very narrow line segment of width of $44.93\mu m$ which is not producible, furthermore it is generally troublesome to maintain a good return loss characteristics for a line pair with high dimensional difference.

Unequal Wilkinson divider with two transformer sections is utilized to maintain 5.31dB of divider ratio with an applicable line width.

The thinnest arm is chosen to be 1mm. Therefore corresponding characteristic impedance for 1mm line segment is 68.8587 Ω (Z_A).

Using (37) Z_B, Z_C, Z_D are calculated as;

$$Z_B = \frac{Z_A}{P_3/P_2} = \frac{68.8587}{3.39856} = 20.261\ \Omega$$

$$Z_C = \frac{Z_A}{\sqrt{1 + P_3/P_2}} = \frac{68.8587}{2.0972} = 32.832\ \Omega$$

$$Z_D = \frac{Z_A}{\sqrt{P_3/P_2}\sqrt{1 + P_3/P_2}} = 17.81\ \Omega$$

The width and quarter wave length of the transmission lines are obtained by using transmission line calculator toolbox (LineCalc) of a microwave circuit simulator (Agilent ADS).

$w_{Z_B} = 6.26\ mm, \qquad l_{Z_B} = 13.72\ mm$

$w_{Z_C} = 3.34\ mm, \qquad l_{Z_C} = 14.11\ mm$

$w_{Z_D} = 7.33\ mm, \qquad l_{Z_D} = 13.629\ mm$

The divider network is simulated on both ADS and HFSS. The simulation results of

these two platforms are different than each other. Since HFSS is a full-wave solver, the results are more reliable. On the other hand it is more convenient to investigate the effect of line segment dimensions on divider performance using ADS. Thus, the divider is tuned on ADS and analyzed on HFSS. Resulting dimensions are:

$w_{Z_B} = 4.45\ mm, \qquad l_{Z_B} = 14.61\ mm$

$w_{Z_D} = 4.9\ mm, \qquad l_{Z_D} = 12.7\ mm$

Divider I with scaled dimensions can be seen in Fig. 53.

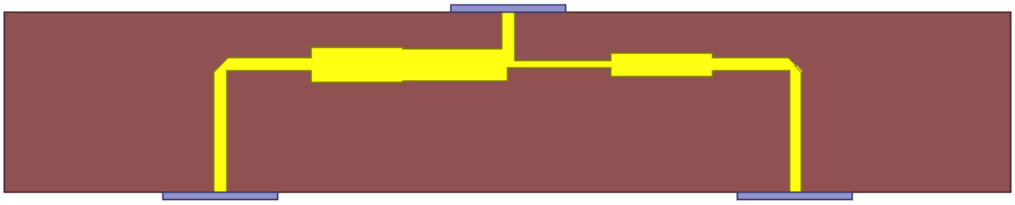

Fig. 53 Scaled layout of power divider I

ADS and HFSS results for input return loss and power division ratio are shown in Fig. 54 and Fig. 55.

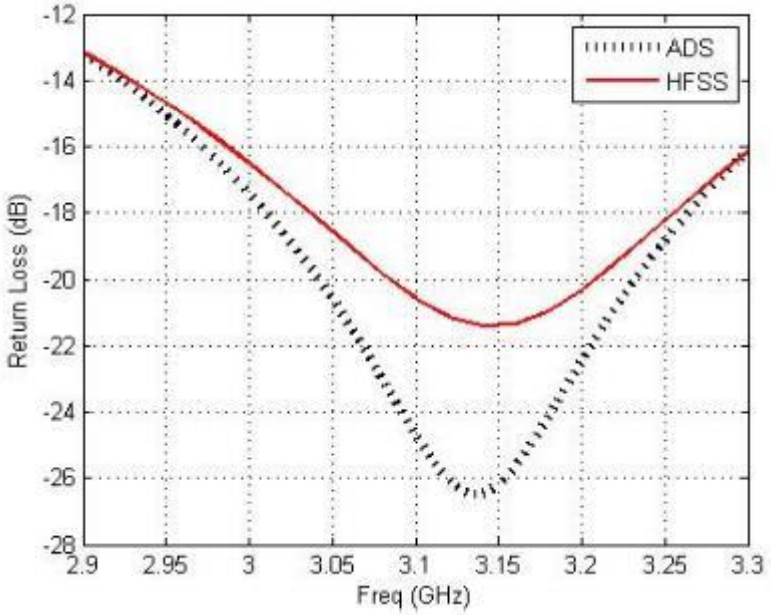

Fig. 54 Return loss of power divider I

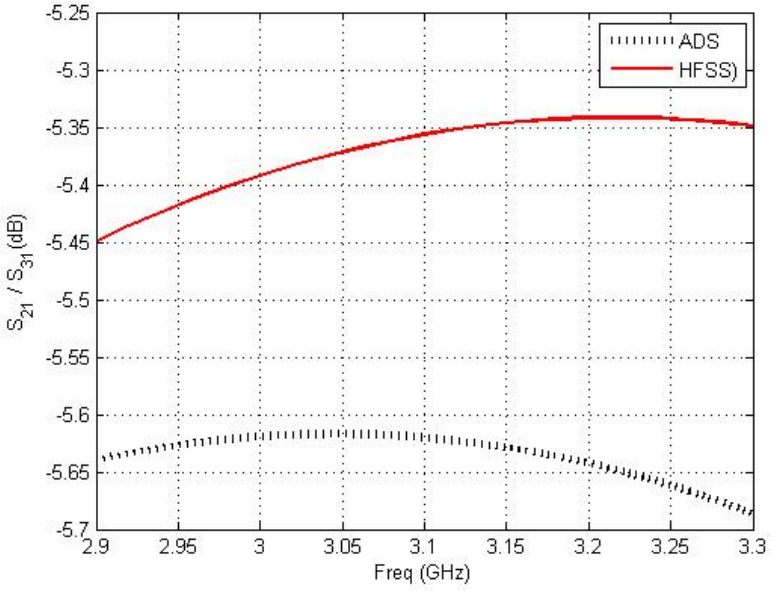

Fig. 55 Power division ratio of power divider I

5.1.2 Power Divider II

The same procedure is followed in designing Power Divider II which as a power division ratio of 2.67dB. The dimensions are:

$w_{Z_A} = 0.43\ mm, \quad l_{Z_A} = 13.4\ mm$

$w_{Z_B} = 1.6\ mm, \quad l_{Z_B} = 14.6\ mm$

$w_{Z_C} = 1.4\ mm, \quad l_{Z_C} = 14.7\ mm$

$w_{Z_D} = 2.27\ mm, \quad l_{Z_D} = 11.85\ mm$

The scaled layout of power divider II can be seen in Fig. 56.

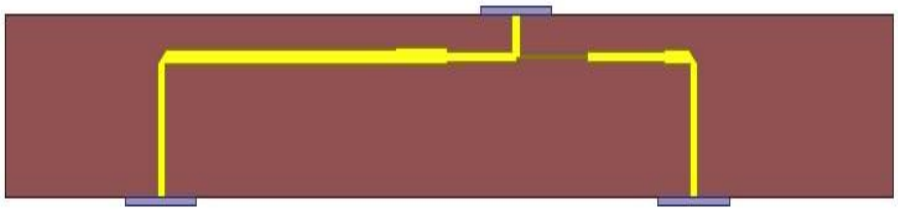

Fig. 56 Scaled layout of power divider II

ADS and HFSS results for input return loss and power division ratio are shown in Fig. 57 and Fig. 58:

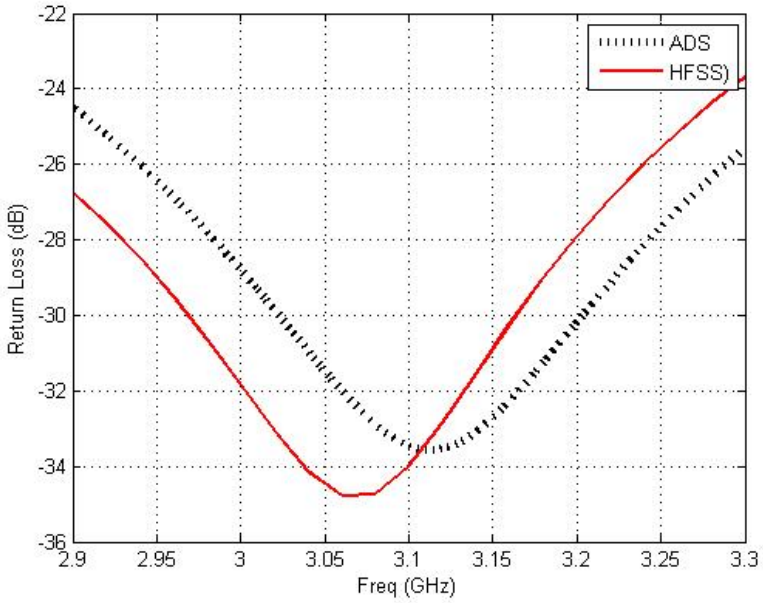

Fig. 57 Return loss of power divider II

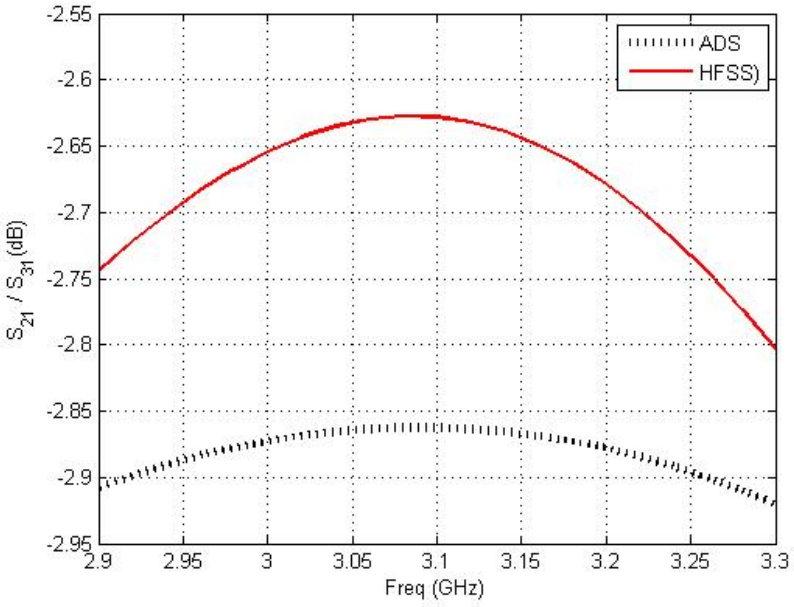

Fig. 58 Power division ratio of power divider II

5.1.3 Power Divider III

A divider, which only differs 0.12dB from a two way equal divider, is required.

The dimensions are:

$w_{Z_A} = 1\ mm, \qquad l_{Z_A} = 12.25\ mm$

$w_{Z_B} = 0.9\ mm, \qquad l_{Z_B} = 16\ mm$

$w_{Z_C} = 1.7\ mm, \qquad l_{Z_C} = 23.5\ mm$

$w_{Z_D} = 1.76\ mm, \qquad l_{Z_D} = 21\ mm$

The scaled layout of power divider III can be seen in Fig. 59.

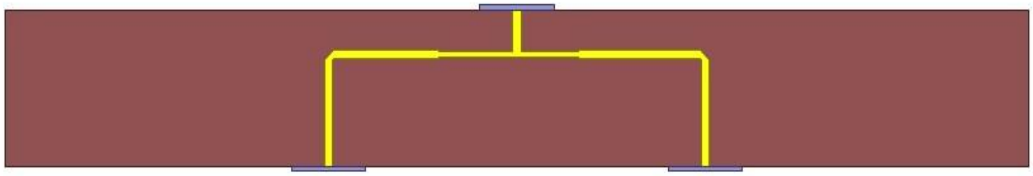

Fig. 59 Scaled layout of power divider III

ADS and HFSS results for input return loss and power division ratio are shown in Fig. 60 and Fig. 61.

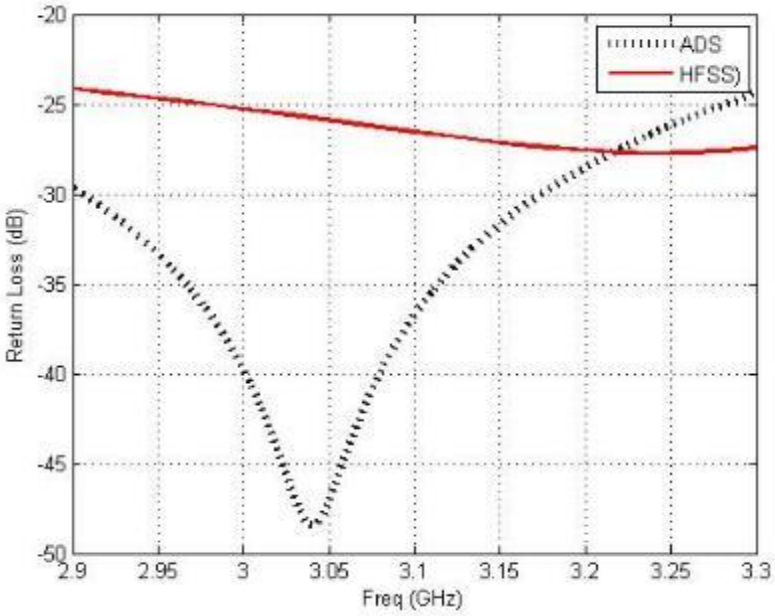

Fig. 60 Return loss of power divider III

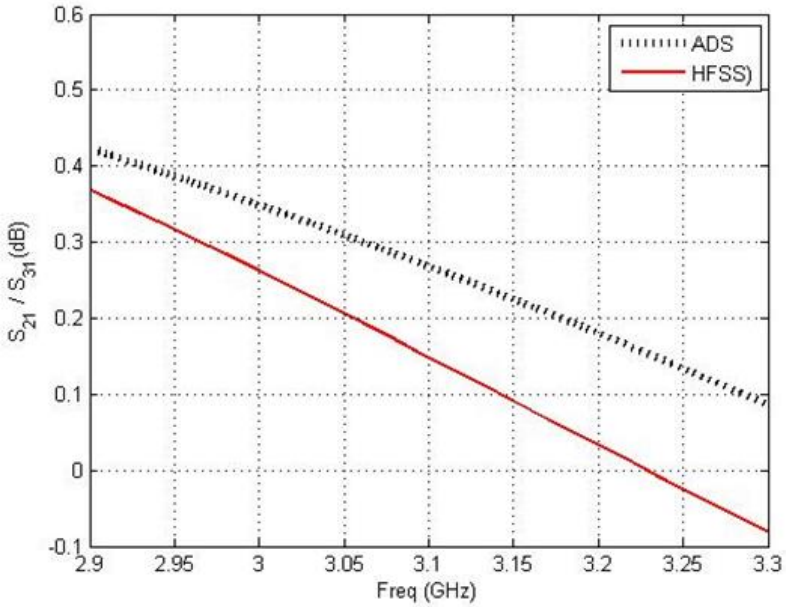

Fig. 61 Power division ratio of power divider III

5.2 8-Element RDRA Array

The array elements and the beam forming network were discussed in previous sections. The 8-element RDRA array together with the feed network is simulated on HFSS. The element spacing is 8mm, making the total array size 57.35cm. Together with the ground plane, total array-antenna size reaches 66cm. Since the dimension of RDRA along the array axis is small (1.15cm), the edge-to-edge distance between the successive elements is 6.85cm ($0.707\lambda_0$). This distance would be more important in terms of mutual coupling if the antennas were endfire radiating. The HFSS model is demonstrated in Fig. 62 and Fig. 63. The simulation results will be discussed together with the results of manufactured divider in Chapter 7.

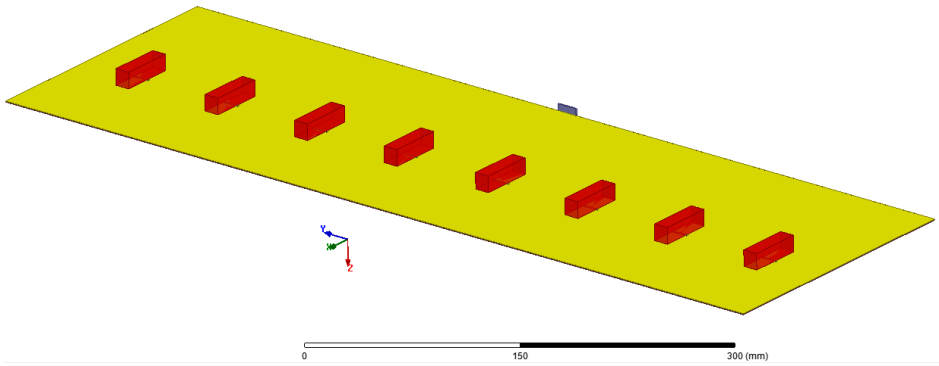

Fig. 62 8-Element RDRA, radiating side

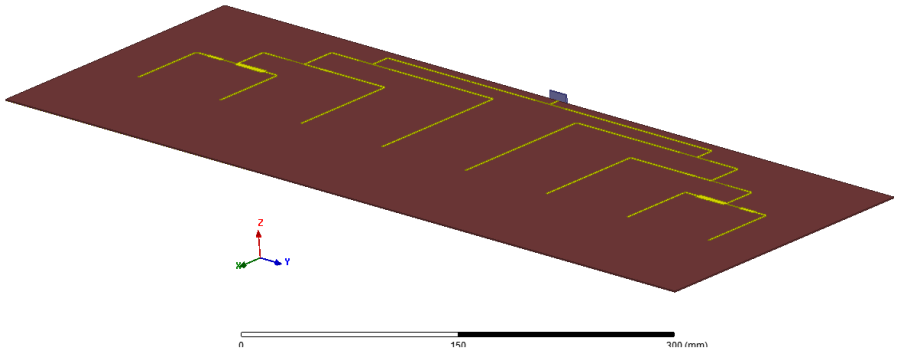

Fig. 63 8-Element RDRA, beam former network

The simulation results for input return loss and radiation pattern in two principle planes are given in Fig. 64, Fig. 65 and Fig. 66, respectively.

The co-pol to cross-pol ratio is more than 40dB. Front to back ratio is 10dB. The gain of the antenna is 10.88dB with a 3dB beamwidth of 9.6° at H-plane and 133° at E-plane. The SLL levels are below $-26dB$ which is 4dB above the -30dB requirement. This is due to the mutual coupling between array elements. The power divider was designed by assuming that the antenna impedances were 50Ω. Although this assumption is reasonable for an isolated antenna, it may not be valid when the active input impedance of each element considered in the array environment. As the active input impedance departs from 50Ω the power division ratios also depart from the expected values.

It can be seen that apart from the SLL, the design requirements are satisfied according to simulation results.

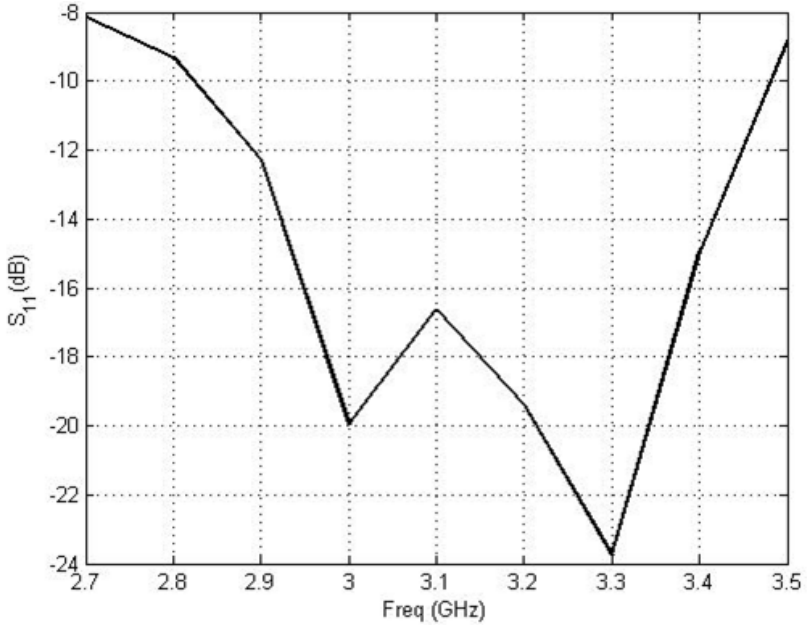

Fig. 64 Input return loss

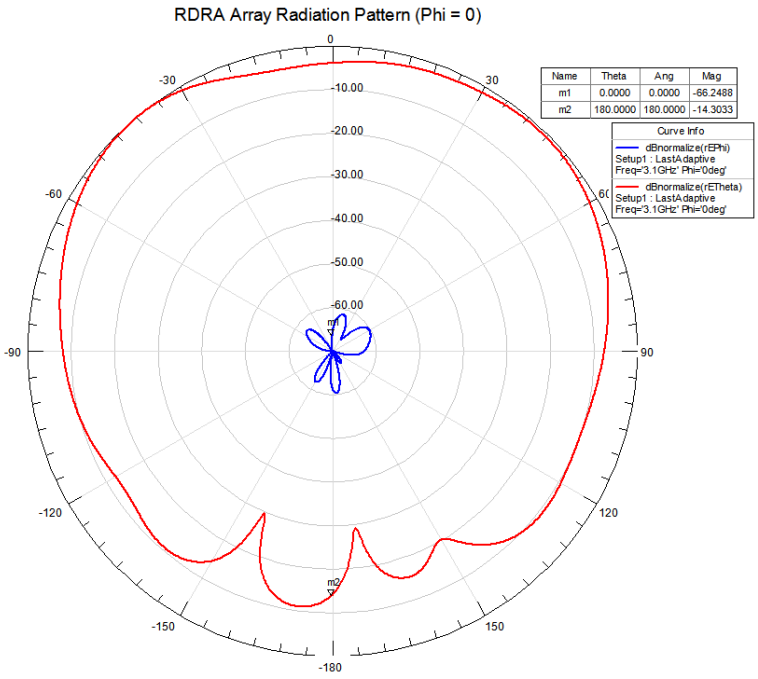

Fig. 65 Co-pol and Cross-pol components of E-field at E-plane

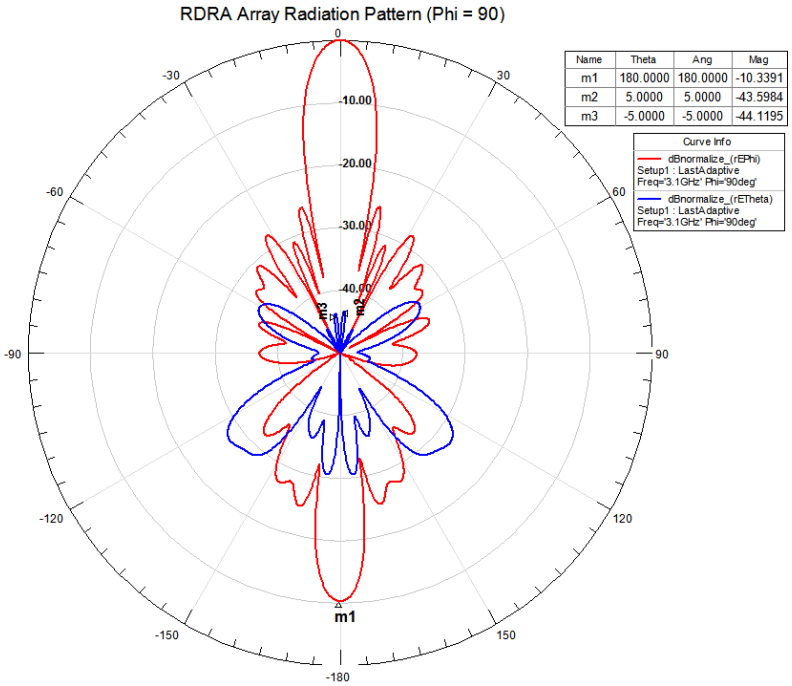

Fig. 66 Co-pol and Cross-pol components of E-field at H-plane

5.3 8-Element SCDRA Array

The array is composed of SCDRA elements instead of RDRA elements as it was in previous section. The array length is 62mm. Together with the ground plane, the length of the structure is 70mm. Unlike the RDRA array, the edge to edge distance between the successive elements is 2mm ($\sim 0.2\lambda_0$). The HFSS model is demonstrated in Fig. 67 and Fig. 68.

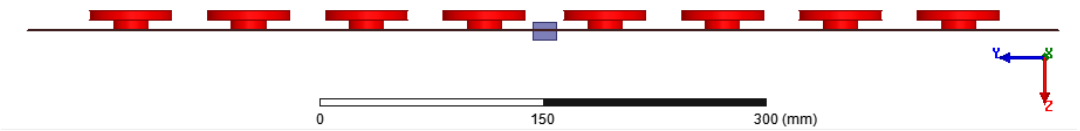

Fig. 67 8-Element SCDRA array, side view

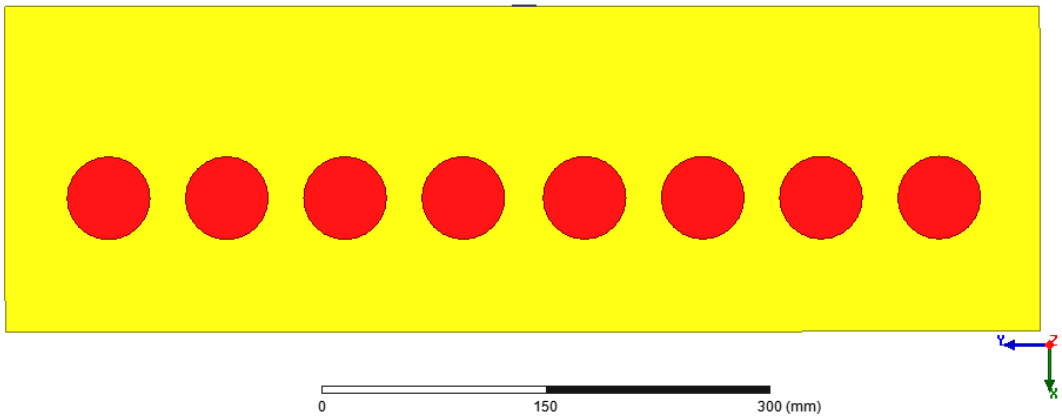

Fig. 68 8-Element SCDRA array, top view

The same beam former is utilized as in RDRA array. The co-pol component is more than 37dB above the cross-pol component in 3dB beamwidth. The gain of the antenna is 14.58dB with a 3dB beamwidth of 9.4° at H-plane and 91.6° at E-plane.

The gain difference (3.64dB) between the RDRA and the SCDRA element is conserved to be same as the gain difference between the array configurations (3.7dB). The SLL levels are below $-26.9dB$ which is 3.1dB above the -30dB requirement. Front to back ratio is 14.5dB, higher than the RDRA array case. The endmost element is 4.2 cm away from the ground edge.

The simulation results for input return loss and radiation pattern in two principle planes are given in Fig. 69, Fig. 70 and Fig. 71, respectively.

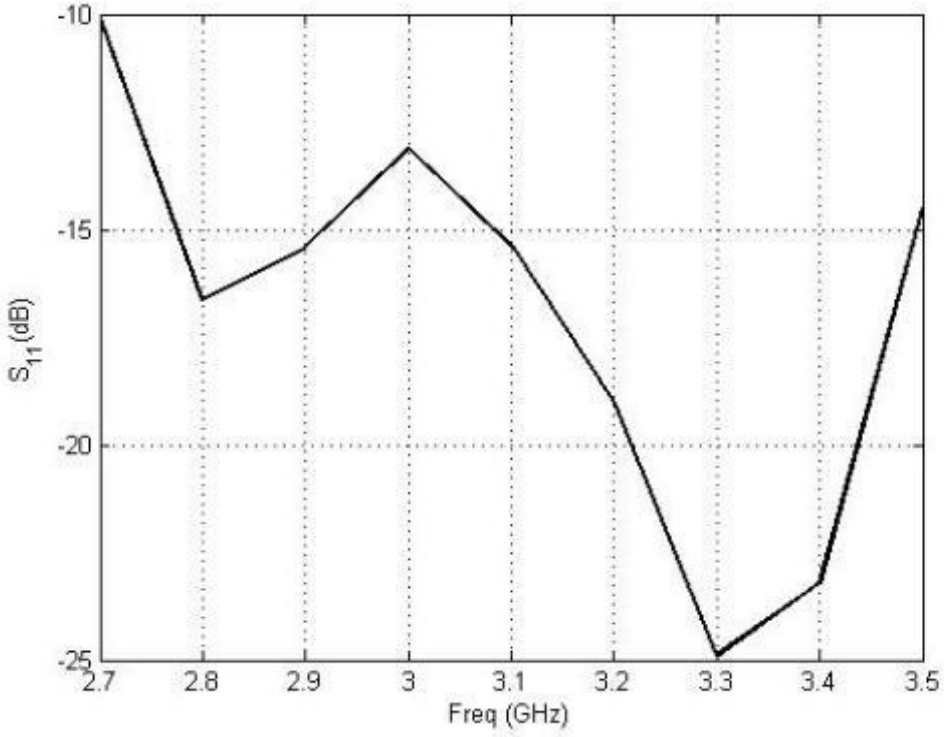

Fig. 69 Impedance bandwidth of SCDRA array

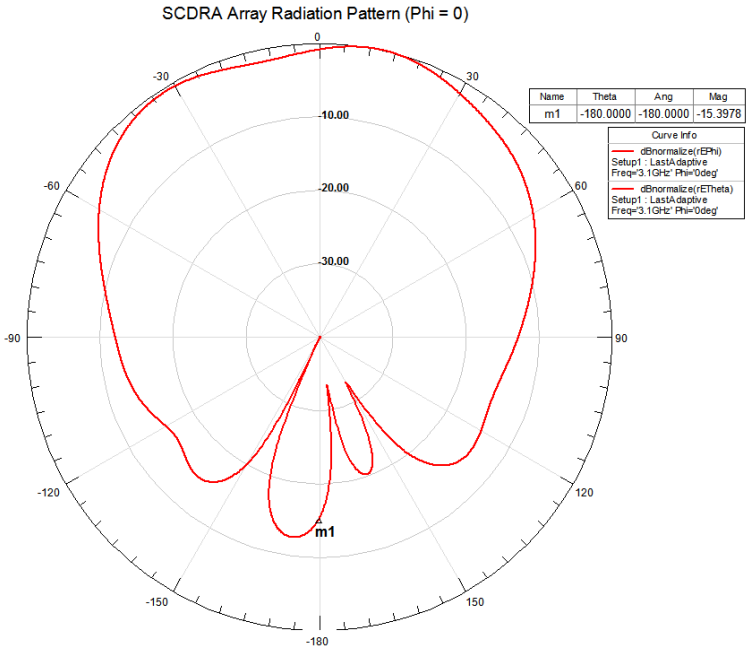

Fig. 70 Co-pol and Cross-pol components of E-field at E-plane

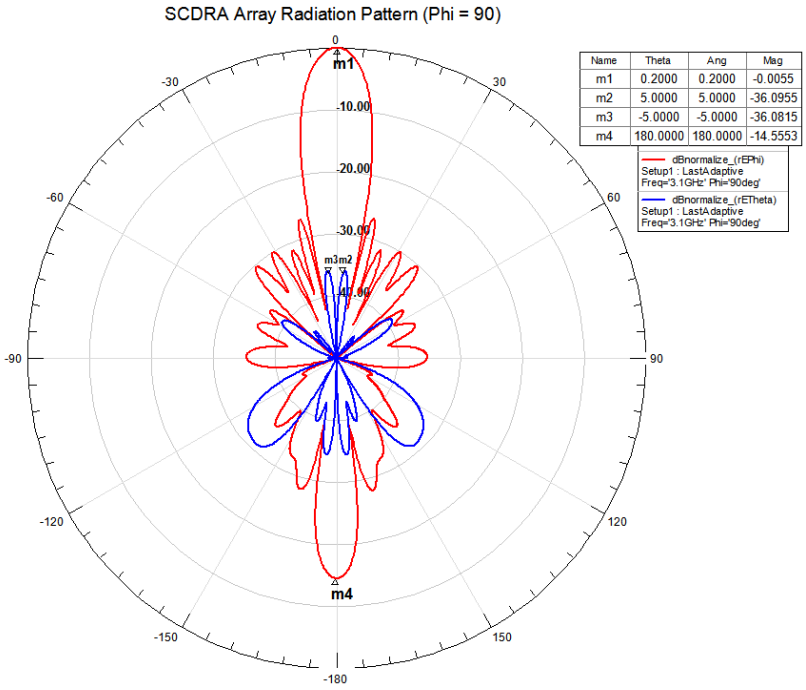

Fig. 71 Co-pol and Cross-pol components of E-field at H- plane

The gain, directivity, E-Plane and H-plane 3dB beamwidths and the front to back ratios (F/B) of both single elements and arrays are summarized in Table 1. While the directivity and gain values are close to each other for a single element, about 1 dB difference between them can be observed for the array configuration. Hence the loss of the feed network can be considered to be about 1 dB. Moreover the E-plane 3 dB beamwidths get wider for the array configuration. From the asymmetry in the E-plane radiation patterns, this widening might be attributed to the spurious radiation from the feed network.

Table 1 Gain, Directivity, E-Plane and H-Plane 3dB Beamwidths and the Front to Back Ratios (F/B) of both Single Elements and Arrays

	Gain (dB)	Directivity (dB)	E-Plane HPBW (degrees)	H-Plane HPBW (degrees)	F/B Ratio (dB)	Gain (dB)
RDRA	5.71	5.92	125	78	14.42	5.71
CDRA	4.81	5.24	145	69	13.43	4.81
SCDRA	9.35	9.38	50	62	18.95	9.35
Array RDRA	10.88	11.75	133	9.6	10.33	10.88
Array SCDRA	14.58	15.45	91.6	9.5	14.55	14.58

CHAPTER 6

FABRICATED PROTOTYPES AND MEASURED RESULTS

Prototypes for rectangular DRA and stacked cylindrical DRA are manufactured. The materials often used in DRA applications are ceramic based materials. In this thesis work, the DRAs are fabricated using Rogers TMM10i material which combines many of the desirable features of ceramic substrates. The antenna is constructed using a prototype PCB milling machine as seen in Fig. 72.

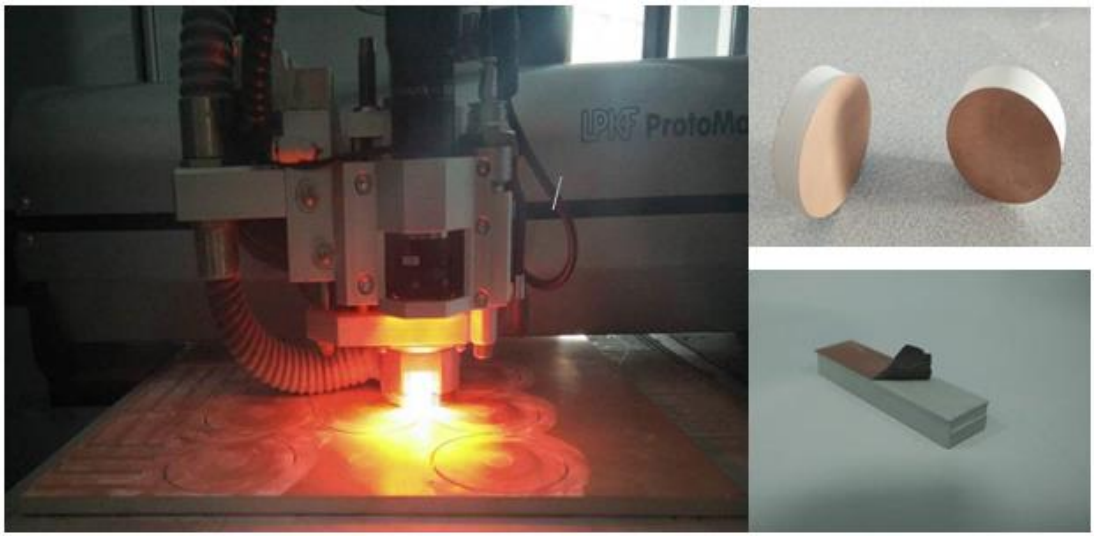

Fig. 72 DRA fabrication

The copper layer is peeled off from the DRAs easily.

The structure is constructed on the ground side of a RG 4003C substrate with a relative permittivity of 3.55. The ground plane and the substrate dimensions are slightly larger compared to the simulations.

The impedance characteristics of prototypes are tested using an Agilent N5242A PNA-X network analyzer. The results are shown in Fig. 73. The input impedance characteristics of experimental antenna are in good agreement with the HFSS simulations. The operational bandwidth is slightly shifted towards lower band by 125MHz, however the matching pattern is pretty consistent with the simulations. The shift is most probably due to the adhesive material used to fasten the DRAs on to the ground plane.

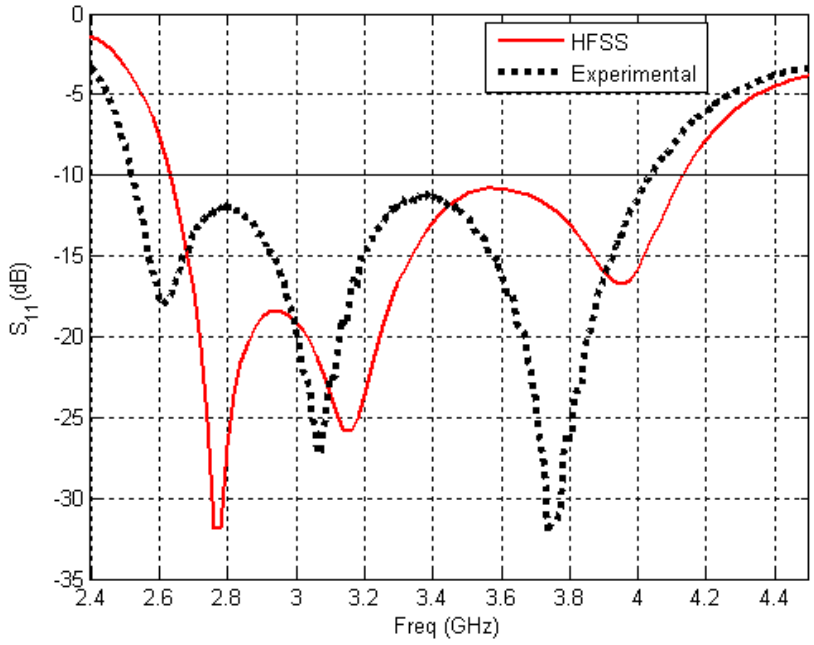

Fig. 73 CDRA element return loss curve

The radiation pattern of a SCDRA element is measured using SATIMO SG32 spherical near field test station. The platform can measure radiation patterns in a band from 2GHz up to 18GHz.

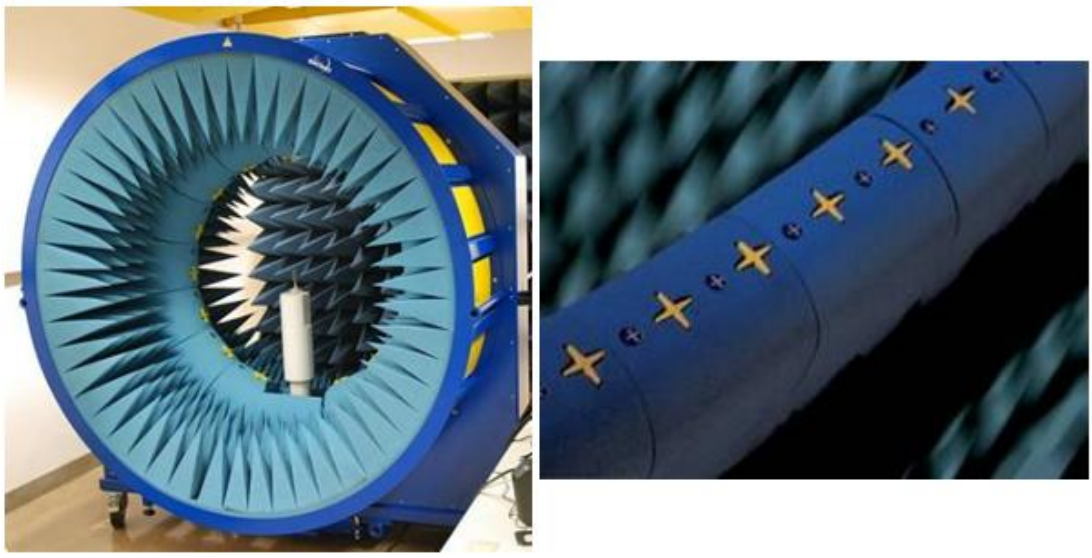

Fig. 74 SATIMO SG32 antenna measurement station

In the test setup, the emitting antenna element is placed on a mast which is at the center of the station as seen in Fig. 74 and

Fig. 75a. Calibrated probes (yellow and dark blue ones) are placed radially at fixed positions. The mast turns around its axis as the probes scan the elevation pattern. The measured and simulated pattern at H-plane is presented in Fig. 76. It can be observed that although the simulation and the measurement results are in good agreement for broadside direction, some discrepancies are observed for the lower half plane. These may be attributed to the large ground plane used in measurements. Since different designs are aimed to be measured on the same board as shown in Fig. 75, a quite large PCB is manufactured.

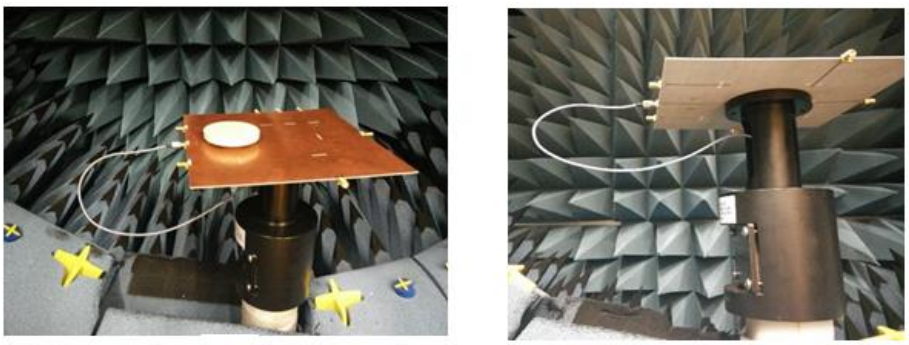

Fig. 75 a b

Fig. 75 Single DRA element measurement in SATIMO SG32

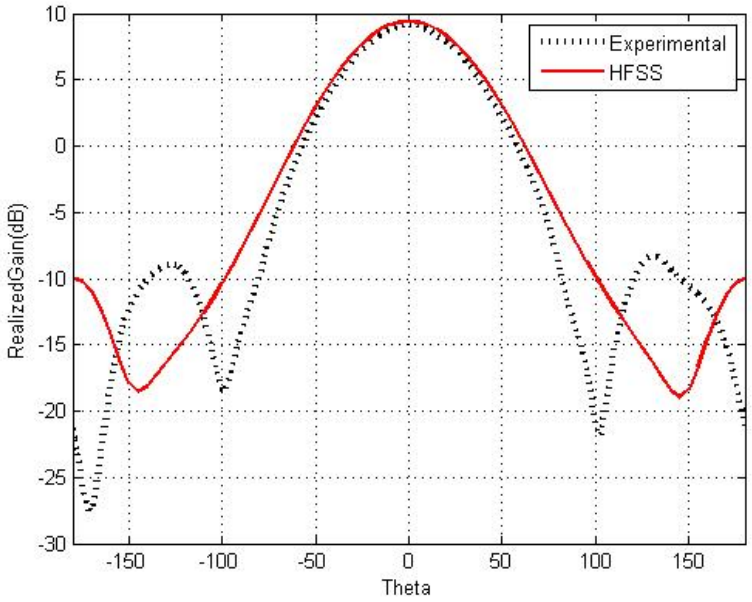

Fig. 76 CDRA element radiation pattern at H-plane

The RDRA element is also measured using the same test platforms. The return loss and the radiation patterns are shown in Fig. 77 and Fig. 78, respectively. For rectangular DRA, the operational bandwidth shifted 100MHz towards lower

frequencies. A similar discrepancy in the lower half plane radiation pattern is also observed for RDRA.

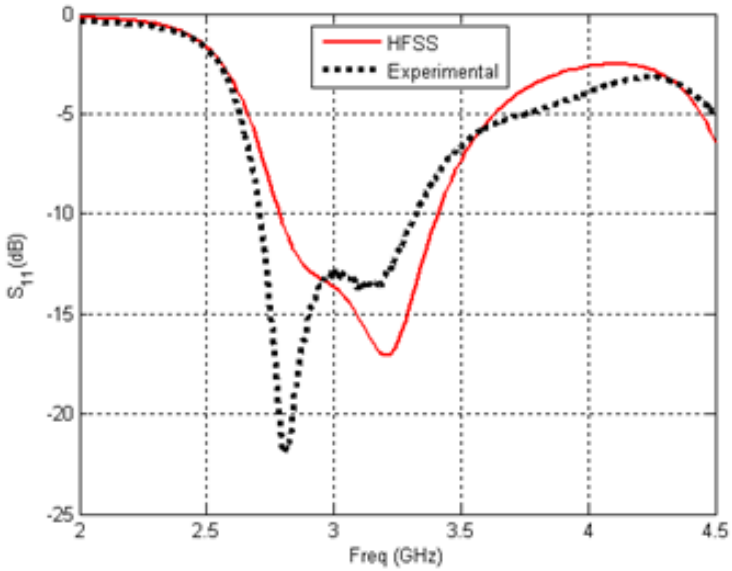

Fig. 77 RDRA element return loss curve

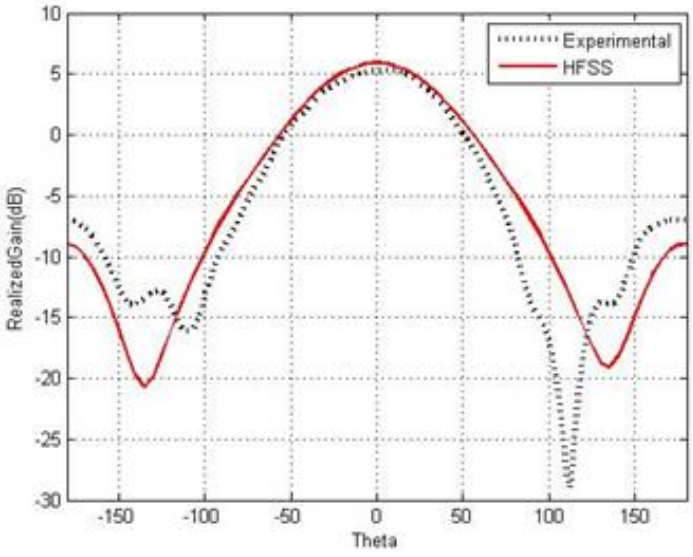

Fig. 78 RDRA element radiation pattern at H-plane

Half of the power divider is fabricated with connectors attached to each port as shown in Fig. 79 for the characterization of the power divider. The s-parameters of the divider are measured using Agilent N5242A PNA-X. The results are well-matched to the simulations and shown in Fig. 80.

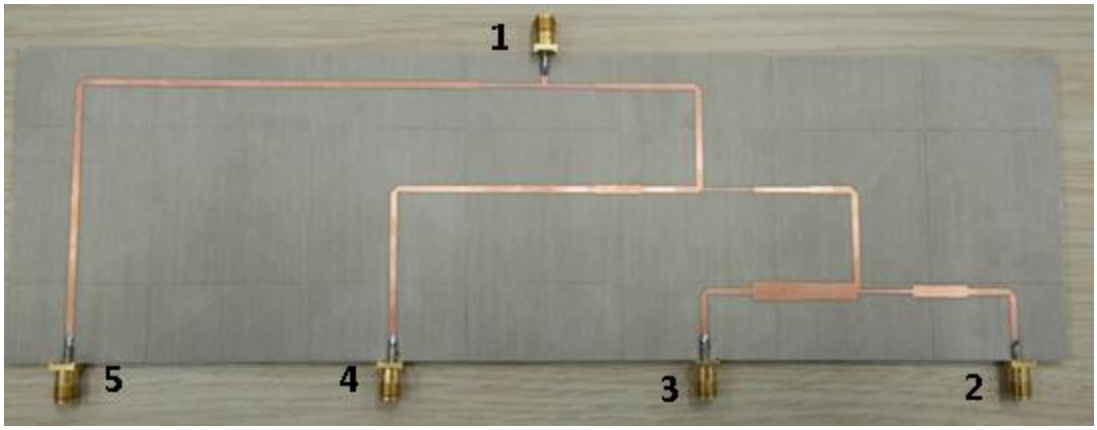

Fig. 79 Half a beam former

The input return loss results are shown in Fig. 80. The power division ratio measurement results are presented and compared to HFSS results in Fig. 81 through Fig. 83.

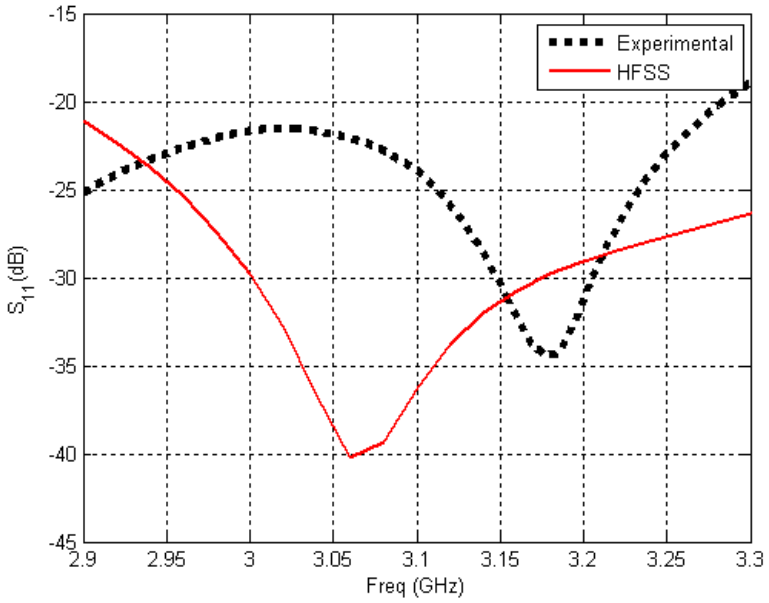

Fig. 80 Return loss of beam former network

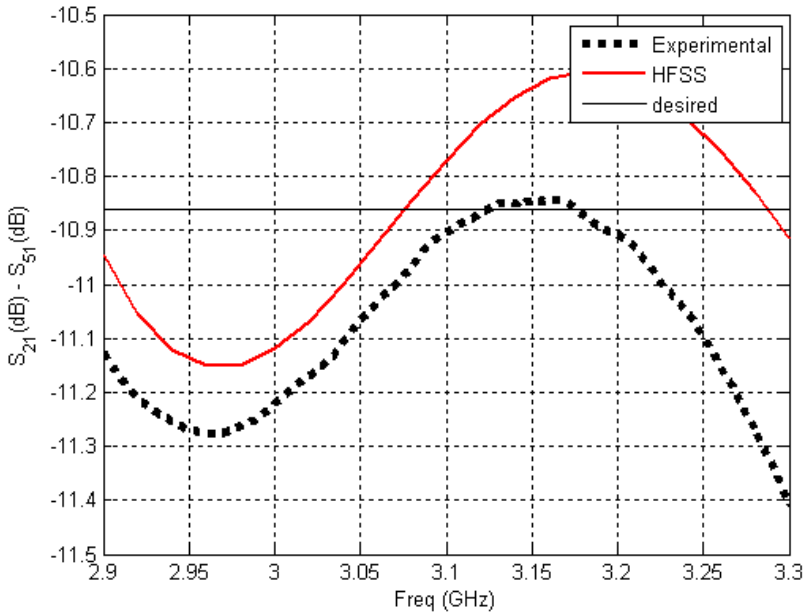

Fig. 81 The difference between Port2 and Port5

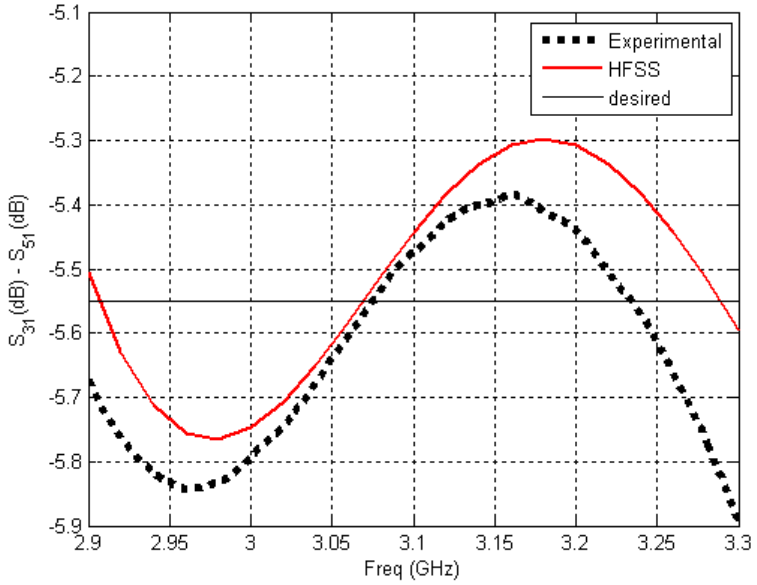

Fig. 82 The difference between Port3 and Port5

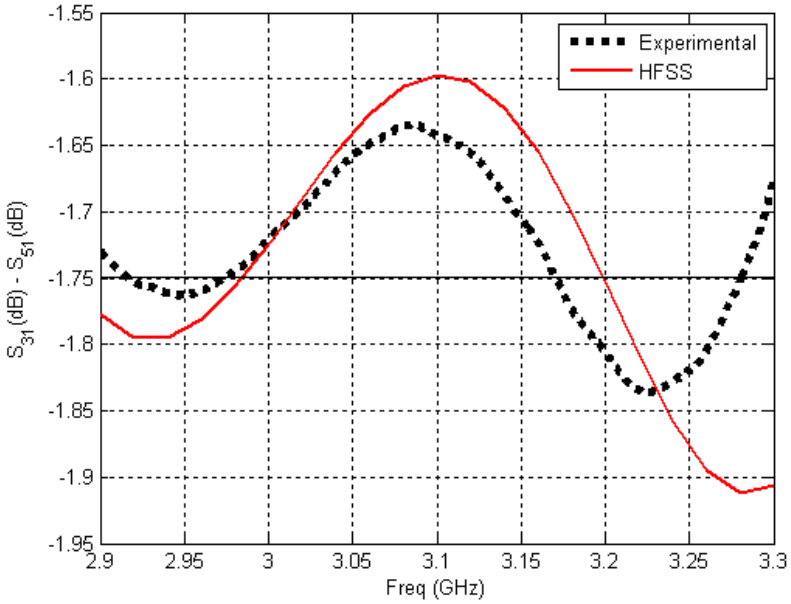

Fig. 83 The difference between Port4 and Port5

The difference between the simulation and the experiments is 0.06dB on the average. The extra insertion loss is caused by the port SMA connectors. Each measurement contains 2 connectors, with each of 0.03-to-0.05dB insertion loss.

The beam former printed board is fabricated in three pieces due to the excessive size for the prototype PCB drilling machine. The three pieces then combined with copper slabs soldered at the joints. Slabs are laser-cut to be as the same width as 50ohm line (1.78mm) in order not to introduce any further mismatch.

For the array antenna measurements, a support structure is manufactured as shown in Fig. 84. Delrin material is preferred to reduce any reflections caused by the support. The beam former PCB and the SMA connector is screw mounted to the support block.

Fig. 84 Array support structure

Return loss characteristics for SCDRA array are shown in Fig. 85. -10dB impedance bandwidth of the SCDRA array is around 44%. In the desired operation band of 2.9-3.3GHz, the array provides an impedance matching better than -15dB.

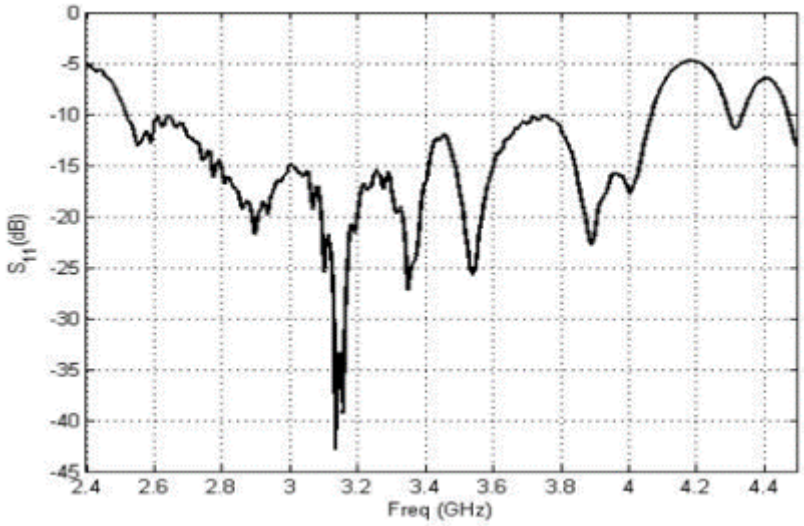

Fig. 85 Experimental return loss curve for 8-Element SCDRA array

The radiation pattern is measured in a different near field test station. The array measurements on SATIMO was not consistent since the dimension of the arrays exceeds the largest antenna size suitable for SATIMO measurement system. In antenna pattern, serious ripples are observed in 3dB bandwidth when measured using SATIMO. For antenna structures with high radiating apertures, the SATIMO introduces disturbance at the side lobes, resulting in much higher side lobe levels.

The radiation patterns measured in appropriate near field measurement platform are shown in Fig. 86.

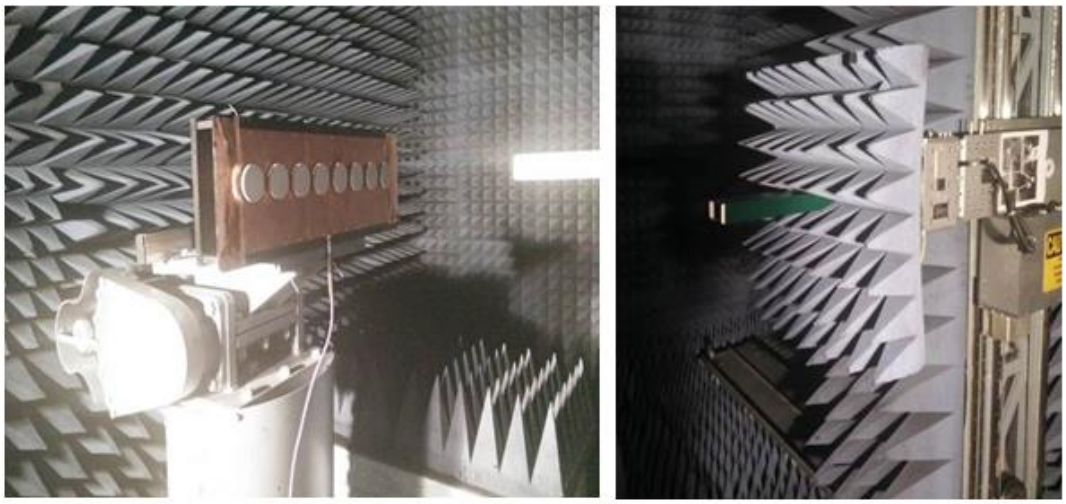

Fig. 86 Near field antenna measurement room

The antenna array is 40 cm away from measurement probe. Alignment procedure is completed by means of an antenna rotator. The measured and simulated radiation pattern of the array is plotted in Fig. 87.

The 3dB beamwidth is observed as 9.55 degrees which is 0.05 degree more than simulation results. Array have a gain of 14.3dB. The antenna gain is 0.2dB less than the simulation results. Since HPBW results for measurement and simulations are consistent, the difference in gain can be attributed to the losses in the feeding network. The design requirement of 30dB SLL could not be achieved both in experimental and simulation results. 26.9dB of first SLL is achieved in simulations and experiments.

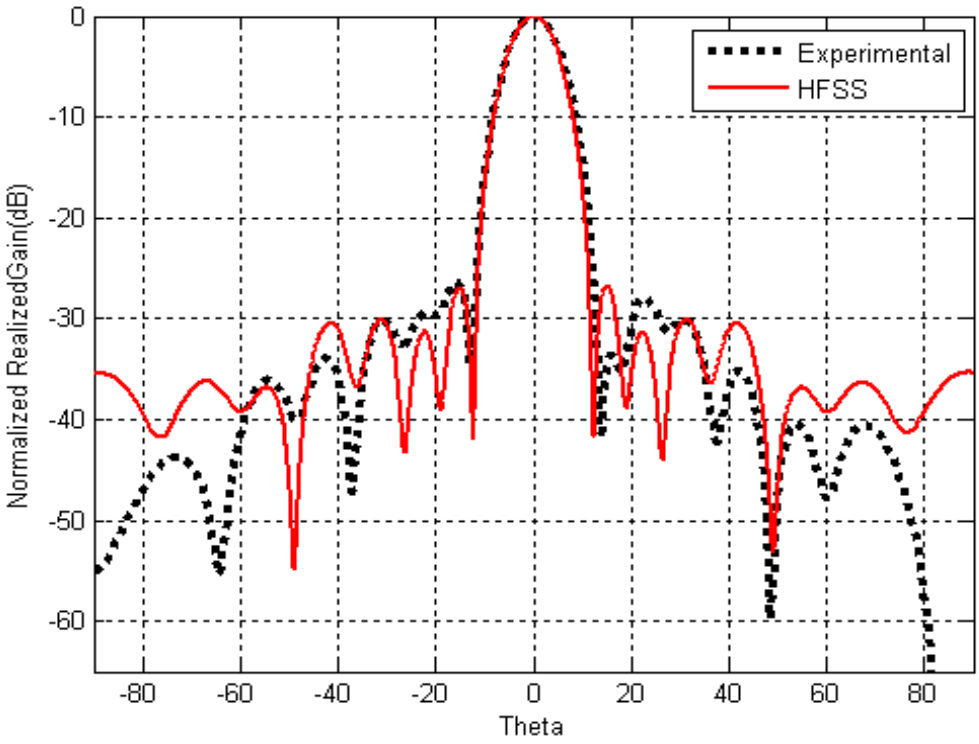

Fig. 87 Radiation pattern of 8-Element SCDRA array

The RDRA array is constructed on the same structure. The impedance bandwidth is measured and shown in Fig. 88. For RDRA array, -10dB impedance bandwidth is around 18%.

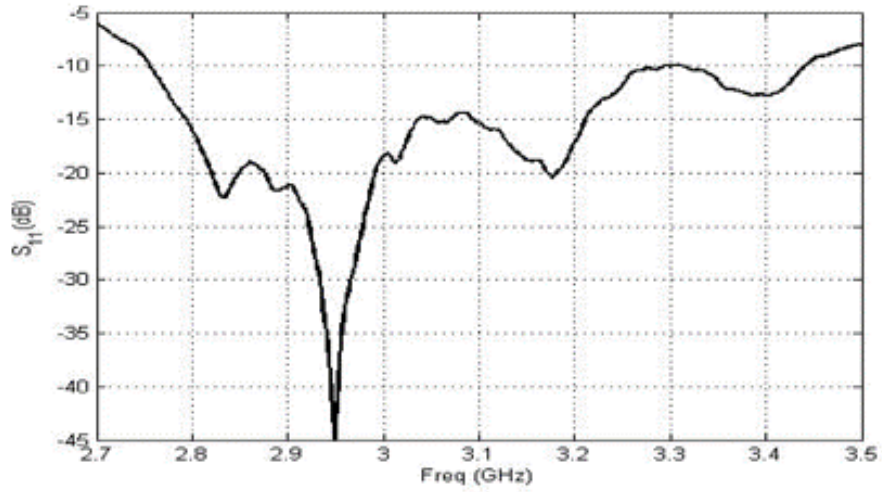

Fig. 88 Experimental return loss curve for 8-Element RDRA array

The radiation pattern at H-plane is shown in Fig. 89. The gain of the RDRA array is 10.1dB which is 0.8dB less than the simulation results. Although the SLLs are below $-26dB$ for both simulation and measurement results, it can be observed that some nulls are filled in practice.

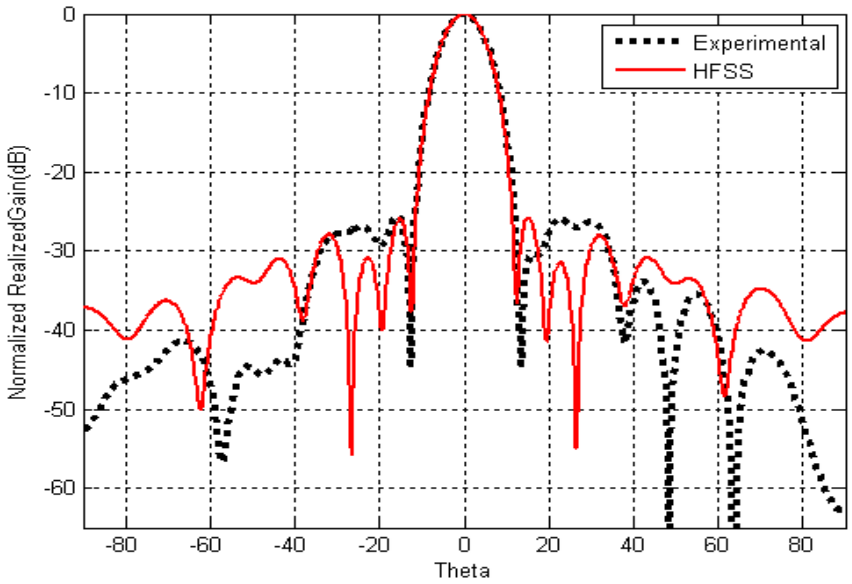

Fig. 89 Radiation pattern of 8-Element RDRA array

CHAPTER 7

CONCLUSION

The focus of this thesis work is to design an antenna array using DRAs as antenna elements. In order to utilize DRAs, the DRAs of basic shapes were investigated theoretically. Based on theoretical findings a software tool with a graphical user interface was developed to be used in designing rectangular and cylindrical DRAs. Apart from the basic shapes, a stacked cylindrical DRA is designed in order to obtain an enhancement in operational bandwidth and increase in antenna gain. An investigation also was done on various feeding mechanisms that can be used to excite DRAs. The slot coupled microstrip excitation was chosen and incorporated in all the DRA configurations in this thesis due to its flexibility in design and ease of manufacturing.

As the aim of this thesis is to provide an antenna array with a design goal of 3dB beamwidth of 10° and $-30dB$ SLL, various tapering methods were investigated. The number of array elements and the corresponding element spacing are specified for Taylor amplitude distribution. In order to maintain the required amplitude ratios between the array elements, several power divider topologies are investigated. A modified unequal Wilkinson-divider topology without isolation resistance is utilized.

An effort also was made to use HFSS for making 3-D electromagnetic analysis of the DRAs designed using software tool. Rectangular, cylindrical and stacked-cylindrical DRAs are electromagnetically solved using HFSS. Stacked-cylindrical DRA

(SCDRA) showed an increase in operational bandwidth from 16.4% to 44.7% compared to CDRA. Also an increase of 4.54dB (from 4.81dB to 9.35dB) in antenna gain is observed. Array structures are simulated on HFSS. With the 8 element SCDRA array, 3dB beamwidth of 9.5° and -26.9dB SLL are achieved.

Prototypes for rectangular DRA, stacked cylindrical DRA and feed network are manufactured. The return loss characteristics of manufactured DRAs and feed network are measured. Good agreement between the measured return loss characteristics and the simulations results were observed. Also, radiation patterns of RDRA and SCDRA are measured both in single and in array configurations. Radiation patterns were observed to be consistent with the simulation results.

As future work, various bandwidth improvement methods proposed in literature, like specially tailoring the shape of the dielectric resonator, could be further investigated. Especially hybrid antenna structures such as monopole loaded by cylindrical dielectric resonator, are attractive examples for the enhancement of operational bandwidth. Bandwidth of DRAs could be increased by exciting two or more modes with similar radiation patterns. Therefore, multi-mode DRAs could also be investigated.

APPENDIX A

MATHEMATICS OF THE RECTANGULAR DRA

The truncated dielectric waveguide model enforces magnetic walls upon the waveguide faces parallel to the x-direction. A magnetic wall imposes the boundary conditions below:

$$\mathbf{E} \cdot \hat{\mathbf{n}} = \mathbf{0} \tag{A.1}$$

$$\hat{\mathbf{n}} \times \mathbf{H} = \mathbf{0} \tag{A.2}$$

However according to ref. [15] the lowest-order TM mode of the dielectric waveguide model does not satisfy the magnetic wall boundary condition. In the same paper, fundamental TM mode has yet to be observed for a rectangular DRA. Therefore, in this thesis we will only consider the fundamental TE mode.

Addition to the magnetic wall conditions, as our DR places on a ground plane, we have "internal" field conditions at $z = 0$. Therefore, the fundamental mode geometry should obey an electric wall condition at $z = 0$:

$$\hat{\mathbf{n}} \cdot \mathbf{H} = 0 \tag{A.3}$$

$$\hat{\mathbf{n}} \times \mathbf{E} = 0 \tag{A.4}$$

A "*truncated*" dielectric waveguide model differs from the original DWG model. The *truncated* model does not impose magnetic wall boundary conditions upon dielectric faces perpendicular to the x-axis. Because, instead, we will later impose the condition in which the fields outside the dielectric resonator are below cut-off and non-propagating, but exponentially decaying.

According to [27], the vector potential for TE^x mode of dielectric waveguide in rectangular coordinate system is:

$$F = \hat{a}_x F_x(x, y, z)$$

where F_x must satisfy the scalar wave equation of

$$\nabla^2 F_x(x, y, z) + \beta^2 F_x(x, y, z) = 0$$

Then the fields can be written as:

$E_x = 0$	$H_x = -j\frac{1}{\omega\mu\epsilon}\left(\frac{\partial^2}{\partial x^2} + \beta^2\right)F_x$
$E_y = -\frac{1}{\epsilon}\frac{\partial F_x}{\partial z}$	$H_y = -j\frac{1}{\omega\mu\epsilon}\left(\frac{\partial^2 F_x}{\partial x \partial y}\right)$
$E_z = \frac{1}{\epsilon}\frac{\partial F_x}{\partial y}$	$H_z = -j\frac{1}{\omega\mu\epsilon}\left(\frac{\partial^2 F_x}{\partial x \partial z}\right)$

Table-A 1 E and H field components for TE^x modes [27]

General form for vector potential is given by [27]:

$$F_x(x,y,z) = \left(C_1\cos\left(k_y y\right) + D_1\sin\left(k_y y\right)\right)(C_2\cos(k_z z) + D_2\sin(k_z z))e^{-jk_x x} \quad \textbf{(A.5)}$$

Applying (A.1) on the surfaces $y = d/2$ and $y = -d/2$ yields:

$E_y\hat{a}_y \cdot (\hat{a}_y)\big|_{y=\frac{d}{2}} = 0 \Rightarrow$

$$e^{-jk_x x}(-k_z C_2\sin(k_z z) + D_2 k_z\cos(k_z z))\left(C_1\cos\left(\frac{k_y d}{2}\right) + D_1\sin\left(\frac{k_y d}{2}\right)\right) = 0 \quad (\boldsymbol{A.6})$$

$E_y\hat{a}_y \cdot \left(-\hat{a}_y\right)\big|_{y=-\frac{d}{2}} = 0 \Rightarrow$

$$e^{-jk_x x}(-k_z C_2\sin(k_z z) + D_2 k_z\cos(k_z z))\left(-C_1\cos\left(\frac{k_y d}{2}\right) + D_1\sin\left(\frac{k_y d}{2}\right)\right) = 0 \quad (\boldsymbol{A.7})$$

From (A.6) and (A.7)

$D_1 = 0$

$$\cos\left(\frac{k_y d}{2}\right) = 0 \Rightarrow k_y = \frac{(2n-1)\pi}{d} \qquad n = 1, 2, 3, \ldots$$

Similarly, applying (A.1) on the surfaces $z = h$ and $z = -h$ yields (Note that the resonator size in z is 2h due to image theory as there is a PEC at $z = 0$)

$$E_z \hat{a}_z \cdot (\hat{a}_z)|_{z=h} = 0 \qquad \textbf{(A.8)}$$

$$\Rightarrow -e^{-jk_x x} C_1 k_y \sin(k_y y)\,(C_2 \cos(k_z h) + D_2 \sin(k_z h))$$

$$= 0$$

$$E_z \hat{a}_z \cdot (-\hat{a}_z)|_{z=-h} = 0 \qquad \textbf{(A.9)}$$

$$\Rightarrow -e^{-jk_x x} C_1 k_y \sin(k_y y)\,(-C_2 \cos(k_z h) + D_2 \sin(k_z h))$$

$$= 0$$

Using (A.8) and (A.9)

$$\Rightarrow D_2 = 0$$

$$\cos(k_z h) = 0 \;\Rightarrow k_z = \frac{(2m+1)\pi}{2h} \qquad m = 0, 1, 2, \ldots \qquad \textbf{(A10)}$$

$$F_x(x, y, z) = \big(C_1 \cos(k_y y)\big)(C_2 \cos(k_z z)) e^{-jk_x x} =$$

$$A_{mn} \cos(k_y y)\, C_2 \cos(k_z z)\, e^{-jk_x x}$$

Substituting $F_x(x, y, z)$ in Table-A 1, the fields can be rewritten as:

$$E_x = 0$$

$$E_y = -\frac{1}{\epsilon}\frac{\partial F_x}{\partial z} = \frac{k_z A_{mn}}{\epsilon} \cos(k_y y) \sin(k_z z) e^{-jk_x x}$$

$$E_z = \frac{1}{\epsilon}\frac{\partial F_x}{\partial y} = -\frac{k_y A_{mn}}{\epsilon} \sin(k_y y) \cos(k_z z) e^{-jk_x x}$$

$$H_x = -j\frac{1}{\omega\mu\epsilon}\left(\frac{\partial^2}{\partial x^2}+\beta^2\right)F_x = -j\frac{1}{\omega\mu\epsilon}A_{mn}\cos(k_y y)\cos(k_z z)(-k_x^2+\beta^2)e^{-jk_x x}$$

$$= -j\frac{A_{mn}}{\omega\mu\epsilon}\left(k_y^2+k_z^2\right)\cos(k_y y)\cos(k_z z)e^{-jk_x x}$$

$$H_y = -j\frac{1}{\omega\mu\epsilon}\left(\frac{\partial^2 F_x}{\partial x\partial y}\right) = -j\frac{A_{mn}}{\omega\mu\varepsilon}(-jk_x)\left(-k_y\sin(k_y y)\right)\cos(k_z z)e^{-jk_x x}$$

$$= \frac{k_x k_y A_{mn}}{\omega\mu\epsilon}\sin(k_y y)\cos(k_z z)e^{-jk_x x}$$

$$H_z = -j\frac{1}{\omega\mu\epsilon}\left(\frac{\partial^2 F_x}{\partial x\partial z}\right) = -j\frac{A_{mn}}{\omega\mu\epsilon}(-jk_x)\cos(k_y y)\left(-k_z\sin(k_z z)\right)e^{-jk_x x}$$

$$= \frac{k_x k_z A_{mn}}{\omega\mu\epsilon}\cos(k_y y)\sin(k_z z)\,e^{-jk_x x}$$

When dielectric WG is truncated, the forward and reverse travelling waves are formed:

$$\overline{\mathrm{H}}_{resonant} = \bar{H}^+ + \bar{H}^-$$

$$\overline{\mathrm{E}}_{resonant} = \bar{E}^+ + \bar{E}^-$$

$$\bar{E}^+ + \bar{E}^- = \bar{E}_{yz}e^{-jk_x x} + \bar{E}_{yz}e^{jk_x x} = 2\cos(k_x x)\,\bar{E}_{yz}$$

$$\bar{H}^+ + \bar{H}^- = \left(\bar{H}_{yz}e^{-jk_x x} - \bar{H}_{yz}e^{jk_x x}\right) + \bar{H}_x\left(e^{-jk_x x} + e^{jk_x x}\right)$$
$$= -j2\sin(k_x x)\bar{H}_{yz} + 2\cos(k_x x)\bar{H}_x$$

Reconstructing the field equations according to truncated DWG:

$$E_x = 0$$

$$E_y = \frac{k_z A_{mn}}{\epsilon} \cos(k_x x) \cos(k_y y) \sin(k_z z) \quad \textbf{(A.11)}$$

$$E_z = -\frac{k_y A_{mn}}{\epsilon} \cos(k_x x) \sin(k_y y) \cos(k_z z) \quad \textbf{(A.12)}$$

$$H_x = -j \frac{A_{mn}}{\omega \mu \epsilon} (k_y^2 + k_z^2) \cos(k_x x) \cos(k_y y) \cos(k_z z) \quad \textbf{(A.13)}$$

$$H_y = -j \frac{k_x k_y A_{mn}}{\omega \mu \epsilon} \sin(k_x x) \sin(k_y y) \cos(k_z z) \quad \textbf{(A.14)}$$

$$H_z = -j \frac{k_x k_z A_{mn}}{\omega \mu \epsilon} \sin(k_x x) \cos(k_y y) \sin(k_z z) \quad \textbf{(A.15)}$$

To obtain the required equations for the dielectric waveguide, we have assumed an infinitely long air-filled WG bounded by magnetic walls. And inside the WG, the internal field frequencies are above the cutoff frequency and for outside the WG, the field frequencies must be below cutoff frequency to decay exponentially to zero at infinity. Thus, we can define a cut-off wavenumber k_c, occurs when k_x is zero. Consider $TE_{\delta 10}$ mode:

$$k_c^2 = k_y^2 + k_z^2 = \left(\frac{\pi}{d}\right)^2 + \left(\frac{\pi}{2h}\right)^2$$

When k_x is less than k_c, the wavenumber becomes imaginary, jk_{x0} and if we put this imaginary wavenumber into the field equations (A11-15):

$$E_x = 0$$

$$E_y = \frac{k_z A_{mn}}{\epsilon} \cos(jk_x x) \cos(k_y y) \sin(k_z z)$$

$$E_z = -\frac{k_y A_{mn}}{\epsilon} \cos(jk_x x) \sin(k_y y) \cos(k_z z)$$

$$H_x = -j\frac{A_{mn}}{\omega\mu\epsilon}\left(k_y^2 + k_z^2\right)\cos(jk_x x)\cos\left(k_y y\right)\cos(k_z z)$$

$$H_y = \frac{k_x k_y A_{mn}}{\omega\mu\epsilon}\sin(jk_x x)\sin\left(k_y y\right)\cos(k_z z)$$

$$H_z = \frac{k_x k_z A_{mn}}{\omega\mu\epsilon}\sin(jk_x x)\cos\left(k_y y\right)\sin(k_z z)$$

Note that the imaginary part of last two equation is absent due to imaginary wavenumber jk_{x0}. Expanding cosine function with imaginary variable into exponential form:

$$E_x = 0$$

$$E_y = \frac{k_z A_{mn}}{\epsilon}\left(\mathrm{e}^{k_{x0}x} + \mathrm{e}^{-\mathrm{k_{x0}x}}\right)\cos\left(k_y y\right)\sin(k_z z)$$

$$E_z = -\frac{k_y A_{mn}}{\epsilon}\left(\mathrm{e}^{k_{x0}x} + \mathrm{e}^{-\mathrm{k_{x0}x}}\right)\sin\left(k_y y\right)\cos(k_z z)$$

$$H_x = -j\frac{A_{mn}}{\omega\mu\epsilon}\left(k_y^2 + k_z^2\right)\left(\mathrm{e}^{k_{x0}x} + \mathrm{e}^{-\mathrm{k_{x0}x}}\right)\cos\left(k_y y\right)\cos(k_z z)$$

$$H_y = \frac{k_x k_y A_{mn}}{\omega\mu\epsilon}\left(\mathrm{e}^{-k_{x0}x} - \mathrm{e}^{\mathrm{k_{x0}x}}\right)\sin\left(k_y y\right)\cos(k_z z)$$

$$H_z = \frac{k_x k_z A_{mn}}{\omega\mu\epsilon}\left(\mathrm{e}^{-k_{x0}x} - \mathrm{e}^{\mathrm{k_{x0}x}}\right)\cos\left(k_y y\right)\sin(k_z z)$$

Now we can divide the fields according to its directions, for +x directed fields where $x > w/2$ the expressions are:

$$E_x = 0$$

$$E_y = \frac{k_z A_{mn}}{\epsilon}\mathrm{e}^{-\mathrm{k_{x0}x}}\cos\left(k_y y\right)\sin(k_z z) \quad \textbf{(A.16)}$$

$$E_z = -\frac{k_y A_{mn}}{\epsilon}\mathrm{e}^{-\mathrm{k_{x0}x}}\sin\left(k_y y\right)\cos(k_z z) \quad \textbf{(A.17)}$$

$$H_x = -j\frac{A_{mn}}{\omega\mu\epsilon}\left(k_y^2 + k_z^2\right)\mathrm{e}^{-\mathrm{k_{x0}x}}\cos\left(k_y y\right)\cos(k_z z) \quad \textbf{(A.18)}$$

$$H_y = \frac{k_{x0}k_y A_{mn}}{\omega\mu\epsilon}\mathrm{e}^{-k_{x0}x}\sin\left(k_y y\right)\cos(k_z z) \quad \textbf{(A.19)}$$

$$H_z = \frac{k_{x0}k_z A_{mn}}{\omega\mu\epsilon}\mathrm{e}^{-k_{x0}x}\cos\left(k_y y\right)\sin(k_z z) \quad \textbf{(A.20)}$$

The fields must obey the continuity conditions, E_y, E_z, H_x, H_y, H_z must be continuous at the boundaries where $x = w/2$:

Inside equations $(x = d/2)$ *(A.11-15)*	*Outside equations* $(x = d/2)$ *(A.16-20)*
$E_y = \frac{k_z A_{mn}}{\epsilon}\cos\left(k_x\frac{w}{2}\right)\cos\left(k_y y\right)\sin(k_z z)$	$= \frac{k_z A_{mn}}{\epsilon}\mathrm{e}^{-\mathrm{k_{x0}}\frac{w}{2}}\cos\left(k_y y\right)\sin(k_z z)$
$E_z = -\frac{k_y A_{mn}}{\epsilon}\cos\left(k_x\frac{w}{2}\right)\sin\left(k_y y\right)\cos(k_z z)$	$= -\frac{k_y A_{mn}}{\epsilon}\mathrm{e}^{-\mathrm{k_{x0}}\frac{w}{2}}\sin\left(k_y y\right)\cos(k_z z)$
$H_x = \frac{A_{mn}}{jw\mu\epsilon}\left(k_y^2 + k_z^2\right)\cos(k_x\frac{w}{2})\cos\left(k_y y\right)\cos(k_z z)$	$-\frac{jA_{mn}}{w\mu\epsilon}\left(k_y^2 + k_z^2\right)\mathrm{e}^{-\mathrm{k_{x0}}\frac{w}{2}}\cos\left(k_y y\right)\cos(k_z z)$
$H_y = -j\frac{k_x k_y A_{mn}}{w\mu\epsilon}\sin(k_x\frac{w}{2})\sin\left(k_y y\right)\cos(k_z z)$	$= \frac{k_{x0}k_y A_{mn}}{w\mu\epsilon}\mathrm{e}^{-k_{x0}\frac{w}{2}}\sin\left(k_y y\right)\cos(k_z z)$
$H_z = -j\frac{k_x k_z A_{mn}}{w\mu\epsilon}\sin(k_x\frac{w}{2})\cos\left(k_y y\right)\sin(k_z z)$	$= \frac{k_{x0}k_z A_{mn}}{w\mu\epsilon}\mathrm{e}^{-k_{x0}\frac{w}{2}}\cos\left(k_y y\right)\sin(k_z z)$

If either of the H_y or H_z equality is divided by one of first three equality, we can obtain:

$$-jk_x\tan\left(k_x\frac{w}{2}\right) = k_{x0} \quad \textbf{(A.21)}$$

Now to find one more independent equation between k_{x0} and k_x we can use the equation outside the DR:

$$|k_0|^2 = k_{x0}^2 + k_{y0}^2 + k_{z0}^2 \quad \textbf{(A.22)}$$

and inside the DR:

$$|k|^2 = k_x^2 + k_y^2 + k_z^2$$

$$\Rightarrow k_y^2 + k_z^2 = |k|^2 - k_x^2 \quad \textbf{(A.23)}$$

where $k_y = k_{y0}$ and $k_z = k_{z0}$ at normal incidence. Substitute (A.23) in (A.22) yields:

$$-k_{x0}^2 = |k|^2 - |k_0|^2 - k_x^2$$
$$-k_{x0}^2 = (\varepsilon_r - 1)|k_0|^2 - k_x^2$$

$$\Rightarrow jk_{x0} = \sqrt{(\varepsilon_r - 1)|k_0|^2 - k_x^2} \quad \textbf{(A.24)}$$

Substitute (A.24) in (A.21):

$$k_x \tan\left(k_x \frac{w}{2}\right) = \sqrt{(\epsilon_r - 1)|k_0|^2 - k_x^2} \quad \textbf{(A.25)}$$

Using (A.25) k_x and, therefore, the resonant frequency can be solved. This equation is usually solved asymptotically.

REFERENCES

[1] R. Richtinger, "Dielectric Resonators," *Journal of Applied Physics,* vol. 10, pp. 391-398, 1939.

[2] A. Okaya and L. Barash, "The Dielectric Microwave Resonator," *Proc. IRE,* vol. 50, pp. 2081-2092, October 1962.

[3] S. A. Long, M. W. McAllister and L. C. Shen, "The resonant cylindrical dielectric cavity antenna," *IEEE Trans. Antennas Propogat.,* Vols. AP-31, pp. 406-412, 1983.

[4] M. T. Birand and R. V. Gelsthorpe, "Experimental millimetric array using dielectric radiators fed by means of dielectric waveguide," *IEEE Electronic Letters,* vol. 17, no. 18, pp. 633-635, 1981.

[5] R. K. Mongia and P. Bhartia, "Dielectric Resonator Antennas - a review and general design relations for resonant frequency and bandwidth," *Int. Microwave Millimeter-Wave Computed-Aided Eng.,* vol. 3, no. 4, pp. 230-247, 1994.

[6] Q. Lai, G. Almpanis, C. Fumeaux, H. Benedickter and R. Vahldieck, "Comparison of the radiation efficiency for the dielectric resonator antenna and the microstrip antenna at Ka band," *IEEE Trans. Antennas Propag.,* vol. 56, no. 11, pp. 3589-3592, 2008.

[7] M. Gastine, L. Courtois and J. Dormann, "Electromagnetic resonances of free dielectric spheres," *Microwave Symposium Digest, 1967 G-MTT International,* pp. 28 - 31, 1967.

[8] A. Petosa, Dielectric Resonator Antenna Handbook, Artech House Antennas and Propagation Library, 2007.

[9] A. Yaghjian and S. Best, "Impedance, bandwidth, and Q of antennas," vol. 53, no. 4, pp. 1298 - 1324, April 2005.

[10] A. W. Glisson, D. Kajfez and J. James, "Evaluation of Modes in Dielectric Resonators Using a Surface Integral Equation Formulation," *IEEE,* Vols. MTT-31, no. 12, pp. 1023-1029, 1983.

[11] D. Kajfez, A. W. Glisson and J. James, "Computed Modal Field Distributions for Isolated Dielectric Resonators," *IEEE,* Vols. MTT-32, no. 12, pp. 1609-

1616, 1984.

[12] J. C. Sethares and S. J. Naumann, "Design of Microwave Dielectric Resonators," *IEEE,* Vols. MTT-14, no. 1, pp. 1-7, 1966.

[13] H. Y. Yee, "An investigation of microwave dielectric resonators," Microwave Lab. Rep. 1065, Stanford Univ. Stanford, CA, July 1963.

[14] J. van Bladel, "On the Resonances of a Dielectric Resonator of Very High Permittivity," *IEEE,* vol. 23, no. 2, pp. 199-208, 1975.

[15] R. K. Mongia and A. Ittipiboon, "Theoretical and Experimental Investigations on Rectangular Dielectric Resonator Antennas," *IEEE,* vol. 45, no. 9, pp. 1348-1356, 1997.

[16] G. Bit-Babik, C. Di Nallo and A. Faraone, "Multimode dielectric resonator antenna of very high permittivity," *IEEE, Antennas and Propagation Society International Symposium,* vol. 2, pp. 1383-1386, 2004.

[17] M. K. Luk and K. W. Leung, Dielectric Resonator Antennas, Hertfordshire, England: Research Studies Press Ltd., 2003.

[18] M. T. K. Tam and R. D. Murch, "Compact Circular Sector and Annular Sector Dielectric Resonator Antennas," *IEEE Transactions on Antennas & Propogation,* vol. 47, no. 5, pp. 837-842, 1999.

[19] A. Ittipiboon, A. Petosa, D. Roscoe and M. Cuhaci, "An Investigation of a Novel Broadband Dielectric Resonator Antenna," *IEEE Antennas and Propogation Symposium Digest AP-S,* pp. 2038-2041, 1996.

[20] M. Lapierre, Y. M. M. Antar, A. Ittipiboon and A. Petosa, "Ultra Wideband Monopole/Dielectric Resonator Antenna," *IEEE Microwave and Wireless Components Letters,* vol. 15, no. 1, pp. 7-9, 2005.

[21] K. P. Esselle, "A Dielectric-Resonator-On-Patch (DROP) Antenna for Broadband Wireless Applications," *IEEE Antennas & Prop. Symposium Digest AP-S,* vol. 2, pp. 22-25, 2001.

[22] F. Z. R. E. Collin, "Part 1," in *Antenna Theory,* McGraw Hill, 1969, pp. 24-25.

[23] R. A. Kranenburg and S. A. Long, "Microstrip Transmission Line Excitation of Dielectric Resonator Antennas," *IEE Electronics Letters,* vol. 24, no. 18, pp. 1156-1157, 1988.

[24] A. Petosa, "Design and Analysis of Multisegment Dielectric Resonator Antennas," *IEEE Transactions on Antennas & Propogation,* vol. 48, no. 5, pp. 738-742, 2000.

[25] T. A. Milligan, Modern Antenna Design, Wiley, 2005.

[26] S. J. Orfanidis, "Electromagnetic Waves & Antennas," 21 June 2004 . [Online]. Available: http://www.ece.rutgers.edu/~orfanidi/ewa/. [Accessed 10 04 2015].

[27] L. I. Parad and R. L. Moynihan, "Split-Tee Power Divider," *IEEE Transactions on Microwave Theory and Techniques,* vol. 13, no. 1, pp. 91-95, 1965.

[28] C. A. Balanis, Advanced Engineering Electromagnetics, John Wiley & Sons, 1989.

[29] R. K. Mongia, A. Ittipiboon, M. Cuhaci and D. Roscoe, "Radiation Q-factor of Rectangular Dielectric Resonator Antennas," *IEEE Antennas and Propagation Society International Symposium, 1994. Seattle, WA, USA.*, vol. 2, pp. 764-767, 1994.

[30] A. A. Kishk and A. W. Glisson, "Bandwidth Enhancement for Split Cylindrical Dielectric Resonator Antennas," *PIER, Progress in Electromagnetics Research,* vol. 33, pp. 97-118, 2001.

[31] A. A. Kishk, G. Zhou and A. W. Glisson, "Anaylsis of Dielectric-Resonator Antennas with Emphasis on Hemispherical Structures," *IEEE, Antennas and Propogation Magazine,* vol. 36, no. 2, pp. 20-31, 1994.

[32] K. Leung, K. Luk, K. Lai and D. Lin, "Theory and experiment of a coaxial probe fed hemispherical dielectric resonator antenna," *IEEE Transactions on Antennas and Propagation,* vol. 41, no. 10, pp. 1390-1398, 1993.